Univerzita Karlova v Praze
Přírodovědecká fakulta

Studijní program: Anorganická chemie

Ing. Jan Mrázek

Příprava ternárních $Zn_xTi_yO_z$ nanostruktur metodou sol-gel a jejich aplikace v technologii solárních článků a ve fotonice

Sol-gel synthesis of ternary $Zn_xTi_yO_z$ nanostructures for applications in solar cell technologies and photonics

Typ závěrečné práce

Disertační

Vedoucí závěrečné práce:

RNDr. Daniel Nižňanský, Ph.D.

Praha, 2011

Charles University in Prague
Faculty of Science

Study program: Inorganic chemistry

Ing. Jan Mrázek

Sol-gel synthesis of ternary $Zn_xTi_yO_z$ nanostructures for applications in solar cell technologies and photonics

Ph.D. Thesis

Supervisor: RNDr. Daniel Nižňanský, Ph.D.
Supervisor-consultant: Ing. Vlastimil Matějec, CSc.

Praha, 2011

Declaration:

I honestly declare that this dissertation describes my original work except where a reference is marked in the text. Neither this work nor its part has already been submitted in order to receive any other or the same academic title.

This declaration is not related to terms of the agreement on Co-tutelle PhD. study signed between the Charles Univesity in Prague and Université de Rennes 1 on December 7, 2006.

Prohlášení:

Prohlašuji, že jsem závěrečnou práci zpracoval samostatně a že jsem uvedl všechny použité informační zdroje a literaturu. Tato práce ani její podstatná část nebyla předložena k získání jiného nebo stejného akademického titulu.

Výjimkou je náplň dohody o vedení doktorátu pod dvojím vedením mezi Univerzitou Karlovou v Praze a Université de Rennes 1 uzavřenou dne 7.12.2006.

V Praze, 5.4.2011

Podpis

Acknowledgement

It is an honour for me to express my sincere gratitude to Professor Dr. Lubomír Špaňhel and RNDr. Daniel Nižňanský, Ph.D. for their supervising and their angelic patience with which they led me over all hardships of my studies.

I am much obliged to Vlastimil Matějec and Ivan Kašík for their admirably efforts in solving my problems that have arisen in the course of my dissertation.

It is a pleasure to thank those who made this thesis possible, namely my colleges Martin Surýnek for his friendship, Geneviéve Chadeyron and Michel Potel and whole staff of "Equipe verres et ceramique" for excellent cooperation. Special thanks belong to admirable Marcel Poulain for all his psychical support and valuable advices.

Last, but not least gratitude belongs to the French Embassy at Prague for awarded bursary that allowed me to do my studies at Université de Rennes 1.

Abstrakt

Tato práce se zabývá přípravou nanokrystalických materiálů ternárních fází $Zn_xTi_yO_z$, jejich charakterizací a potenciální aplikací ve fotonice. Dosažené výsledky přinášení nové poznatky o procesech vedoucích ke vzniku nanokrystalických fází $Zn_xTi_yO_z$ z amorfních xerogelů a poskytují nové informace o strukturních a opto-elektrických vlastnostech připravených materiálů. Na základě vypracovaných postupů lze připravit většinu z doposud známých ternárních struktur, a to nejen ve formě prášku, ale i ve formě tenkých vrstev.

K přípravě byla zvolena metoda sol-gel. Připravené základní soly byly připraveny dvěma postupy. V prvním postupu je využito reakce $[Zn_4O]$acetát$_6$ klastrů s i-propoxidem titaničitým. Druhý postup je založen na přímé heteronukleaci dihydrátu octanu zinečnatého s butoxidem titaničitým v ethanolu. Připravené soly byly alternativně dopovány 1 at. % Eu^{3+} a naneseny jako tenké vrstvy nebo tepelně zpracovány na xerogely.

První část práce se věnuje studiu krystalizačních vlastností a teplotnímu vývoji vzniklých sloučenin. Na základě dosažených výsledků byly přirpraveny čisté nanokrystalické faze inverzního spinelu Zn_2TiO_4, defektního spinelu $ZnTiO_3$ and rhombohedrického $ZnTiO_3$ s definovanou velikostí nanokrystalů. V závislosti na zvolených podmínkách tepelného zpracování může být velikost nanokrystalů v připraveném materiálu plynule měněna v rozsahu od desítek nanometrů až do řádu mikrometrů. Materiály s kubickou mřížkou lze dopovat prvky vzácných zemin.

V druhé části práce jsou poznatky získané v první části práce využity pro přípravu tenkých vrstev s definovaným složením a nanokrystalickou strukturou. Tloušťku připravených vrstve lze plynule měnit od několika nanometrů, až do několika mikrometrů. Pro jednotlivé faze byly stanoveny indexy lomu, disperzní charakteristiky a šířky zakázaného pásu. Index lomu materiálů s krychlovou mřížkou se pohybují od 1,7 do 1,95. Stanovené šířky zakázaného pásu byly přibližně 3,7 eV. Vypočtený index lomu romboedrického $ZnTiO_3$ byl ca 2,56, šířka zakázaného pásu 3,61 eV.

Třetí část práce je věnována přípravě optických vláken. Nanočástice oxidu zinečnatého dopované Eu^{3+} ionty byly úspěšně naneseny do křemenné frity v substrátové trubici, která byla zpracována preformu. Preforma byla vytažena do optického vlákna s vnějším průměrem 124 μm, průměrem jádra 15 μm a anumerickou aperturou 0,084. Základní útlum připraveného vlákna činil $dB \cdot m^{-1}$. Koncentrace sledovaných prvků v připravené preformě byla přibližně 0.9 at. % zinečnatých iontů a 0.12 at. % europitých iontů. Bylo jednoznačně ukázáno, že nanočástice oxidu zinku připravené metodou sol-gel mohou být úspěšně využity jako hostitelská matrice pro prvky vzácných zemin a být využity pro přípravu aktivních optických vláken. Parametry připraveného vlákna jsou srovnatelné s parametry vlákna připraveného standardním postupem, který využívá metodiky depozice iontů vzácných zemin z roztoků.

Abstract

The presented study deals with the sol-gel synthesis of nanocrystalline ternary phases of the general formula $Zn_xTi_yO_z$, their characterization and potential application in photonics. Achieved results bring new fundamental knowledge about the processes leading to the formation of $Zn_xTi_yO_z$ nanocrystals from amorphous xerogels and give novel information about structural and opto-electrical properties of the prepared materials. he presented results allow us to prepare most of up-to-date reported $Zn_xTi_yO_z$ compounds with tailored nanocrystaline sizes and structures in forms of powders or thin films.

Two sol-gel approaches based on the cluster process and direct heteronucleation were employed to prepare initial sols. These sols were optionally doped by Eu^{3+} ions to evaluate effects of rare earth elements to crystallization properties of the formed compounds.

In the first part of this study crystallization properties and structural evolution of thermally treated xerogels were analyzed. As a result a versatile sol-gel method allowing the preparation of inverse spinel Zn_2TiO_4, cubic defect spinel $ZnTiO_3$ and rhombohedral $ZnTiO_3$ with tailored nanocrystal sizes was designed and developed. By controlling the initial composition of sols and conditions of thermal annealing this method allows us to prepare selected ternary phases with tailored nanocrystal sizes ranging from tens of nanometers up to micrometric scale. The formed cubic structures can be doped by rare earth elements up to their limits of solubility.

In the second part of the study, the approaches elaborated in the first part were successfully exploited for the preparations of thin films with define nanocrystalline structure and selected compositions. The thickness of the prepared films varied from several tens of nanometers up to few micrometers. Refractive indexes, dispersion curves and band gap energies of particular structures were determined. Refractive indexes of cubic structures range from 1.70 to 1.95. The determined band gap energy is approximately of 3.7 eV. The calculated refractive index of rhombohedral $ZnTiO_3$ was around 2.56 and band gap energy of 3.61 eV.

In the third part of this study zinc oxide nanoparticles doped by Eu^{3+} ions were successfully applied into a silica frit that was sintered and collapsed into the core of a fiber preform. The preform was drawn into an optical fiber with an outer diameter of 124 μm, the core diameter of 15 μm and numerical aperture equal to 0.084. Baseline losses of the prepared fiber were around 0.9 $dB \cdot m^{-1}$. The concentration of particular elements inside the preform was approximately 0.9 at. % of Zn^{2+} ions and 0.12 at. % of Eu^{3+} ions. These results clearly demonstrate that zinc oxide nanoparticles prepared by the sol-gel process can be successfully employed as a part of host matrixes for rare earth elements allowing the preparation of active optical fibers with parameters close to optical fibers prepared by the standard or modified solution doping method.

Table of content

List of symbols and abbreviations

c	molar concentration
c_L	speed of light in vacuum
d	inter-planar distance
h	Planck constant
k	numerical coefficient
k_g	parameter of the type of transition
k_L	absorption coefficient of optical losses
k_S	structural factor
l	length of the light path
m	mass
n	refractive index
n_I	multiplication factor
A	integration constant
A_c, B_c, C_c, D_c, E_c, F_c	constant of Cauchy's equation
A_N	aggregation number
E_A	activation energy of the crystallization
E_c	conduction band
E_g	band gap energy
E_V	valence band
I	intensity
I_0	initial intensity
R	ideal gas constant
R(J2/J1)	asymmetry factor
R_P	Fresnel's coefficient of reflection for P polarization
R_S	Fresnel's coefficient of reflection for S polarization
S	integrated peak area
S_i	Stokes parameter
T	temperature
T_0	thermodynamic temperature
T_p	peak temperature
V	volume
Z	number of elementary charges
α	absorption coefficient
α_c	critical angle
β	heating rate
β_c	correlated full width in half maximum
δ	partial charge
ε	extinction coefficient
λ	wavelength
ν	frequency of electromagnetic field
τ	film thickness
Δ	phase difference
Ψ	amplitude of polarized light
θ	angle of incidence

AFM	atomic force microscopy
DSC	differential scanning calorimetry
DTA	differential thermal analysis
EDS	energy-dispersive X-ray spectroscopy
FT-IR	Fourier transform infrared spectroscopy
FWHM	full width in half maximum
HOMO	highest occupied molecular orbital
LUMO	lowest unoccupied molecular orbital
MS	mass spectrometry
NA	numerical aperture
NIR	near infrared
REE	rare earth elements
RMS	standard deviation of roughness
SE	spectral ellipsometry
SEM	scanning electron microscopy
TEM	transmission electron microscopy
TG	thermal gravimetry
UV	ultraviolet
VIS	visible
XRD	X-ray diffraction

Preface

This work has arose from the newly established cooperation between the Institute of Photonics and Electronics AS CR, v.v.i. at Prague and Laboratory of Nanocolloidal Materials, Université de Rennes 1, managed by Prof. Dr. Lubomír Špaňhel. The common goal of our laboratories was to investigate materials that would be exploited in photonics and photocatalysis. The original idea of this work was to profit on huge experiences of Prof Špaňhel and prepare metallic nanoparticles which would lead to new types of optical sensors based on localized surface plasmon resonance.

Due to financial and organizational reasons the research in this study has been extended to novel materials based on the nanoparticles of zinc oxide. As it has proved to be unsustainable to kept running two different projects, the original idea was abandoned and this work has been focused to preparation and characterization of $Zn_xTi_yO_z$ nanocrystalline structures.

Materials based on $Zn_xTi_yO_z$ structures were in the focus of both research institutions. Their possible photocatalytic properties could be widely exploited in the fundamental and applied research programs of Laboratory of Nanocolloidal Materials. Their crystalline structure makes them suitable as matrixes for variety of dopants including rare earths elements. For such a reason they could be exploited as novel materials for optical waveguides and active optical components. Modus operandi in our laboratories is based on the sol-gel method. For this reason the whole study is focused to colloidal approaches and sophisticated physical methods as molecular beam epitaxy or metal-organic chemical vapor deposition are slightly disregarded. By this disregarding, I do not want to deny their enormous importance in the field of nanomaterials.

Because the work had been mingling with projects of other colleagues the variety of achieved results was very broad. As well the purpose exploitation of prepared materials was slightly different in both laboratories. Such circumstances resulted into huge broadening of planned goals and great number of particular results. Thus, it was difficult to choose data that made a compact topic. After careful consideration I have decided not to include parts of my work dealing with the preparation and characterization of $Zn_xTi_yO_z$ doped by other compounds than rare earth elements. So the whole chapter dealing with the photocatalysis was skipped.

Continuous movement between two laboratories placed high requirements on the temporal stability and reproducibility of prepared samples. As was confirmed in several laboratories elaborated methods were practically fully reproducible leading to the preparation of samples of excellent quality.

Introduction

Photonics and principle of optical fibers

Photonics deals with the generation, transmission, detection and processing of light. It covers wide area of activities from the fundamental research of novel photonic structures to the development of industrial application and commercial products. From historical and practical reasons the term "light" is not understood as purely visible part of the spectra, but it's extended to the near infrared region where telecommunications frequencies are localized ranging from 1250 to 1650 nm [1]. The photonics research covers theoretical fundamentals of the interaction of light with different materials, material research and application part which exploits acquired knowledges to the development and fabrication of novel photonic devices. From the application point of view photonic's the research deals with light sources, detectors, waveguides including optical fibers, sensors etc. A number of results of these research and production activities can be found in daily life. Let me to mention light emitting diodes (LED), plasma and LED screens, or optical sensors in medicine [2]. Despite the fact that they usually stay in shadows, optical fibers make a backbone of the modern information society.

An optical fiber is usually defined as a cylindrical optical waveguide whose transversal length is significantly larger than a lateral dimension [3]. A structure of optical fiber is shown in

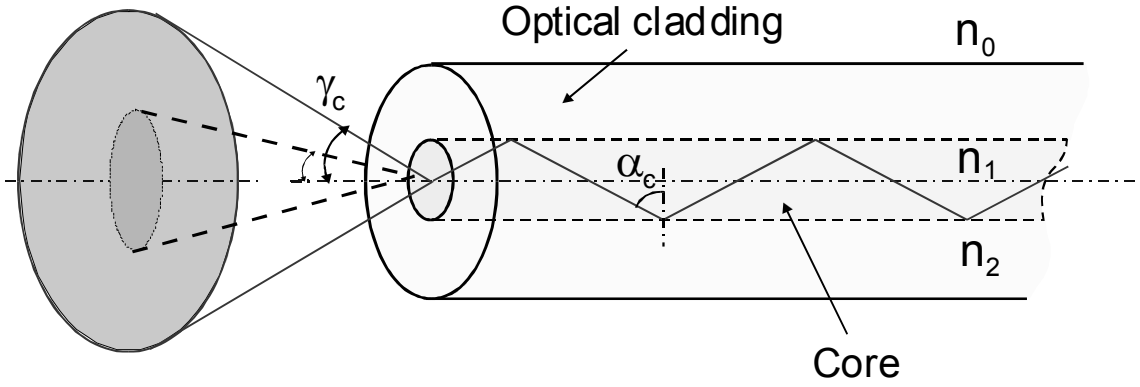

Figure 1 Principle of optical fiber. n_0 -surrounding medium (air), n_1 -refractive index of the fiber core, n_2 –refractive index of cladding, α_c –critical angle, γ_c –output angle of emitted light

Figure 1. Light is transmitted through the fiber due to the total reflections on the core-cladding boundary. From the well known Snell's law it can be deduced, that the critical angle α_c corresponds to the ratio of the refractive index of the the cladding n_2 over the refractive index of the fiber core n_1 as can be seen from the equation :

$$\frac{n_2}{n_1} = \sin \alpha_c \tag{1}$$

With regard to changes of the transmitted light, optical fibers can be divided to passive or active. Light transmitted through passive optical fibers is attenuated due to optical losses of the fiber. Active optical fibers can amplify light signals transmitted through the fiber. They act as fiber lasers. Laser effects in optical fibers are realted to the doping of the fiber core with suitable elements. Usually rare earth elements (REE) such a erbium, thulium are used as dopants because the energy of their f-f internal transitions corresponds to the spectral range

from 1250 nm to 1650 nm, where telecomunication frequencies are localized. Together with Er^{3+} ions, Yb^{3+} ions are usually introduced into the core [4]. The energy diagram of erbium and ytterbium-doped silica optical fibers is demonstrated in Figure 2. Such a fiber is pumped by a laser operating at 980 nm. Excited electrons are tranfered from Yb^{3+} to Er^{3+} ions and undergo an non-radiative transition. Thus, the inverse population of Er^{3+} can be obtained. The wavelength of the signal generated in the fiber corresponds to the energy difference between the energy level with the inverse population and the ground state of Er^{3+} ions. In amplifiers the transmitted light causes a stimulated emission and it is amplified.

With increasing requirements to the data transmission novel approaches improving the properties of fiber lasers are under research. Beside of development novel arrangements of

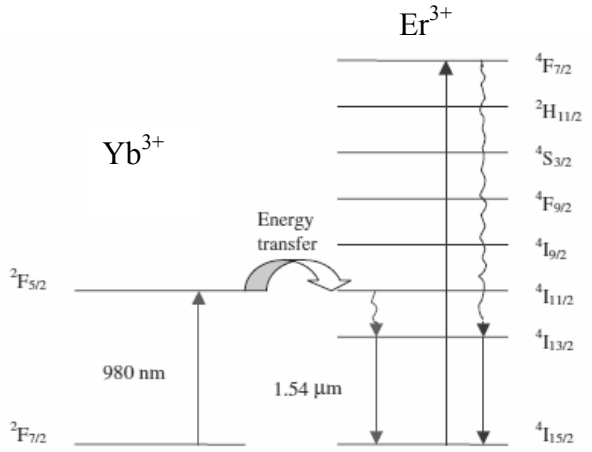

Figure 2 Energy level diagram of Er^{3+} and Yb^{3+} ions in silica matrix [4] illustrating the non-radiative charge transfer to Er^{3+} followed by the stimulated emission at 1540 nm.

fiber lasers [5], the main attention is focused to exploitation of novel matrices that could improve optical properties of lasers and amplifiers by suppressing clustering effects of REE [6]. The last trend in this field consists in incorporating ceramic nanoparticles together with REE [7] in order to increase their solubility inside the host matrix, suppress the clustering of REE oxides and increase the quantum efficiency of radiative transitions.

Nanomaterials

For the purpose of this study nanoparticles and nanomaterials will be defined as objects which exhibit a particle dimensions or a structural dimensions in nanometric scale. Such a dimension can provide a lot of advantages due to newly raised quantum states, better structural homogeneity, high porosity etc. As an example one can mention the exploitation of quantum dots in fluorescence optical sensors and optical imaging [8]. The increased porosity is widely used in the field of photocatalysis [9, 10]. The nanocrystalline structure of materials can lead to their better transparency and thus to a better performance of active optical waveguides based on them [11, 12] or can be employed for the development of new light sources [13, 14].

Opto-electronic properties of semiconductors

Theoretical and experimental research of semiconductors includes an enormous number of particular specialization. It is completely out of scope of this study to introduce them even in their simplified form. For this reason only the general concept and the definition of basic terms are presented.

Opto-electronic properties of nanomaterials often depend on the size of nanoparticles from which they are composed. The reason for this could be found in the existence of new quantum states that raise up in these nanoparticles. As an example of such a phenomena one can mention the fluorescence of CdSe and CdS quantum dots which significantly depends on the size of formed nanoparticles [15, 16].

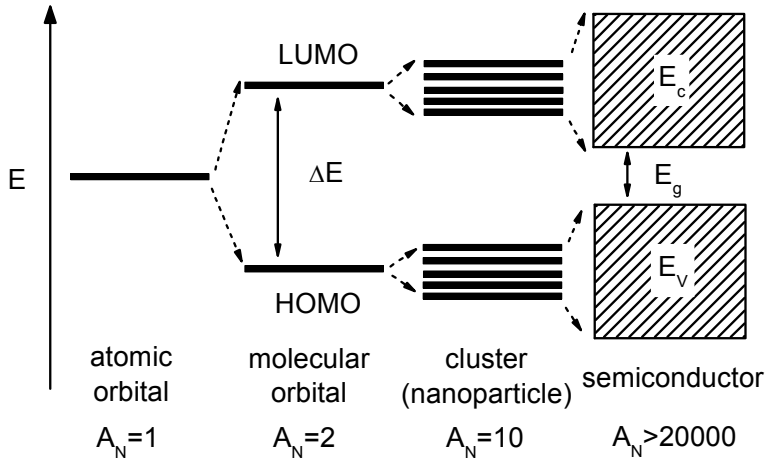

Figure 3 Schematic chart of changes in electronic structure of a semiconductor compound formed by aggregated monomers. A_N refers to the aggregation number of monomeric units. Adapted from [16].

According to the quantum theory, atomic orbitals in an isolated atom correspond to discrete energy levels [17, 18]. The chemical bond between two species can be approximated by the theory of molecular orbitals. The formation of these orbitals can be seen from Figure 3. In case of two identical species, the original atomic orbitals are combined to form the same number of molecular orbitals. The formed orbitals are hybridized and splitted into two levels. Electrons are redistributed into the formed molecular orbitals in order to conserve the minimum of energy. The filled molecular orbital with the highest energy is called the highest occupied molecular orbital (HOMO), the first empty orbital is called the lowest unoccupied molecular orbital (LUMO). They can be characterized by the energy difference ΔE. Such an energy difference corresponds to the minimal energy that must be given to the electron in the HOMO orbital to excite it into the LUMO orbital. With further increasing the number of aggregated species the polymolecular cluster or nanoparticle is formed. Energy sublevels in this cluster are further splitted however they still appear the discreet character. The energy difference between the LUMO and HOMO orbitals is decreasing. A limiting case is achieved for a huge number of aggregated species which correspond to the electronic band structure. The combined atomic orbitals form continuous bands separated by the forbidden band. The band, where electrons are localized, is called the valence band and is characterized by energy E_v, the formed band unoccupied by electrons is called the conduction band. The energy

between the conduction and the valence band is characterized by the band gap energy E_g. Conventionally materials are classified by the value of E_g to insulators for $E_g > 3.6$ eV and semiconductors for $E_g < 3.6$ eV.

The fundamental equation assigns to light with the frequency ν the corresponding energy E:

$$E = h \cdot \nu = h \cdot \frac{c_L}{\lambda} \ , \tag{2}$$

through the Planck constant h. Equation 2 can be expressed via the wavelength λ and the velocity of light c_L. If the energy of light interacting with the semiconductor is higher than band gap energy then light can be absorbed by the material and eventually excite the electron from the valence band to the conducting band. If the excitation of the electron in semiconductors is associated with the conservation of the electron momentum, such semiconductors are called direct semiconductors. If the excitation of the electron from the valence band to the conduction band is associated with a change of the electron momentum then such semiconductors are classified as indirect semiconductors.

$Zn_xTi_yO_z$ structures

Although the first compact work about the phase system based on ZnO-TiO_2 was presented more than fifty years ago, there are still many uncertainties. The original phase diagram [19] evaluated from the solid state approach is demonstrated in Figure 4. It's relatively simple and predicts the existence of five particular species with well defined chemical composition. Let's discuss their structures and properties in details.

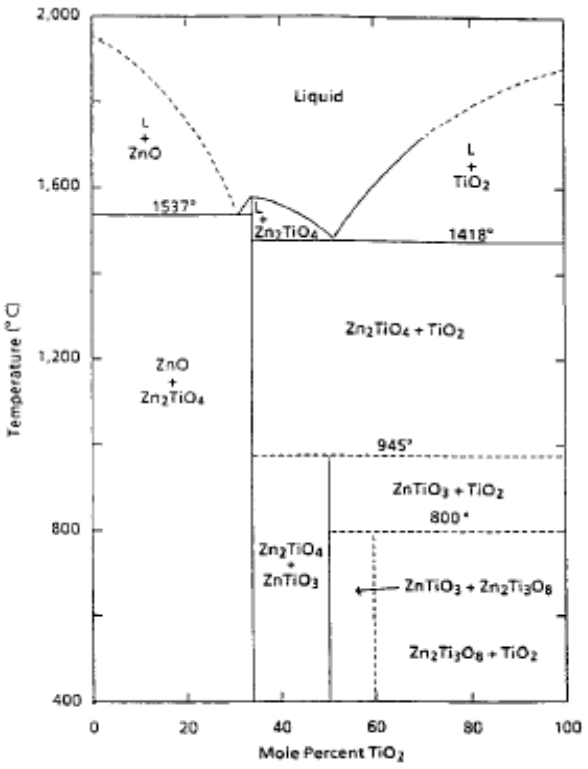

Figure 4 Phase diagram of the system ZnO-TiO_2. The results were obtained by the solid-state approach. Proposed by [18].

Zinc oxide and titanium oxide

The borders of the phase diagrams are created by zinc oxide and titanium oxide. ZnO and TiO_2 exhibit semiconductor properties and they are well established in industry. Both of them are widely used as pigments, titanium oxide, namely the anatase structure, is widely exploited as photocatalyst [20, 21].

Despite of the existence of other crystallographic modifications ZnO usually occurs as wurtzite with the hexagonal lattice. TiO_2 provides us with two tetragonal structures: anatase and rutile. Crystallographic properties of particular structures are summarized in Table 1.

In the last decade, the interest at these oxides has increased dramatically with increasing concern about nanomaterials. Tailored approaches have allowed the formation of novel nanomaterials that have found new fields of applications as transparent semiconductors [22], transducer layers in solar cell technology [23-25] as well as materials for novel light sources [14, 26]. They can be readily prepared by sol-gel routes allowing the formation of well defined nanoparticles with a tailored shape and morphology [21, 24, 27].

Table 1 Overview of selected crystallographic properties of pure oxides of system ZnO-TiO_2

	ZnO	**TiO_2**	
Used label	ZnO	a-TiO_2	r-TiO_2
Structure	wurtzite	anatase	rutile
Lattice system	hexagonal	tetragonal	tetragonal
Space group	$P6_3mc$	$I4_1/amd$	$P4_2/mnm$
Unit cell parameters (nm)	a=0.325 c=0.521	a=0.378 c=0.951	a=0.459 c=0.296
JCPDS datafile N°	36-1451	78-2486	21-1276

$Zn_xTi_yO_z$ ternary phases

Up to date three ternary phases with the general formula $Zn_xTi_yO_z$ have been reported according to the presented phase diagram. Namely Zn_2TiO_4 crystallizing in a cubic structure as an inverse spinel and $ZnTiO_3$ which was reported in a cubic structure as a defect spinel or in a rhombohedral structure as ilmenite. The third compound with the general formula $Zn_2Ti_3O_8$ has been classified into a cubic structure as a defect spinel. Because structures derived from the spinel type are quietly complicated comparing to hexagonal or tetragonal structures of pure oxides, it deserve a more detailed description. The normal spinel structure may be expressed by a general formulation AB_2O_4 [28, 29] where A is a divalent cation, B is a trivalent cation and O represent anions, usually O^{2-}. A unit cell contains 8 cations of the type A, 16 cations of the type B and 32 anions where cations A are distributed into tetrahedral positions, cations B occupies octahedral positions in the lattice. The general formulation can be expressed by the formula $(A_8)^t(B_{16})^oO_{32}$ where ^{t} depicts the tetrahedral position and ^{o} the octahedral position. In so-called inverse spinel, represented by the general formulation $B(AB)O_4$, cations A are placed exclusively in octahedral positions. Cations B are equally

distributed between tetrahedral and octahedral positions in the lattice. The structure of the inverse spinel Zn_2TiO_4 may be expressed by the formulation $(Zn_8)^t(Zn_8Ti_8)^oO_{32}$.

In the cubic structure $ZnTiO_3$ the number of zinc cations is reduced. The structure can be regarded as a defect spinel $(Zn_8)^t(Zn_{8/3}\square_{8/3}Ti_{32/3})^oO_{32}$ where a part of zinc cations is replaced by vacancies labelled by the symbol □. These vacancies increase the space that can be occupied by introduced dopants e.g. Eu^{3+} ions. Up to date, the structure of defect spinel $Zn_2Ti_3O_8$ has not been clarified. The overview of the introduced structures and their selected properties are shown in Table 2.

These ternary phases and their compounds often show superior properties over those of pure oxides, from which are formed. That is why they have attracted great attention in research as well as possible in industrial applications. They were successfully tested as novel catalysts for desulphurization [30] and dehydrogenation processes [31], in solar cell research [32-38], as advanced materials for microwave dielectrics [31-33] and as novel phosphors [39, 40].

Various methods of the preparation of these ternary phases have been reported up to date. They include solid-state and hydrothermal approaches [19, 30, 41-48], leading to the formation of powders, elaborated sol-gel routes [32-38, 40, 49-56] allowing the preparation of powders and thin films as well as sophisticated physical approaches, such as chemical vapour deposition or magnetron sputtering which allow us to prepare thin films [31, 39, 56, 57]. The approaches which were used to prepare particular phases are listed in Table 2.

Sol-gel approach to $Zn_xTi_yO_z$ structures

Comparing to the other approaches, sol-gel methods allow us to prepare nanocrystalline compounds with well defined properties. The purity of prepared materials can be controlled by initial composition of starting materials and by using the appropriate route. Moreover, sol-gel approaches allow us to prepare highly crystalline materials at low temperatures.

Up to date several sol-gel routes leading to zinc titanate compounds of general composition and structure have been reported. They are depicted in Figure 5. The first route is based on the direct heteronucleation of a proper initial compound and it was successfully employed in our laboratory to prepare powders and thin films [35, 37]. However, it still hasn't been fully explored. The second and the third methods are based on the preparation of pre-hydrolyzed polymolecular clusters that are further reacted together or with the corresponding initial precursor [35, 58]. The formed polymolecular clusters can be substituted by the colloidal solution of ZnO or TiO_2 [35, 36, 41]. This route labeled by number 4 is widely exploited. The last technique is based on the complexation of initial precursor followed by hydrolysis. This method is labeled by number 5 and it is often used [52, 54, 55, 59].

To my best knowledge the versatile sol-gel route allowing the formation of selected $Zn_xTi_yO_z$ nanocrystalline structures has not been presented so far. Moreover, the phase diagram obtained as the result of the solid state chemistry or hydrothermal approach does not provide any information about structural evolution of samples prepared by so called "bottom-up" approach. Thus, it is the intention of this thesis to elaborate a versatile sol-gel method providing $Zn_xTi_yO_z$ nanocrystalline structures with tailored sizes and structures, investigate the crystallization properties of prepared xerogels and extend acquired knowledge to the preparation of thin films.

Table 2 General overview of recently reported zinc titanate phases and their crystal structures

	Zn_2TiO_4 (c)	**$ZnTiO_3$ (r)**	**$ZnTiO_3$ (c)**	**$Zn_2Ti_3O_8$ (c)**
Used label	Zn_2TiO_4	r-$ZnTiO_3$	c-$ZnTiO_3$	-
Ratio Zn:Ti	2:1	1:1	1:1	2:3
Structure type	inverse spinel	ilmenite	not clarified defect spinel-like	defect spinel-like
Lattice system	cubic	hexagonal/ rhombohedral	cubic	cubic
Space group	Fd3m	R3	Fd3m	Fd3m/$P4_332$
Unit cell parameters (nm)	a=0.846	a=0.507 c=1.3927	a=0.840	a=0.843
JCPDS datafile N°	25-1164	26-1500	39-0190	38-3500, 73-0579
Atomic positions in the unit cell	$(Zn_8)^t(Zn_8Ti_8)^oO_{32}$	$(Zn_2Ti_2)^oO_6$	$(Zn_8)^t(Zn_{8/3}\square_{8/3}Ti_{32/3})^oO_{32}$	$(Zn_8)^t(\square_4Ti_{12})^oO_{32}$
References				
solid state and hydrothermal approach	[30, 42, 60-63]	[43, 48, 49, 62, 63]	[46, 63]	[19, 44, 45]
sol-gel routes	[38, 64]	[32, 53, 59]	[33, 35-37, 40, 52, 54, 65]	-
vapour phase deposition and sputtering	[31, 57]	[56, 57]	[31]	-

Note: c = cubic, r = rhombohedral, t = tetrahedral site, o = octahedral site, □ = vacancy

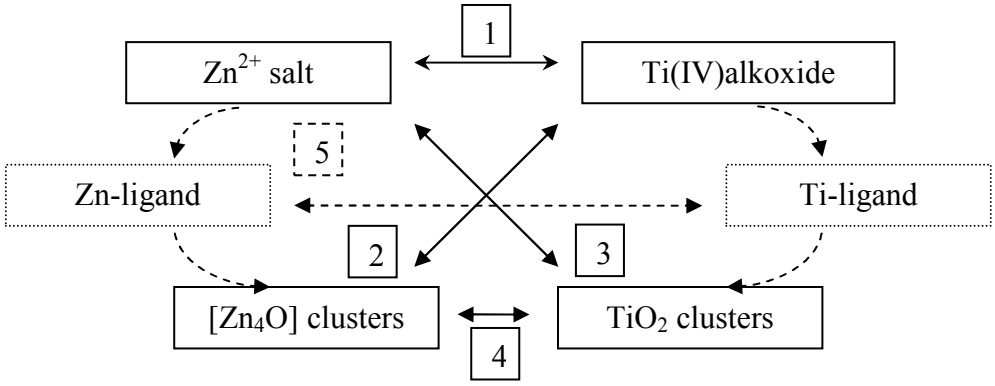

Figure 5 Overview of referred sol-gel routes allowing the preparation of $Zn_xTi_yO_z$. Method 1) direct heteronucleation process. 2 and 3) reaction of polymolecular clusters with initial compounds 4) and a reaction between pre-hydrolyzed clusters. 5) Reaction between complexes.

Aim of the study

The general aim of this thesis is to elaborate a versatile sol-gel route allowing the bottom-up synthesis of ternary phases represented by the general formula $Zn_xTi_yO_z$. Materials prepared by this route should have performance for wide employment as thin films for optical, opto-electrical and photocatalytic purposes. Therefore, well defined structures of the formed ternary phases and tailored nanocrystalline structures are required.

The general aim is specified by the following objectives:

1. To develop an appropriate versatile method allowing the reproducible preparation of ternary crystal structures on the nanoscale without side-formed phases.
2. To introduce Eu^{3+} ions into formed materials and study their structural evolution and photoluminescence properties.
3. To find an approach allowing the preparation of thin films with tailored nanocrystalline structures.
4. To determine optical and opto-electrical properties of the prepared nanocrystalline ternary structures
5. Exploit the investigated approaches in the technology of active optical fibers.

Material and methods

Selected approaches and theoretical backgrounds of used methods

Fundamentals of used methods are introduced in following chapters. As most of them are part of common knowledge, general principles and information were draw from following literature [3, 66-70]. Once a special method or technique is introduced, the adequate reference is cited.

Selected spectral methods

Absorption spectroscopy

The intensity of the light passing through the medium is decreasing according to the Lambert-Beer Law:

$$I = I_0 \cdot e^{-\varepsilon \cdot c \cdot l} = I_0 \cdot e^{-\alpha \cdot l} \ , \tag{3}$$

where I and I_0 mean the intensity of the transmitted and incident light, respectively. ε is the molar extinction coefficient, α is the absorption coefficient, c is the molar concentration and l is the length of the light path. For practical purpose the absorbance is defined by relations :

$$A = \log \frac{I_0}{I} = \varepsilon \cdot c \cdot l \ , \tag{4}$$

$$A = \ln \frac{I_0}{I} = \alpha \cdot l \ , \tag{5}$$

widely used for absorption of liquids or thin films, respectively. In fiber optic technology the attenuation A_A of the optical fiber is defined by relation[3]:

$$A_A = 10 \cdot \log \frac{I_0}{I} \ , \tag{6}$$

where I and I_0 mean the intensity of light transmitted through the fiber and light entering into the fiber.

The absorption coefficient depends on the wavelength thus on the energy of absorbed light. The energy of light absorbed in the UV-VIS spectral region corresponds to electronic transitions in the valence bands of atoms or molecules. From the position, intensity and shape of absorption bands one can deduce the internal structure of particular energy levels of the analyzed material.

The fundamental transitions in semiconductors are related to the band-to-band transition or to exciton transition. In the direct transition the electron momentum is conserved, while in the indirect transition it is changed. The type of the band gap transition can be estimated from the form of an optical absorption band. After several simplifications, the absorption coefficient can be related to the energy of band gap by the relation [71]:

$$(\alpha \cdot h \cdot \nu)^{k_g} \sim k \ \cdot (h \cdot \nu - E_g) \ , \tag{7}$$

where k_g is the coefficient acquiring the value 0.5 for the indirect transition or 2 for direct transitions and k is a numerical coefficient.

The Fourier transform infrared spectroscopy deals with the infrared part of spectra. The energy of infrared radiation is associated with rotational, vibrational and rotational-vibrational transitions in atoms and molecules. In this study FT-IR spectra will be exploited to identify particular compounds.

Luminescence spectroscopy

Luminescence is the emission of light from material in electronically exited states [72]. Luminescence is divided into two categories, fluorescence and phosphorescence. In fluorescence the excited electron is paired to the second electron in the ground-state orbital. The electronic transition from the excited state to the ground stated is spin allowed. In phosphorescence the excitation and related relaxation of the electron is associated with the spin change and both electrons in the excited and ground states have the same spin. Thus the transition of excited electron to the ground state is spin forbidden. Luminescence is associated with the emission of light which accompanied radiative transitions. The wavelength of emitted light correspond to the energy of particular transitions.

In this study two types of the luminescence measurement will be employed. The first one is the energy-dispersive X-ray spectroscopy (EDS). In EDS the sample is excited by accelerated electron beam. The energy of the electron beam is sufficient to excite electrons inside the inner shell of atoms that form the analyzed sample. The energy of the emitted radiation corresponds to inner transitions inside the electron shell. For that reason the EDS method can provide us by the information about the chemical composition of the analyzed sample.

The second technique exploits the phosphorescence of Eu^{3+} ions in visible part of spectra. The luminescence spectrum of Eu^{3+} ions is hyper sensitive to changes of the local symmetry [73]. Basically, one can recognize two peaks in the luminescence spectrum of Eu^{3+} which correspond to $^5D_0 \rightarrow {}^7F_1$ and $^5D_0 \rightarrow {}^7F_2$ electronic transitions. The first transition is associated with the magnetic dipole, the second one is associated with the electric dipole in the crystal field of Eu^{3+} ions. A change of the local symmetry of Eu^{3+} ions affects the electric dipole while the magnetic dipole remains unaffected. By decreasing the symmetry of the crystal field of Eu^{3+} ions the intensity of $^5D_0 \rightarrow {}^7F_2$ electronic transitions decreases as well. Thus, the ratio of intensities of the $^5D_0 \rightarrow {}^7F_2$ transition and $^5D_0 \rightarrow {}^7F_1$ transition can provide structural information about the site symmetry of Eu^{3+} ions. For this reason Eu^{3+} ions are widely exploited as useful indicator allowing to evaluate their displacement and symmetry of occupied positions inside the crystal lattice. This method has been widely employed to observe the formation of nanocrystalline materials. As an example one can mention the evolution of hexagonal lattices of ZnO [73], tetragonal titania [74], cubic YAG garnets [75] etc.

Thermal analysis and mass spectrometry

From general point of view, thermal analysis investigates the thermal behavior of samples (i.e. thermo mechanical properties). In the presented work the differential scanning calorimetry (DSC), differential thermal analysis (DTA) and thermal gravimetry (TG) were employed. These methods can provide us with sets of thermodynamical data.

The principle of DTA is the following: an analyzed sample in a crucible is placed onto a pan which is welded to a thermocouple. The sample pan is heated together with a reference pan in a furnace by defined heating rate under defined atmosphere. Thermodynamic

effects occurring in the sample resulting into temperature changes detected by the thermocouple. The voltage differences between the sample and the reference thermocouple are recorded as a function of the temperature.

DSC method has a similar arrangement. However, the heat flow which is needed to compensate caused temperature changes of the analyzed sample is measured. Thermodynamical processes can be evaluated from the course of the recorded signal and namely from appearing peaks.

TG method measures mass changes of an analyzed sample during the analysis. A modern TG apparatus is usually coupled with a mass spectrometer allowing to accurately determine the chemical composition of the liberated matter.

Mass spectrometry is an analytical method which allows accurately determine the quantitative and qualitative compositions of the sample. The sample is ionized liberating charged mass fragments. These fragments pass through a mass-separator. Electromagnet field inside the separator deflects the entering fragments proportionally to the ratio of their mass over their charge. The mass-separator is followed by a detector. The fragments that pass the separator impinge on the detector causing a recorded signal. Changing the electromagnetic field in the separator allows selectively choose fragments that pass to the detector and thus provide information about the qualitative composition of the sample. The quantitative information is given by the intensity of recorded signal.

The methods mentioned above are well established in the solid state chemistry allowing the exact determination of thermodynamical properties joined with solid state reactions and crystallization processes. However, the complicated composition of sol-gel derived structures, usually not fully determined, readily prevents to evaluate correct values of selected thermodynamic quantities. Despite the difficulties, noted methods can help us to determine several thermodynamical properties of prepared xerogels.

To evaluate the activation energy of crystallization processes three different approximations represented by Ozawa equation (8) [76], Kissinger equation. (9) [77] and Augis-Bennett equation (10) [78] were taken into account:

$$\ln(\beta) = -\frac{E_A}{R \cdot T_P} + A \ , \tag{8}$$

$$\ln\left(\frac{\beta}{T_P^2}\right) = -\frac{E_A}{R \cdot T_P} + A \ , \tag{9}$$

$$\ln\left(\frac{\beta}{T_P - T_0}\right) = -\frac{E_A}{R \cdot T_P} + A \ . \tag{10}$$

In the introduced equations β represents the heating rate, T_p is the peak temperature at the exothermal peak, T_0 is equal to 273.15 K and represents the conversion to Celsius scale, E_A is the activation energy of the crystallization of the amorphous phase, R is the ideal gas constant and A is the integration constant.

The mechanism of crystallization can be estimated from the value of the Avrami parameter n_A calculated from the Johnson-Mehl-Avrami equation expressed in the Ozawa's modification for linear heating rates as [79]:

$$-n_A = \left.\frac{d\{\log[-\ln(1-\alpha_A)]\}}{d\log\beta}\right|_T \ , \tag{11}$$

where n_A represents the Avrami parameter obtained from the slope of the plot $\log[-\ln(1-\alpha_A)]$ vs. $\log\beta$, α_A is the volume fraction crystallized at time t and β is the heating rate. The value of n_A was calculated for all fixed temperatures as the ratio of the partial integration area of the crystallization peak at the selected temperature T over the total integration area of the crystallization peak. Values of the Avrami parameter with the corresponding type of the reaction mechanism taken from [79] are listed in Table 3.

Table 3 Values of the Avrami parameter n_A for different kind of reaction mechanism

Type of nucleation	Mechanism (dimension)		Growth controlled by	
			Phase-boundary growth	Diffusion
Instantaneous nucleation (saturated sites)	Bulk	1-D growth	1	0.5
		2-D growth	2	1
		3-D growth	3	1.5
	Surface 2-D growth		~2	1
Constant rate growth	Bulk	1-D growth	2	1.5
		2-D growth	3	2
		3-D growth	4	2.5
	Surface 2-D growth		~3	~2

X-ray diffraction

X-ray diffraction could provide us with important data about crystal properties of analyzed materials including cell parameters.

Rays incident to plane-parallel layer can interfere which results into interference fringes as is well known from optics. Because atoms in periodic crystal lattice are arranged in regular position, the set of planes can be interleaved inside the crystal lattice. X-rays are employed since their wavelength is close to the inter-planar distance in crystals. The diffraction of X-rays on the crystal lattice occurs when the well known Bragg's law is satisfied:

$$n_I \cdot \lambda = 2 \cdot d \cdot \sin\theta \ , \tag{12}$$

where n_I is denoted to any integer, λ is the wavelength, d is the inter-planar distance and θ is the angle of incidence. The common reflection setup employs an X-ray cathode emitting X-rays. The emitted rays fall on the sample at a defined angle of incidence θ, diffract on the surface of the sample and then are recorded by the detector. The angle of incidence is varied in a wide range and the signal which is proportional to the intensity of the detected X-rays is recorded. In the case, when the Bragg's law is satisfied, interference of X-rays occurs and the peak is recorded in the spectrum.

Crystallite and grain sizes D can be calculated from the Scherer's equation [80]:

$$D = \frac{k_S \cdot \lambda}{\beta_c \cdot \cos\theta} \ , \tag{13}$$

where k_S is the structural factor equal to 0.89, λ is the X-ray wavelength equal to the excitation wavelength of X-rays, β_c is the correlated full width in half maximum (FWHM) of

analyzed peak and the diffraction angle θ. In general, the smaller is the crystal size the higher is the FWHM of analyzed peak.

Special characterization methods of thin films: Surface profilometry, atomic force microscopy (AFM), spectral ellipsometry (SE)

The surface profilometer used in this work belongs to the group of contact apparatus. A stylus fixed on the piezocrystal is brought into contact with the sample and moved along the sample surface. Variations of the sample surface move the stylus up and down, deforming the piezocrystal. The electrical voltage induced on the piezocrystal due to the deformation corresponds to the surface variation.

Atomic force microscopy is based on the existence of general forces (e.g. attractive, repulsive and electrostatic) between the sample surface and a tip on a cantilever. The cantilever with the tip scans the sample. From the upper side of the cantilever a laser beam is reflected which passes into a detector array. The resultant force deflects the tip and so the cantilever. The deflection of the cantilever is transferred to the deflection of the laser beam increasing the angular resolution. Modulations of the deflection of the laser beam owing to the scanning of the cantilever along the sample correspond to the surface profile of the sample. The surface profile of the sample is reconstructed from individual scans and from measured deflections of the laser beam.

Spectral ellipsometry is an optical method based on the changes of the polarization of linearly polarized light interacting with an analyzed sample. Changes of properties of polarized light reflected on thin films can be expressed by the equation [81]:

$$tg\Psi \cdot e^{i\Delta} = \frac{|R_P|}{|R_S|} \ , \tag{14}$$

where Ψ denotes the amplitude of polarized light reflected on the films, Δ is the phase difference of light ray before and after the reflection, R_P and R_S are the Fresnel's coefficients of reflection for P and S polarization respectively. Parameters Ψ and Δ depend on the film thickness τ, refractive index n and absorption coefficient of optical losses k_L and wavelength of the employed light. Acquired data (see example in Figure 6) can be theoretically analyzed and optical constants can be evaluated by employing suitable mathematical and physical models. The absorption coefficient of the film is related to the absorption coefficient of optical losses k_L by the relationship [81]**:**

$$\alpha = \frac{4\pi}{\lambda} \cdot k_L \ , \tag{15}$$

where α denotes the absorption coefficient of thin film introduced previously, λ is the wavelength, k_L is the absorption coefficient of optical losses resulting from ellipsometric analysis.

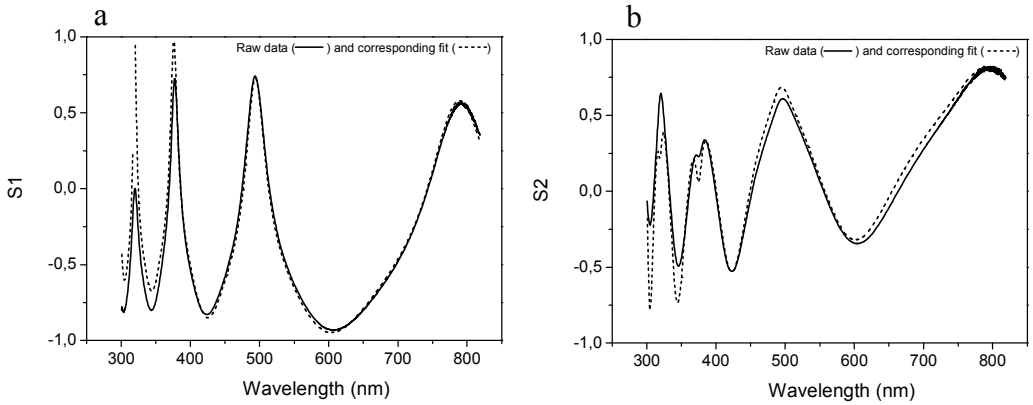

Figure 6 Experimental ellipsometric data for Zn_2TiO_4 thin film on silica substrate expressed in the a) S1 and b) S2 functions and corresponding fits. Analyzed at the angle 65 degrees.

Microscopic methods

Despite its simplicity the drawback of the common light microscopy is in low resolution on the micrometric level. The reason lies in the wave character of light. When the observed objects have a comparable dimensions as used light, the diffraction of light occurs, preventing the observation of objects smaller than one micrometer. The resolution of visualization techniques based on wave propagation can be improved by decreasing the wavelength of the used light. Such an improvement is provided by electron microscopy.

In an electron microscope an electron beam is accelerated by electrostatic field. It is well known that the energy of accelerated electrons is inversely proportional to their wavelength. By such way we can create an electron beam with the selected wavelength. In the transmission electron microscopy (TEM) the accelerated electron beam passes through the sample similarly to light in an optical microscope. In the scanning electron microscopy (SEM) the accelerated electron beam excites secondary electrons from the sample surface which are detected. The beam is scanned around the sample surface allowing thus the imaging the surface. The SEM is routinely combined with an EDS analyzer. An increased energy of the incidence electron beam can impact electrons from the sample surface. The emission of electron is followed by realignment of electrons in atomic shells that is followed by radiation of characteristic rays. The composition of the sample can be determined from properties of these characteristic rays.

Preparation of optical fibers

The technology of active silica optical fibers is based on three step process. In the first step a porous frit is prepared inside a silica tube by the modified chemical vapor deposition. Rare earth elements are introduced into the formed frit that is sintered and together with the silica tube collapsed into a rod, the preform. Finally, the prepared preform is withdrawn into optical fiber.

The general concept of introducing rare earth elements inside the silica frit follows from the widely used solution doping method. The solution containing dissolved ions of rare earth elements is soaked inside the silica frit usually doped by other oxides, such as aluminum oxide [82], the frit is dried and sintered. The final local immobilization, physico-chemical properties and concentrations of rare earth elements incorporated into the frit depend on the affinity of dopants to the frit that can be modified by another dopants [7]. As the preforms and

optical fibers are processed at temperatures above 2000 °C the high thermal stability of compounds in the formed glass is required.

In this work the particular attention was paid to the cubic inverse spinel Zn_2TiO_4. Such an interest was invoked by its high thermal stability and by its ability of forming suitable matrix allowing the incorporation of rare earth elements. The primary intention was exploiting the noted inverse spinel as a part of a novel matrix with incorporated rare earth elements for active optical fibers. An initial sol with a ratio of Zn:Ti equal to 2:1 containing Eu^{3+} was prepared in order to study the immobilization of rare earth elements inside the formed matrix. The sol was soaked into a silica frit and processed to a fiber preform. However, during the thermal treatment of the frit and preform formed compounds pass through the side reaction and decomposition leading to crystal structure of zinc silicate and pyrochlore structure of europium titanate. Hence, other thermally stable compounds should be exploited.

From the phase system ZnO-TiO_2 only the pure oxides fulfill requirements to the thermal stability. As is well known, despite its possible utilization as a host matrix [83], Ti^{4+} ions distributed inside silica matrix of optical fiber cores are partially reduced to Ti^{3+}. Although the concentration of Ti^{3+} is on the level of several ppm, their intensive and broad absorption reduces the transparency of formed material practically to zero in whole visible and near infrared part of spectra. For such reasons zinc oxide nanoparticles doped by Eu^{3+} ions were finally tested for the preparation of fibers.

Characterization of preforms and optical fibers

The refractive index profile is a fundamental parameter of preforms and optical fibers. It can be calculated from the deflection of light scanning transversally through the preform immersed into an immersion with the silica-matched refractive index. The preform core acts as an optical lens deflecting light according to the lens maker's equation. The final deflection depends on the refractive index of the preform core and local curvature of the core. The result of this measurement is the so called deflection function expressing the deflection between the detected position of the beam captured by the detector and the initial axial position of the laser beam. The refractive index profile is calculated from this deflection function.

The numerical aperture is the principal parameter of optical fibers representing the maximal angle below which each ray entering the input fiber face is transmitted through the fiber by the total internal reflection. It can be calculated from the difference between the refractive indexes of the core and cladding of the optical fiber according to the equation:

$$NA = \sqrt{n_{core}^2 - n_{cladding}^2} \ , \tag{16}$$

where NA means the numerical aperture, n (core/cladding) is the refractive index of the fiber core and cladding respectively. For the standard technology of silica optical fibers, the refractive index of the cladding is equal to the refractive index of the silica glass, i.e. 1.457 (at 630 nm).

In this thesis the numerical aperture was also determined from angular distributions of the output optical power from an optical fiber excited by a collimated laser beam. These distributions were measured on a custom-made apparatus. In the measurements the front face of analyzed fiber is put into a rotation axis of a goniometric cantilever with a fixed laser diode. The end-face of the analyzed fiber is fixed in a photo detector. The cantilever rotates around the rotational axis varying the angle of incidence of light illuminating the front face of the fiber. The detected signal is recorded as a function of the intensity on the angle of incidence of light from the laser diode.

Preparation of samples

From many approaches resulting into the formation of $Zn_xTi_yO_z$ structures, the cluster process and direct heteronucleation approach were chosen. The cluster process was chosen for its relative simplicity. The process based on the direct heteronucleation extends the method previously elaborated in our laboratory [37]. This new method allows us to prepare $Zn_xTi_yO_z$ structures with any required ratio of zinc to titanium. The general chart of the selected approaches is depicted in Figure 7.

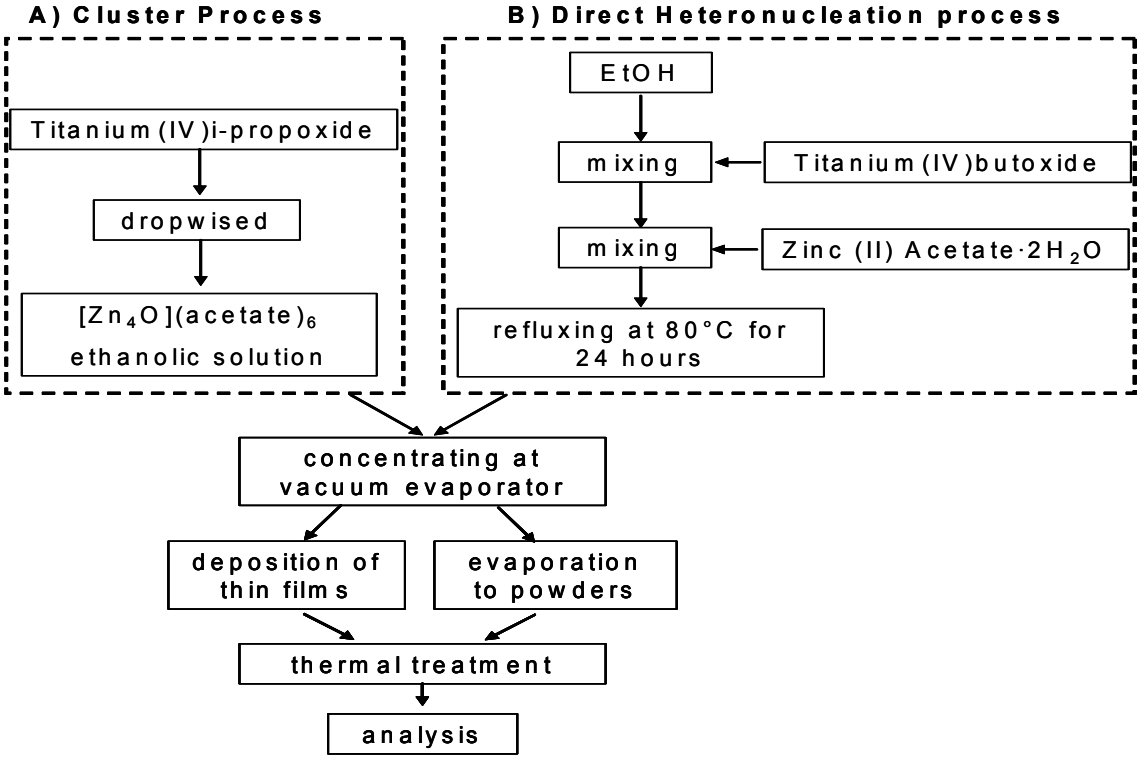

Figure 7 Schematic flow chart of employed synthesis and sample processing

List of used chemicals and materials

All chemicals used in this thesis were purchased from standard providers. Highly pure precursors were used as received without further purification. They are listed in Table 4.

Pyrex glass substrates were purchased from Optic-C company (France). Finally, polished silicon wafers (P-type, doped by boron, orientation <100> , resistivity >10 k·Ω·cm) were purchased from Si-Mat company (Germany).

The substrates were carefully cleaned before use. They were subsequently sonicated in the solution of Elma cleaner (Sigma-Aldrich) mixed with deionized water in a volume ratio 1:5. The cleaned substrates were sonicated and washed up by copious amount of deionized water followed by rinsing by ethanol and blowing by nitrogen to prevent the irregular evaporation of the solvent.

A silica frit, optical preform and optical fiber were prepared in the Institute of Photonics and Electronics AS CR, v.v.i. by standard procedures according to the recipe N° SG 1069 (not included as the part of the thesis).

Table 4 List of chemicals used for synthesis

Name	Used formula/abbreviation	Purity/Grade	Provider
ethanol	C_2H_5OH	Spectranal, absolute	Sigma-Aldrich
europium nitrate pentahydrate	$Eu(NO_3)_3 \cdot 5H_2O$	99.9%	Aldrich
erbium nitrate pentahydrate	$Er(NO_3)_3 \cdot 5H_2O$	99.9%	Aldrich
thulium nitrate pentahydrate	$Tm(NO_3)_3 \cdot 5H_2O$	99.9%	Aldrich
tetramethylammonium hydroxide	TMAH	25 wt. % solution in methanol	Aldrich
titanium(IV)i-propoxide		purum	Fluka
titanium(IV)butoxide		purum	Fluka
zinc acetate dihydrate	$Zn(acetate)_2 \cdot 2H_2O$	ACS reagent	Fluka

Synthesis of precursors

Synthesis of $[Zn_4O](acetate)_6$ clusters

Zinc oxo-acetate clusters of the general formula $[Zn_4O](acetate)_6$ were prepared by the thermal dehydratation of zinc acetate dihydrate in ethanolic solutions [27].

In this process $Zn(acetate)_2 \cdot 2H_2O$ was dispersed in ethanol. The formed mixture was heated up to 85 °C in an evaporator under a regular stirring forming a transparent solution. The solutions was evaporated to about half of the initial volume, then cooled down and diluted by ethanol to the concentration of 0.1 $mol \cdot l^{-1}$. The initial amounts of the particular components are summarized in the Table 5.

Table 5 Initial conditions employed in the synthesis of precursors

	Precursor	
	$[Zn_4O](acatate)_6$ clusters	ZnO nanoparticles
$m_{Zn\ Acetate \cdot 2H_2O}$ (g)	4.38	4.4
$V_{ethanol}$ (cm^3)	200	40
$m_{Eu(NO_3)_3 \cdot 5H_2O}$ (mg)	-	452
V_{TMAH} (cm^3)	-	9

Synthesis of ZnO nanoparticles doped by Eu^{3+} ions

Zinc oxide nanoparticles doped by Eu^{3+} ions were prepared by the modified method employing the thermal condensation of $Zn(acetate)_2 \cdot 2H_2O$ into zinc oxide particles followed by desaggregation of the formed particles by tetramethylammonium hydroxide [36].

In experiments europium salt was dissolved in ethanol. Then $Zn(acetate)_2 \cdot 2H_2O$ was dispersed in the solution in an ultrasonic bath. The formed mixture was overheated up to 130 °C. Approximately one tenth of the formed mixture was evaporated, then the mixture was cooled down. Finally, the 25 wt. % methanolic solution of tetramethylammonium hydroxide was added into the mixture. The mixture was regularly stirred at ambient temperature forming the transparent solution. Initial amounts of the used components are summarized in Table 5.

Synthesis of heterosols

Cluster process

The cluster process route is based on the condensation of highly reactive $[Zn_4O](acetate)_6$ clusters with titanium(IV)i-propoxide at ambient temperature. In this route, the required volume of titanium(IV)i-propoxide was added drop wise into a freshly prepared solution of $[Zn_4O](acetate)_6$ clusters under regular stirring. The formed solution was heated at 50 °C under regular stirring for 30 minutes and aged at ambient temperature for 24 hours. The aged sols were purified by filtration trough a 0.2 μm PTFE membrane and concentrated under vacuum to the required concentration.

Optionally, 1 at. % of europium nitrate pentahydrate (with respect to the overall content of Zn and Ti) was dissolved in the solution of $[Zn_4O](acetate)_6$ clusters prior to the addition of titanium(IV)i-propoxide. Reaction parameters of such a synthesis are summarized in Table 6.

Table 6 Initial composition employed in the cluster process

Ratio Zn:Ti	2:1	1:1	2:3
$V_{clusters}$ (cm^3)	50	50	50
$V_{ethanol}$ (cm^3)	4,29	3,52	2,78
$V_{Ti(IV)(i\text{-}propoxide)}$ (cm^3)	0.74	1.48	2,22
$m_{Eu(NO_3)_3 \cdot 5H_2O}$ (mg)	32,7	43,1	66,5
c_{max} ($mol \cdot l^{-1}$)	0,3	0,3	0,5

Direct heteronucleation process

The direct heteronucleation process is a single batch process based on the reaction of zinc acetate dihydrate with titanium(IV)butoxide in ethanolic solution. Zinc acetate dihydrate dissolved in ethanolic medium undergoes the thermal decomposition according to the following reaction [21, 37, 84]:

$$4\ Zn(Acetate)_2 \cdot 2H_2O \rightarrow [Zn_4O](Acetate)_6 + 7\ H_2O + 2\ HAcetate\ . \quad (17)$$

The liberated acetic acid enables the complexation of titanium ions. Simultaneously, the esterification of the liberated acetic acid occurs. The liberated water allows the hydrolysis of titanium butoxide followed by the heteronucleation.

In this thesis titanium(IV) butoxide was dissolved in ethanol. and then the required amount of zinc acetate dihydrate was suspended in the solution. The solution was refluxed at 85 °C for 24 hours passing into a transparent solution. This solution was cooled down to ambient temperature.

Optionally, 1 at. % of europium nitrate pentahydrate was added into solution. The prepared sols were purified by filtration through a 0.2μm PTFE membrane and concentrated under vacuum to a required concentration. Details about the concentration of particular components are shown in the Table 7.

To estimate solubility limits in the Zn_2TiO_4 structure, the initial sols were optionally doped by varying amount of europium, erbium or thulium nitrate pentahydrate reaching the concentration of REE from 0 to 5 at. % (with respect to the overall content of cations).

Table 7 Initial composition employed in the direct heteronucleation process

Ratio Zn:Ti	2:1	1:1	2:3
$m_{Ti(IV)butoxide}$ (g)	2.23	5.38	16
$V_{ethanol}$ (cm^3)	125	60	60
$m_{Zn\ Acetate \cdot 2H_2O}$ (g)	2.88	3.47	6.89
$m_{EuNO_3 \cdot 5H_2O}$ (mg)	85.0	136.8	339.1
c_{max} ($mol \cdot l^{-1}$)	0,57	0,75	>1

Preparation of xerogels

The prepared sols were used for the deposition of thin films or evaporated under the vacuum forming thus bulk xerogels. The chemical composition of the prepared bulk xerogels was verified by the EDS analysis. Results, summarized in Table 8, are in a good agreement with the chemical composition of the starting sols. The bulk xerogels were heated with a constant heat-rate of 10 °C·min^{-1} to a selected temperature where they were kept for 30 minutes according to the chart in Figure 8a and then cooled down to ambient temperature.

Table 8 EDS analysis of sintered zinc titanate pellets

Ratio Zn:Ti		2:1	1:1	2:3
Cluster process	c Zn (at.%)	67.2	51.4	39.7
	c Ti (at.%)	32.8	48.6	60.3
	Ratio Zn:Ti	2.05	1.06	1.98
Direct heteronucleation	c Zn (at.%)	65.74	52.41	40.52
	c Ti (at.%)	34.26	47.59	59.48
	Ratio Zn:Ti	1.92	1.1	2.04

Deposition of thin films

Films were deposed on the pre-cleaned substrates by the dip-coating method employing a commercial dip-coater (ID-Lab, CR) allowing to precisely control the withdrawing speed. The substrate was immersed into a sol for 60 seconds, withdrawn by the speed varying from 10 to 30 $cm^3 \cdot min^{-1}$ according to the viscosity of the applied sol. The films were heated with a constant heating rate of 10 °C·min^{-1} up to 350 °C, annealed at this temperature for 10 minutes in order to burn out remaining organic matter and then cooled down to ambient temperature. The deposition was repeated two times. Finally, the prepared films were annealed at 650 °C for 10 minutes. The chart of the multideposition process is shown in Figure 8b.

Preparation of optical fibers

A sol of ZnO nanoparticles doped by 5 at. % Eu^{3+} ions was soaked into a silica frit applied onto the inner wall of a silica tube and aged for 12 hours. Than the sol was removed and the frit was heat treated with a constant heating rate 10 °C·min^{-1} to 350 °C and annealed for 3 hours. Then the tube with the soaked frit was cooled down and the process was repeated. Finally, the frit was annealed at 650°C for 24 hours under the oxygen flow 50 $cm^3 \cdot min^{-1}$ in order to burn out remaining parts of organic matter. The chart of the deposition process is summarized in Figure 8c

The soaked frit was thermally treated according to the internal recipe N° SG 1069. The recipe includes the sintering at temperatures to 1800 °C and preform collapse at temperatures

in a range 2200-2300 °C. The prepared optical preform was characterized and withdrawn into the optical fiber.

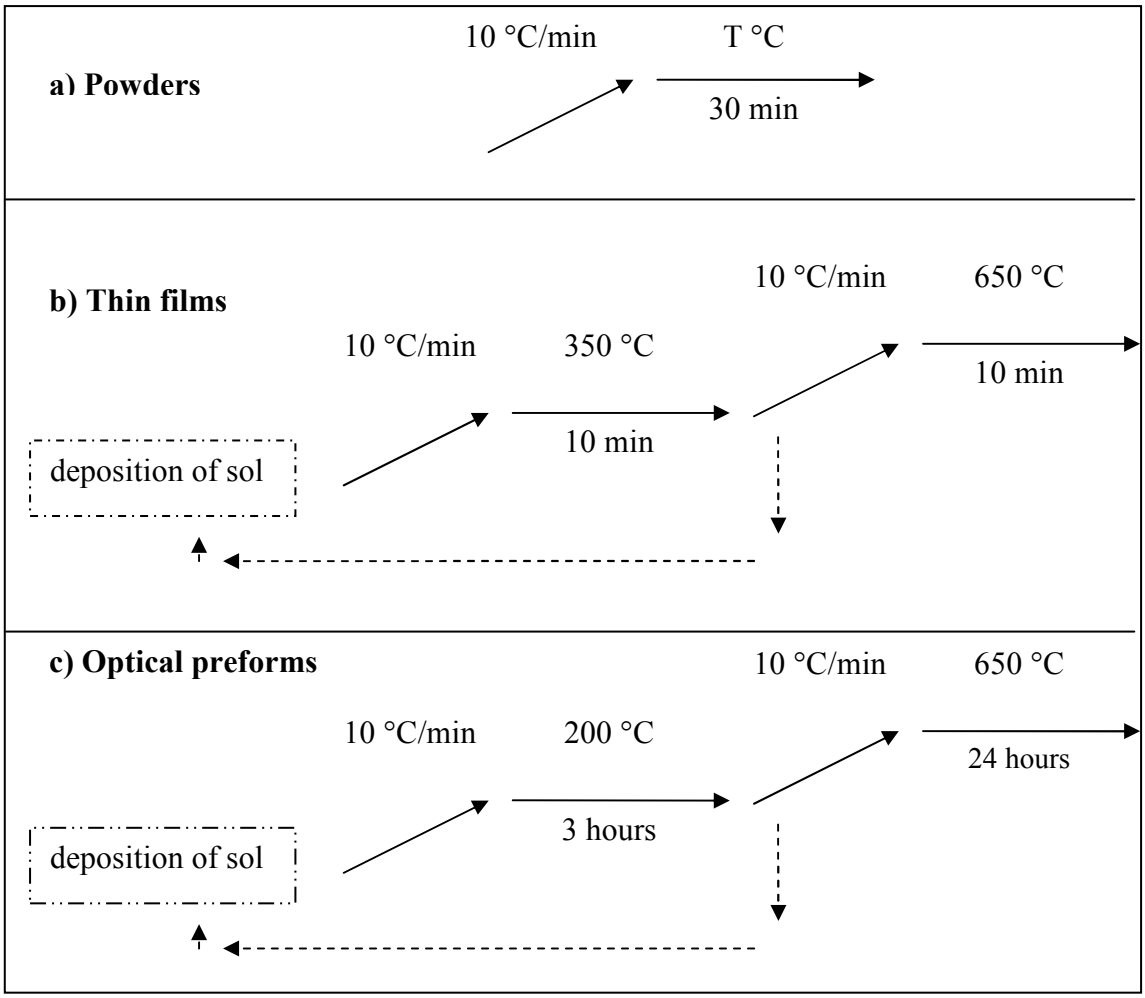

Figure 8 Flow chart of thermal processing of a) powder , b) thin films, c) optical preforms

Experimental equipment and methods

Data processing

Except denoted cases, acquired data were processed and evaluated by the Origin8.1 software. Error bars of calculated values were evaluated as a standard deviation of collected data or standard deviation of fitted curves.

Thermal analysis and mass spectrometry

The burnout and crystallization properties of the prepared powders were analyzed by differential thermal analysis (DTA), thermogravimetry (TG) and differential scanning calorimetry (DSC) followed by mass spectrometry (MS) and infrared spectroscopy (FT-IR). The DTA, TG, DSC and MS measurements were carried on a Netzsch STA449C multifunctional apparatus. To determine the liberation of organic compounds during the heat treatment some powder samples were analyzed by the DSC method coupled with MS at a heating rate of 10 °C·min^{-1} up to 800 °C under a nitrogen flow of 50 cm^3·min^{-1}. Crystallization properties of the prepared powders were determined by the DSC analysis of the powder samples pre-treated at temperatures to 400 °C in air in order to evaporate volatile fractions of organic compounds. These samples were further treated at different heating rates from 15 to 30 °C·min^{-1} under an oxygen flow of 50 cm^3·min^{-1}. In all these experiments approximately 10 mg of powder samples was used.

UV-VIS spectroscopy

Absorption spectroscopy

Optical absorption spectra of the prepared sols and thin films were measured using a Varian CARY 5 apparatus operating in the transmission set-up. Diffuse reflectance spectra of the powder samples were recorded with a UV-VIS CARY 100 spectrophotometer. Absorption spectra of optical fibers were measured by the cutback method using a fiber optic set-up including an Ocean Optics PX-2 xenon lamp as a light source and Ocean Optics SD 2000 CCD double channel spectrometer as a detector. The reference signal was coupled out from the light source, attenuated and joined into the reference channel of the detector.

Fluorescence spectroscopy

Photoluminescence spectra of the prepared nanopowders were recorded at a room temperature using a Jobin-Yvon HR1000 double grating monochromator equiped with a photomultiplier. A 450W xenon lamp with light that passed through a monochromator (Jobin, HR320) was used as the excitation source. The emission spectra of heat-treated powders were recorded between 400 nm and 800 nm to proof the lack of Eu^{2+} ions in the heat-treated samples. The asymmetry factor $R(J_2/J_1)$ was calculated as the ratio of integral intensities belonging to peaks of electronic transitions $^5D_0 \rightarrow {}^7F_2$ and $^5D_0 \rightarrow {}^7F_1$.

Vibrational spectroscopy

FT-IR spectra of the prepared powders were recorded with a Bruker Vector 22 spectrometer operating in the transmission set-up. At these measurements, approximately 4

mg of the powder was mixed with 200 mg of KBr finely pulverized in a mortar and pressed into a pellet. The blank sample made of pure KBr was used as the reference.

X-ray diffraction analysis

The XRD structural analysis of the prepared powders was performed on a Bruker D8 diffractometer with the Bragg-Brentano geometry operating with the Cu-Kα radiation (λ=1.54056 Å, operating voltage 40 kV, current 40 mA, integration time 200 ms). Recorded data were evaluated by the Origin 8.1. Diffraction peaks were fitted by the Gaussians curves to calculate the full-width at half-maximum (FWHM) values. The instrumental broadening of the peaks was correlated to the diffraction peak of KCl (ACS, Sigma-Aldrich) corresponding to the (200)-plane. Crystallite and grain sizes D were calculated from the Debye-Scherrer's equation. Particular phases were identified on the basis of the JCPDS database. In addition to JCPDS data files listed in Table 1 and Table 2, the following records were utilize to identify formed structures:
N° 23-1072, 18-0499 and 23-0590, for $Eu_2Ti_2O_7$, $Er_2Ti_2O_7$ and $Tm_2Ti_2O_7$, respectively. To clarify crystallization processes, the volume fraction of a particular crystalline phase was evaluated from the measured XRD spectra by using formula [85]:

$$Volume\_fraction(\%) = \frac{S_{phase}}{S_{allpeaks}} \cdot 100 \ , \tag{18}$$

where S_{phase} is the integral area of XRD peaks belonging to the evaluated phase and $S_{allpeaks}$ is the integrated area of all XRD peaks of overall XRD record.

Characterization by electron beams

SEM images of the sintered powder samples and thin films were taken with a JOEL JSM 6301 F or Philips XL30 ESEM electron microscope. The images taken on the Philips microscope are marked by the black labels. The overall chemical composition of selected samples was verified by elemental analysis on a JEOL JSM 6400 electron microscope equipped with an Oxford instrument EDS analyzer. The chemical compositions of individual grains were measured on the powders heat-treated to 1200 °C for 24 hours by a Cameca SX100 electron microprobe. A thin palladium layer was sputtered onto the samples prior to the analysis to prevent samples charging.

Other characterization of thin films

The thickness of films was measured on the edge between the film and the uncoated substrate by a stylus-based surface profiler Tencor Alfa step 500.

The surface morphology was analyzed by the AFM (Digital Instruments/Veeco, Woodbury, NY) in the contact mode using a Dimension 3100 AFM operated in air. Commercial Si_3N_4 cantilevers (DI) with an elastic modulus of $0.56 \cdot N \cdot m^{-1}$ were used. The surface variation was evaluated by the RMS factor representing the standard deviation of the Z-axis. Acquired data were evaluated and visualized by the nanoscope 6.13R1 software.

Spectral ellipsometry measurements were carried on a Sentech 850SE spectral ellipsometer equipped with focusation micro objectives. Heat treated thin films were analyzed in a spectral range from 300 to 800 nm with a 1 nm step at angles of incidence of 60, 65 and 70 °. The refractive index and absorption coefficient were calculated employing the build-in Spectraray software. Acquired data were analyzed using a model of a single layer on a silica glass substrate and the Cauchy's dispersion relations expressed by the equations [69]:

$$n(\lambda) = A_c + \frac{B_c}{\lambda^2} + \frac{C_c}{\lambda^4} \quad , \tag{19}$$

$$k_L(\lambda) = D_c + \frac{E_c}{\lambda^2} + \frac{F_c}{\lambda^4} \quad . \tag{20}$$

where n represents the refractive index of the layer, k_L is the absorption coefficient of optical losses, λ is the wavelength and A_c, B_c, C_c, D_c, E_c and F_c are fitted constants. The roughness of the surface at the level of 5 nm was taken into account in calculations.

Characterization of preforms and optical fibers

Refractive-index profiles of the preforms were measured on an A2600 Photon Kinetics apparatus equipped with a HeNe laser beam as the light beam.

The angular distribution of the output power from the optical fiber was measured by the custom-made apparatus equipped with a laser diode operating at 633 nm. The rotation step was 0.05 degrees. Light passing through the fiber was detected by a PIN photo detector. Typically about 5 m of the optical fiber was employed in the measurements.

Results and discussion

Preparation and properties of $Zn_xTi_yO_z$ nanostructures

Properties of formed heterosols

Both selected approaches, i.e. cluster process and direct heteronucleation, provide us with fully transparent sols with the long term stability. The sols can be concentrated up to the maximal concentrations indicated in Table 6 and Table 7. Surpassing the maximal concentration leads to the formation of a white colloidal solution which is followed by the aggregation and sedimentation of white powder which was identified as zinc oxide. As the formed sols are relatively complex mixtures, classical techniques of vibrational spectroscopy failed in the attempt to clarify binding properties of their particular components. However, several conclusions can be deduced from analysis of the xerogels as will be discussed later.

The critical concentration of the sols prepared by the cluster process is practically half of that of the sols prepared by the direct heteronucleation. Such a behavior should be attributed to the presence of free aggregated $[Zn_4O](acetate)_6$ species and to the preferred complexation of acetates to titanium ions as will be demonstrated later.

UV-VIS absorption spectra of the prepared sols are shown in Figure 9. The determined values of the extinction coefficients of the prepared sols are significantly smaller than those

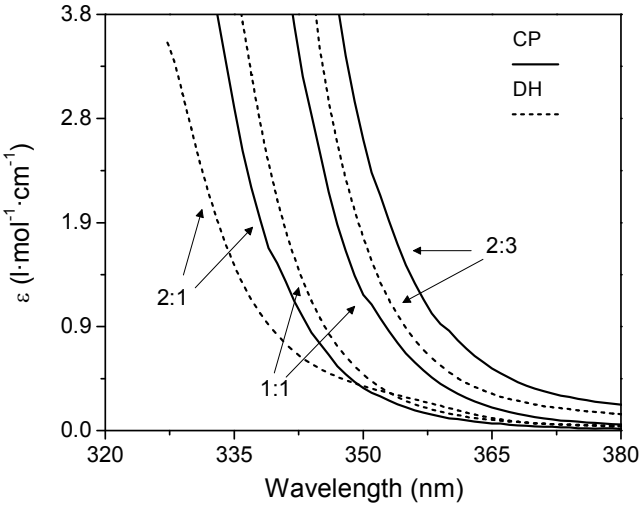

Figure 9 Optical absorption spectra of the sols prepared by the cluster process (CP) and by the direct heteronucleation (DH). Concentration was 1 mol·l^{-1} related to the sum of cations

reported for colloidal solutions of nanocrystalline materials [21, 27, 37]. This result can reflect the fact that the formed sols consist of polymolecular clusters not aggregated nanoparticles. The absorption edges in Figure 9 appear a significant red shift with an increasing content of titanium ions. This phenomena is more obvious for the sols prepared by the cluster process. This conclusion indicates the higher aggregation of Ti-O-Ti chains in the mixture which naturally reflects the higher reactivity of titanium(IV)i-propoxide employed as the precursor.

Burn-out behavior of xerogels and thin films

The thermal treatment of sol-gel based materials is complex process including the decomposition of organic compounds, various chemical reactions and crystallization

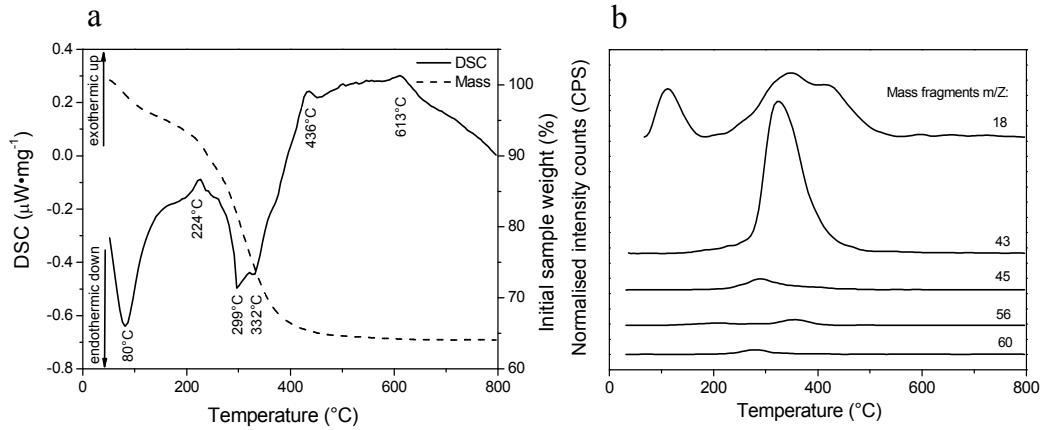

Figure 10 a) DSC-TG curves of Zn_2TiO_4 sample containing 1at.% of Eu and b) corresponding MS spectra for selected fragments. Heating rate 10 K·min^{-1}. N_2 flow 50 cm^3·min^{-1}.

processes. The thermogravimetric analysis of the powder with the ratio Zn:Ti equal to 2:1 is demonstrated in Figure 10a. The thermogravimetric curve indicates two main mass losses which can be linked with two endothermic peaks on the DSC curve. According to the MS results (see Figure 10b) the first step bellow 130 °C can be attributed to the evaporation of water (m/Z=18) and volatile compounds such as residual ethanol. The second step in a temperature range from 224 to 430 °C can be related to the second broad endothermic peak and it is accompanied by liberation of water (m/Z=18) and organic ligands based on acetate fragments such as acetic acid (m/Z=43, 45, 60) and butyl acetate (m/Z=43, 56). The decomposition of organics is followed by slow dehydration and can be related to the third endothermic peak at 456 °C. Finally, the crystallization of Zn_2TiO_4 occurs at 613 °C.

The MS record was followed by the FT-IR measurements to verify the character of the

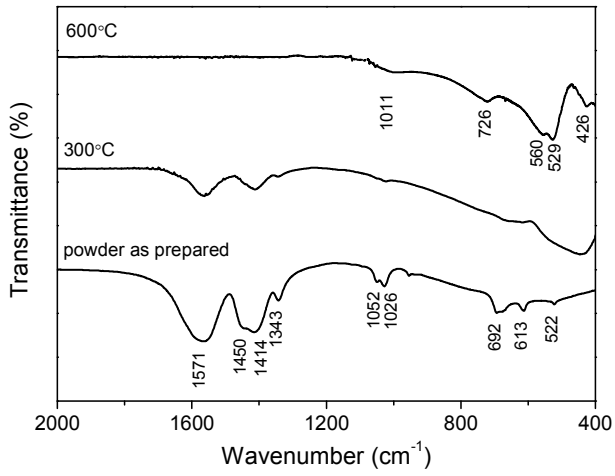

Figure 11 FT-IR spectra of Zn_2TiO_4 powders heat-treated at different temperatures.

liberated organics and coordination modes of organic ligands toward central atoms (see Figure 11). As expected the prepared powders contain large amount of organic materials. Absorption bands linked with CH_3- organic group can be found at 1026, 1052 cm^{-1} representing CH_3 rock vibrations, at 1343 cm^{-1}, 1414 cm^{-1} representing $\delta_s(CH_3)$, $\delta_{as}(CH_3)$ [83] respectively. Bands at 522, 613 and 692 cm^{-1} can be attributed to γ(COO), π(COO) and α(COO) respectively [37, 86].Two broad bands centered around 1450 and 1571 cm^{-1} are attributed to the stretching vibrations of carboxylic groups coordinated on metal ions [87]. From the difference between the position of bands corresponding to asymmetric (1565, 1550-1590 cm^{-1} for Zn and Ti respectively) and symmetric (1450, 1414 cm^{-1} for Zn and Ti resp.) vibrations of COO^- groups one can estimate the presence of bridging bidentate ligands bonded to Ti and chelating bidentate ligands bonded to Zn ions [86, 87]. Partial charge-δ calculations on acetate capped Zn- and Ti-oxoacetates show that δ(Ac) connected to less electropositive Zn is around -0.2 whereas δ(Ac) connected to Ti drops to -0.5 indicating a higher thermodynamic stability of Ti-acetate complexes.

The FT-IR spectra show that by increasing the temperature, organic ligands are gradually burned out and corresponding absorption bands diminish (see Figure 11). Acetates coordinated to Zn ions are burned out at lower temperatures than ligands attached to Ti ions which can be drawn from the practically disappeared absorption band at 1450 cm^{-1} attributed to acetates bonded to Zn ions and from comparison with the absorption band of acetates bonded to Ti ions at 1414 cm^{-1} at 400 °C. Thus, at this temperature mainly bridging bidentate ligands bonded to Ti ions remain in the mixture. These measurements explain why the traces of ZnO can be formed prior to the crystallization of Zn_2TiO_4 due to the easier accessibility of zinc ions. Once the crystallization takes place and periodic structure of the crystal lattice is formed bellow 600 °C, new sharp absorption bands related to $[TiO]_6$ and $[ZnO]_4$ groups [64, 88, 89] appear in FT-IR spectra. These conclusions are in excellent correlation with the DSC-TG measurements demonstrated in Figure 12. The increasing

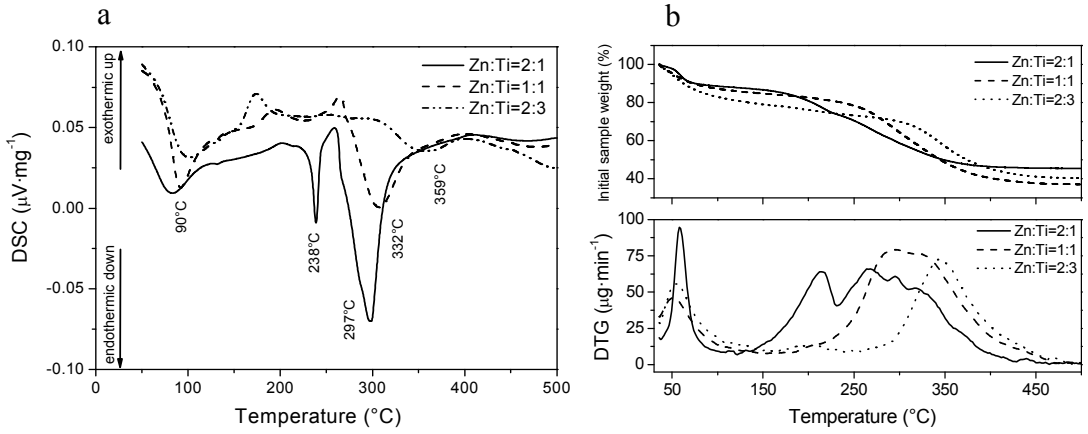

Figure 12 Thermal analysis of amorphous xerogels prepared by cluster process for different Zn:Ti ratios. a) DSC data and b) corresponding TG and DTG curves. Heating rate 10 $K \cdot min^{-1}$. N_2 flow 50 $cm^3 \cdot min^{-1}$.

amount of Ti ions in the bulk xerogel regularly shifts the position of DSC peaks to higher temperatures. The evaporation of volatile organic compounds bellow 150 °C is followed by burnout of organic ligands. The peak appearing at 240 °C should be attributed to burnout of acetates coordinated to Zn and is followed by the peak at about 400 °C which corresponds to the burnout of acetates coordinated to Ti. All organic materials are burned out bellow 400 °C and the nanocrystallization process of ternary structures is initiated.

Although the presented data explicitly clarify the burnout behavior of the prepared xerogels, the question remains about the burnout behavior of thin films. Despite the same chemical composition of the deposited layers and bulk xerogels, the different structure of these samples can significantly modify the physico-chemical properties during the thermal annealing. Namely, the mass transfer will be significantly different in bulk xerogels and thin films. To estimate the difference between the powder and thin films the sol was dropped on a fragment of a silicon wafer forming a thin layer with the thickness of about 200 nm and broken apart. The part of the sample was thermally analyzed by the DSC method. The other part was subsequently heat-treated up to 350 °C and analyzed by the FT-IR spectroscopy. Despite the fuzzy course of the DSC curve for the sample with the ratio Zn:Ti equal to 2:3

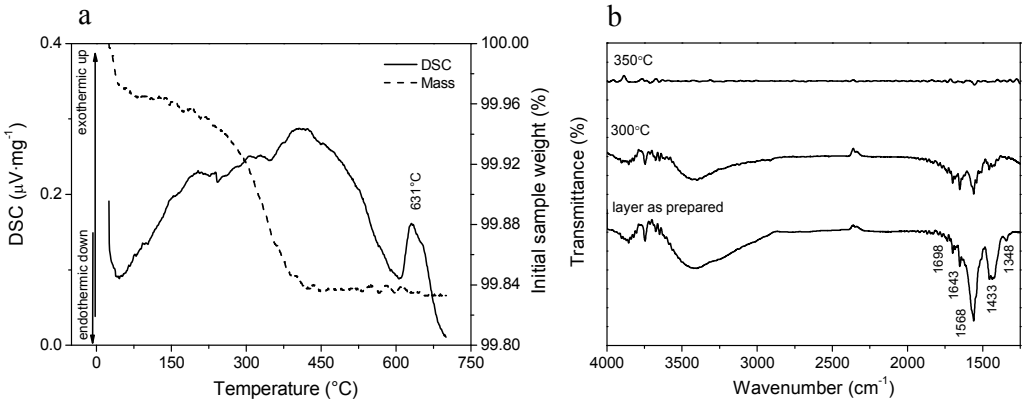

Figure 13 Burnout behaviors of thin films. Approximately 200 nm thick layer of the initial composition Zn:Ti=2:3 coated on the silicon substrate. a) DSC-TG analysis. Heating rate 5 K·min^{-1}. O_2 flow 100 cm^3·min^{-1}., b) FT-IR spectroscopy of the heat-treated film

demonstrated in Figure 13a, the TG curve appears a slight shift of about 20 °C to lower temperatures comparing to the analyzed powder. The peak appearing at 631 °C belongs to the crystallization of TiO_2 as will be discussed later. Although the thickness of the analyzed layer is relatively small, FT-IR spectra in Figure 13b show strong absorption peaks of acetates groups and remaining organic matter which regularly disappear with increasing heat-treating temperatures. All organic material contained in the layer is completely burned out bellow 350 °C. From the practical point of view one can estimate such a temperature as an optimum for the thermal annealing of particular layers in the multideposition process of thin films.

Thermal evolution of $Zn_xTi_yO_z$ nanostructures

In following chapters the global thermal evolution of ternary structures followed by the XRD analysis will be discussed. Since in preliminary experiments it has been found that the global evolution of the formed structures is similar for both selected sol-gel approaches, i.e. cluster process and direct heteronucleation, general results will be demonstrated on XRD data obtained for the samples prepared by the direct heteronucleation process for particular ratios of zinc over titanium in compounds. Moreover, the cluster processing leads to ternary phases containing indispensable traces of side formed structures such as ZnO and exhibits worse morphology of formed nanocrystals. The XRD data for samples prepared by the cluster process are presented in Appendix 1. As the presence of 1 at. % of Eu^{3+} ions in starting xerogels dramatically changes crystallization properties, graphs representing the thermal evolution of the undoped samples and samples containing 1 at. % of Eu^{3+} ions will be compared. The following abbreviations are denoted to particular sol-gel approaches leading to

the initial xerogels: DH –direct heteronucleation, DDH –direct heteronucleation with introduced 1 at. % of Eu^{3+} ions, CP –cluster process, DCP –cluster process with introduced 1 at. % of Eu^{3+} ions.

Ratio Zn:Ti equal to 2:1, Zn_2TiO_4 nanocrystals growth

The crystallization of amorphous xerogels prepared by the direct heteronucleation takes place around 500 °C as can be seen from Figure 14a. Heat-treated powders contain the inverse spinel phase Zn_2TiO_4 and negligible amounts of ZnO. With the consecutively raising

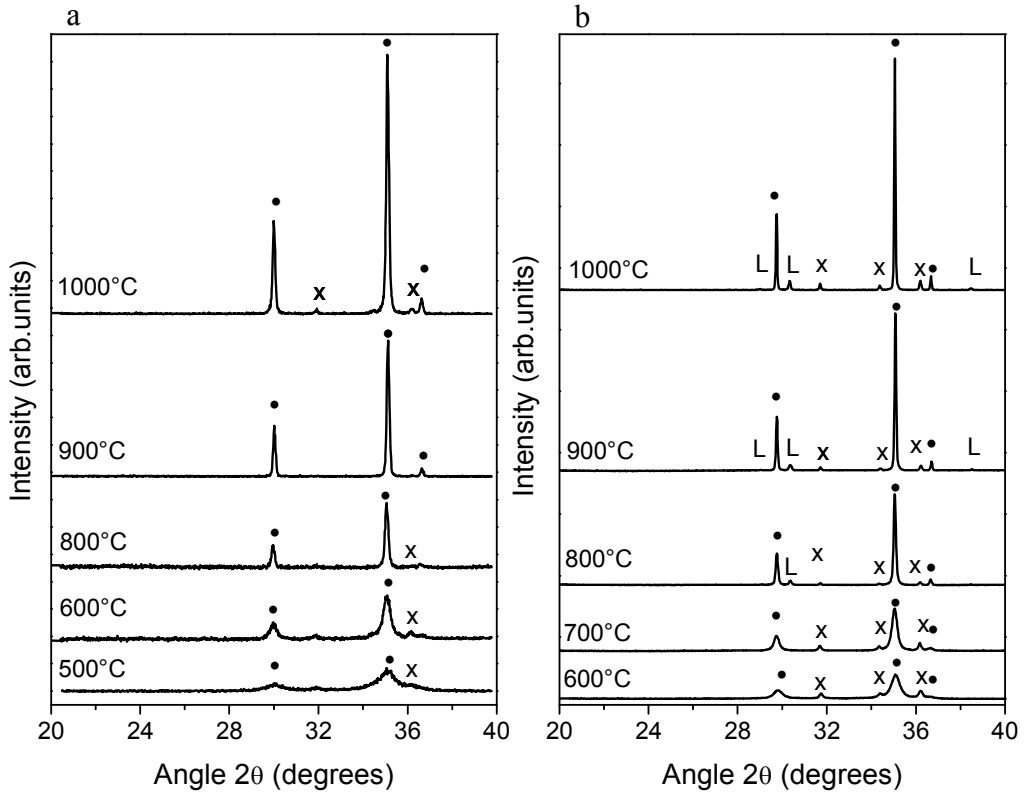

Figure 14 XRD patterns depicting the nanocrystals evolution of xerogels prepared by the direct heteronucleation for the ratio Zn:Ti=2:1. a) undoped xerogels, b) xerogels doped by 1 at.% of Eu ions. Denoted symbols: (●) Zn_2TiO_4, (x) ZnO, (L) $Eu_2Ti_2O_7$.

temperature the spinel phase progressively grows without any further phase separation. At the same time, the amount of hexagonal wurtzite ZnO practically completely disappears.

The presence of europium ions in quantities around 1 at. % partially changes the evolution of the xerogel crystallization as one can see from Figure 14b. The crystallization of ternary phases is shifted to higher temperatures and the amount of side formed ZnO is significantly increased. At 800 °C a new crystalline phase of pyrochlore type $Eu_2Ti_2O_7$ appears. A slight shift of the diffraction lines of Zn_2TiO_4 to smaller 2θ values can be observed. This shift can be explained by the expansion of interplanar distances due to incorporation of Eu^{3+} ions inside the Zn_2TiO_4 lattice. The solubility of rare earth elements inside the inverse spinel lattice will be discussed later.

Figure 15 displays sizes of formed Zn_2TiO_4 nanocrystals calculated on the basis of the Debye-Scherrer's equation as the function of the annealing temperature. The calculated sizes

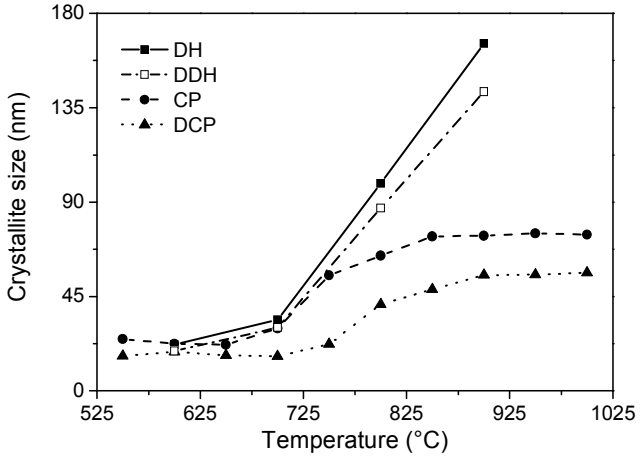

Figure 15 Temperature dependence of Zn_2TiO_4 nanocrystals size on the sintering temperature for particular approaches Sizes calculated by the Debye-Scherrer's equation.

were verified by the SEM observation. Typical results are demonstrated in Figure 16. Inherently, the nanocrystal size regularly grows with increasing the temperature. The average size of nanocrystals formed at 600 °C is around 30 nm (see Figure 16a) for the sample prepared by the direct heteronucleation process. In addition to shifting the crystallization to higher temperatures, the presence of Eu^{3+} suppresses the nanocrystals growth and increases the uniformity of the prepared nanocrystals. Such a phenomena is obvious at higher temperatures where the size of the formed grains exceeds one micrometer (see Figure 16b,c), although the size of doped samples remains on the level of three hundreds of nanometers (see Figure 16d).

From the calculated sizes in Figure 15 one can deduce that smaller nanocrystals can be achieved by the cluster process. However, these results also show a high portion of side formed phases and worse uniformity of the formed nanocrystals. Several phases such a ZnO, c-$ZnTiO_3$ and r-TiO_2 were detected in the formed material. Such an observation combined with the observed low growth rate of the formed nanocrystals suggests a hypothesis that the introduced cluster process has a character of solid state reactions between ZnO and TiO_2 clusters. Such clusters can be formed by incomplete reaction between $[Zn_4O](Acetate)_6$ and its higher homologues with titanium(IV) i-propoxide during the nucleation processes in the initial sol. Titanium(IV) i-propoxide partially condensates forming polymolecular $Ti_xO_y(OH)_z$ species which co-exist with pre-formed $[Zn_4O](Acetate)_6$ clusters. Consequently, after burning out organic ligands from xerogels, the crystallization of hexagonal form of ZnO takes place at 450 °C. The formation of inverse spinel Zn_2TiO_4 occurs that is concurrent to the crystallization of defect spinel c-$ZnTiO_3$. Such a compound is decomposed above 900 °C to Zn_2TiO_4 and r-TiO_2 according to our observation.

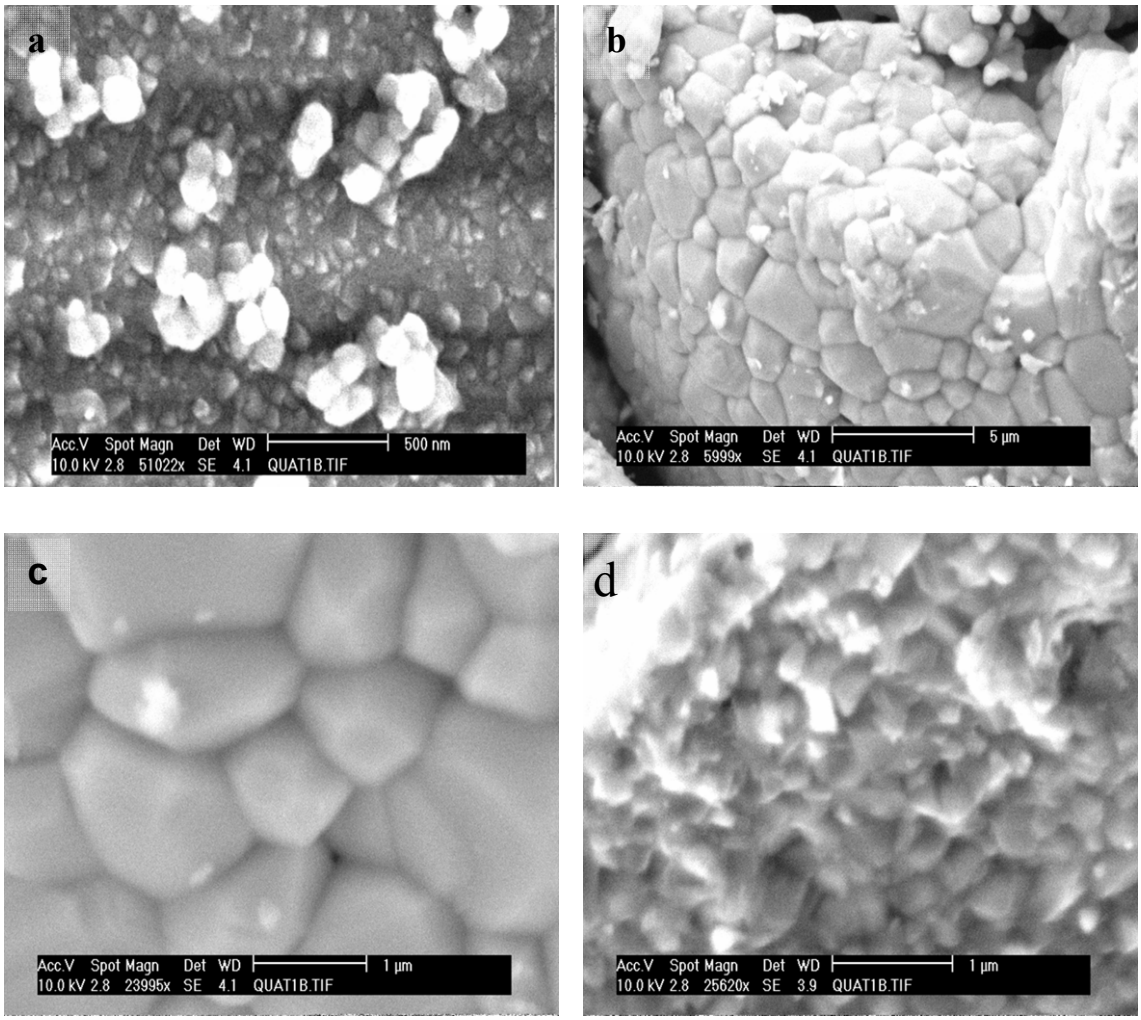

Figure 16 SEM images of overall surface of heat-treated powders. Undoped Zn_2TiO_4 heat-treated at a) 600°C, b) 1000°C and the zoom of c) undoped Zn_2TiO_4, d) Zn_2TiO_4 doped by 1 at.% of Eu^{3+} heat-treated at 1000°C.

Solubility of rare earth elements in Zn_2TiO_4 nanocrystals

The presence of europium pyrochlore -$Eu_2Ti_2O_7$ in the samples opened the question about limits of the solubility of europium in Zn_2TiO_4 lattice. To answer this question, the initial sols were doped by different amounts of Eu^{3+} and thermally treated. The thermal evolution of the crystallite fraction of Zn_2TiO_4 for different Eu^{3+} concentrations can be seen from Figure 17. This figure shows that the crystallite fraction of undoped Zn_2TiO_4 is practically constant and close to 100% with respect to low concentrations of the residual ZnO. In the samples containing Eu ions the growth of zinc titanate is blocked and the relative amount of ZnO is not negligible at lower temperatures. Consequently, the crystallite fraction of such samples at low temperatures is rather lowered compared to the undoped sample. The crystallite fraction continuously grows up with increasing the temperature. This result holds only for the samples where the concentration of Eu^{3+} ions does not exceed the limits of solubility (i.e. of about 0.5 at. %). If the concentration of Eu^{3+} exceeds the limit of solubility (e.g. the concentration of 1 at. % Eu^{3+}), the break corresponding to the crystallization of new phase $Eu_2Ti_2O_7$ appears on the curve.

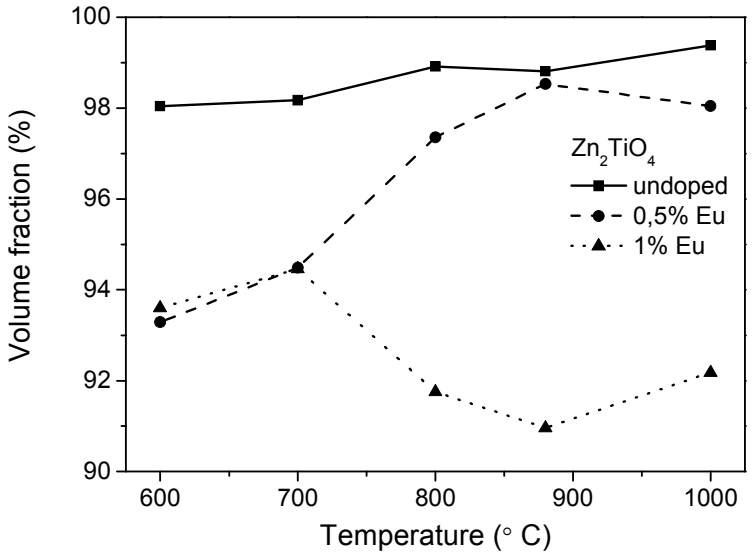

Figure 17 Thermal evolution of the crystallite fraction for undoped and Eu-doped Zn_2TiO_4

Similar processes were observed with erbium and thulium ions forming corresponding pyrochlores. To confirm the immobilization of REE elements in the matrix and their solubility, local microanalyses of individual grains were carried out with the results are summarized in Table 9.

Table 9 Results of the local chemical analysis of particular grains of Zn_2TiO_4 sintered at 1200 °C for 24 hours

Dopant	Zn	Ti	REE
	(at.%)	(at.%)	(at.%)
undoped Zn_2TiO_4	66,0±0,3	34,1±0,4	-
Eu	59,9±0,4	39,6±0,4	0,5±0,1
Tm	63,6±0,4	35,8±0,4	0,6±0,1
Er	64,0±0,4	35,6±0,4	0,4±0,1

The overall elementary analysis employing the EDS method determined contents of 66.5 and 33.5 at. % of zinc and titanium, respectively. However, the content of zinc in individual grains is slightly decreased particularly in samples containing rare earth elements. Such concentration differences and crystallization behavior can be explained on the basis of a hypothesis that REE particularly substitute zinc in the matrix and that concentrations higher

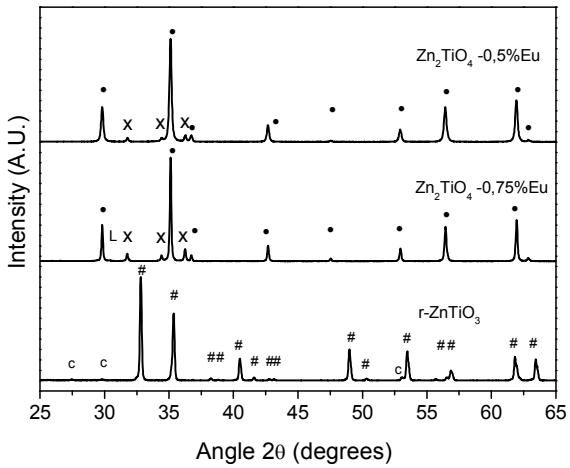

Figure 18 XRD patterns of REE doped Zn_2TiO_4 and r-$ZnTiO_3$ powder. Denoted symbols: (●) Zn_2TiO_4, (#) r-$ZnTiO_3$, (r) r-TiO_2, (c) c-$ZnTiO_3$, (L) $Eu_2Ti_2O_7$, (x)ZnO

that the limits of solubility of REE lead to the decomposition of doped zinc titanate into zinc oxide and corresponding REE pyrochlore. This hypothesis is further supported by results published elsewhere [64] where the introduction of vanadium, tin and chromium into the Zn_2TiO_4 lattice caused the substitution of Zn^{2+} in the lattice. In agreement with this mechanism and quantitative chemical analysis, zinc titanates doped by 0.5at.% of RE elements were prepared. Their diffractograms are shown in Figure 18. An increase of REE in concentrations to 0.75 at. % is followed by formation of REE pyrochlores as can be seen in the same figure.

Ratio Zn:Ti equal to 1:1, $ZnTiO_3$ nanocrystals growth

As presented in Introduction the system with the ratio Zn:Ti equal to 1:1 should provide us with two forms of $ZnTiO_3$ phases, i.e. with the cubic forms c- $ZnTiO_3$ crystallizing as the defect spinel structure and the rhombohedral phase r- $ZnTiO_3$ crystallizing as the ilmenite structure. For the undoped samples the crystallization starts by formation of c-$ZnTiO_3$ which is stable up to 800 °C as can be seen from Figure 19. Then the phase transformation takes place. The formed cubic defect spinel c- $ZnTiO_3$ is partially transformed into the rhombohedral form and partially into inverse spinel liberating r-TiO2. Above 900 °C the decomposition of rhombohedral $ZnTiO_3$ occurs. The presence of Eu^{3+} ions in the input xerogels does not only block the crystallization process but significantly stabilizes the cubic structure extending it's persistence up to 900 °C. As one can see from Figure 20a, the average grain size doesn't exceed 40 nm. The corresponding SEM image demonstrated in Figure 20 shows that the sintered powders are formed by homogenous uniform crystallites with fine structure.

Rather complicated is the preparation of pure rhombohedral $ZnTiO_3$. It can be successfully formed only in a narrow temperature interval above 800 °C. A relatively small

increasing of the temperature leads to the formation of undesirable inverse spinel Zn_2TiO_4. It has been successfully prepared by heat-treating the undoped xerogels at 780 °C for 48 hours. The recorded XRD patterns of the prepared samples are shown in Figure 18.

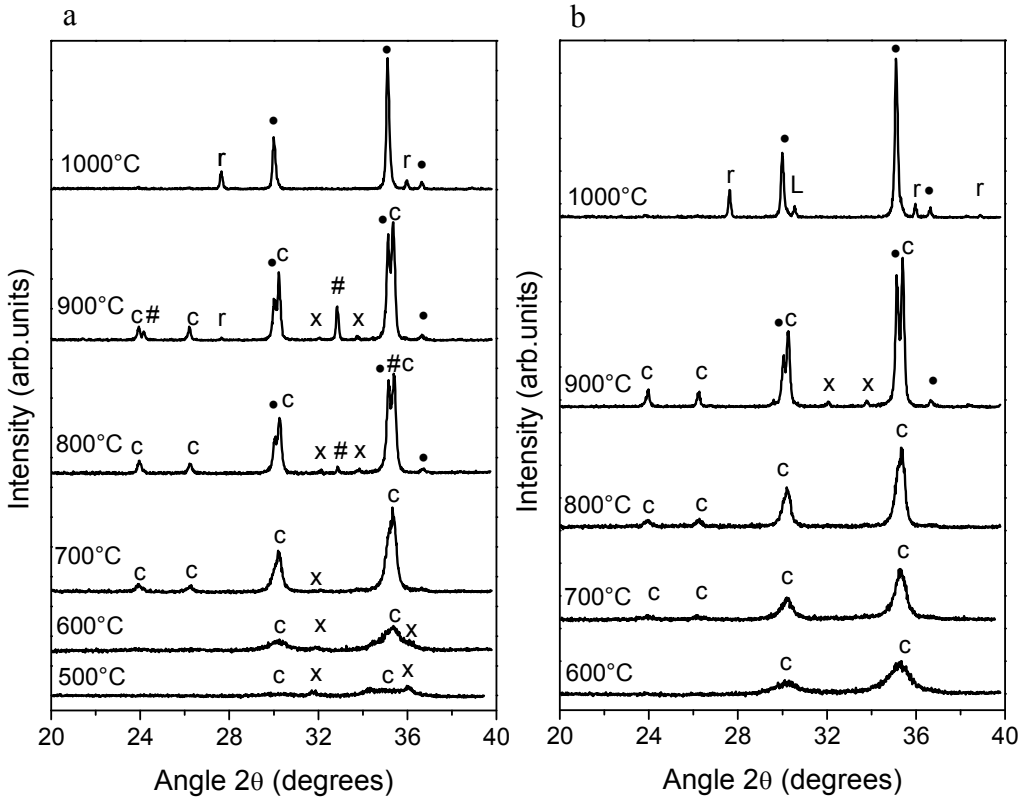

Figure 19 XRD patterns depicting the nanocrystals evolution of xerogels prepared by the direct heteronucleation for the ratio Zn:Ti=1:1. a) undoped xerogels, b) xerogels doped by 1 at.% of Eu ions. Denoted symbols: (c) c-$ZnTiO_3$, (x) ZnO, (#) r-$ZnTiO_3$, (r) r-TiO_2, (●) Zn_2TiO_4, (L) $Eu_2Ti_2O_7$.

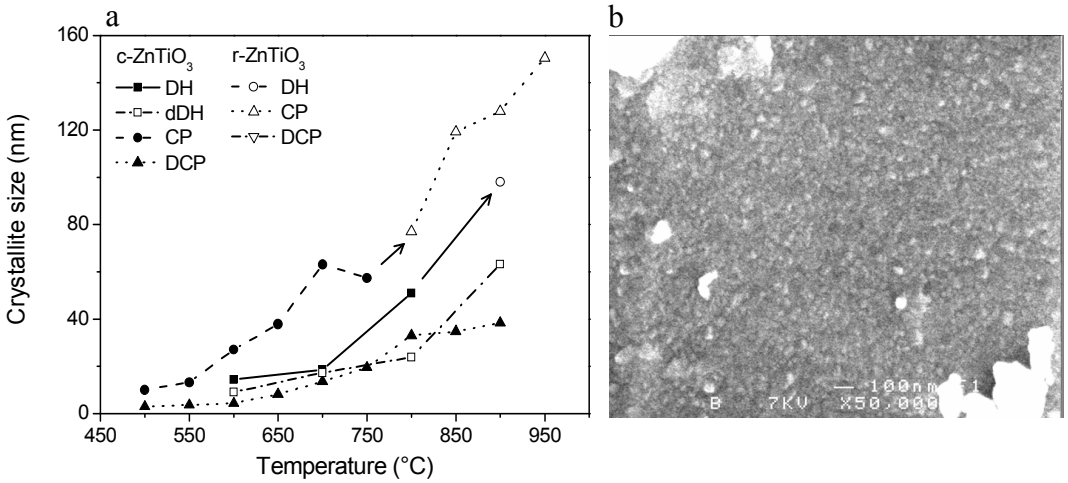

Figure 20 a) Temperature dependence of $ZnTiO_3$ nanocrystals size on the sintering temperature for particular approaches Sizes calculated by the Debye-Scherrer's equation. b) c-ZnTiO3 doped by 1 at.% of Eu^{3+} heat-treated at 800°

Ratio Zn:Ti equal to 2:3

On the basis of a literature review, the formation of defect spinel $Zn_2Ti_3O_8$ was expected. As one can see from Figure 21 the crystallization of undoped samples starts below

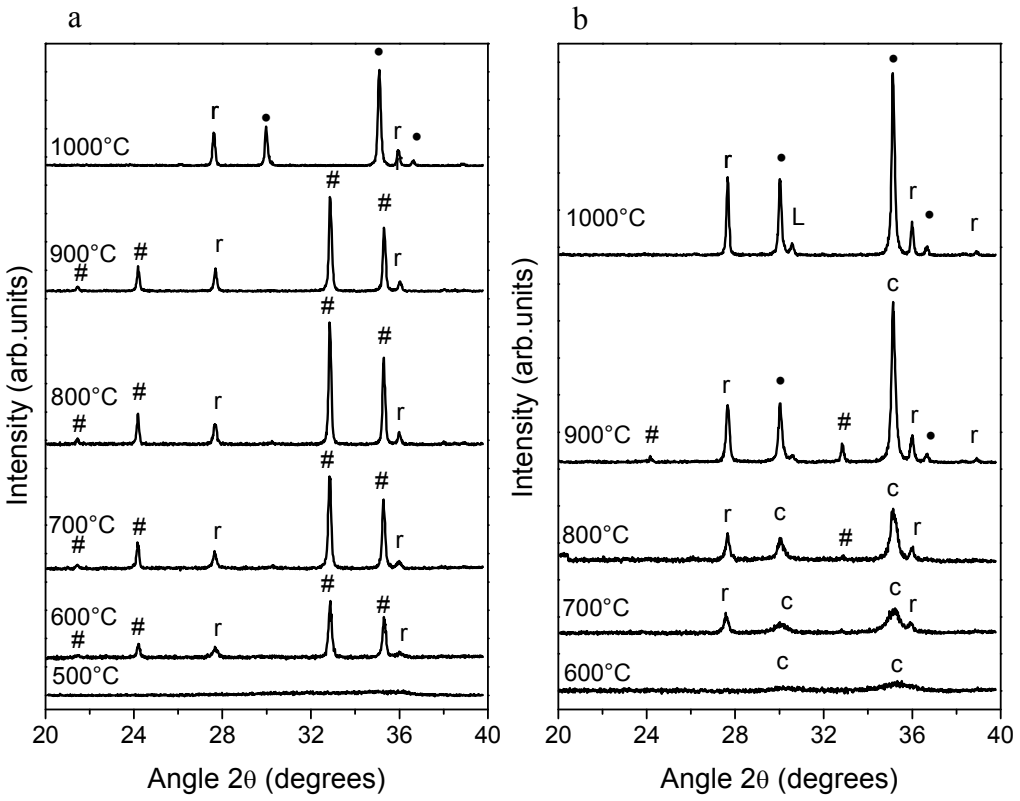

Figure 21 XRD patterns depicting the nanocrystals evolution of xerogels prepared by the direct heteronucleation for the ratio Zn:Ti=2:3. a) undoped xerogels, b) xerogels doped by 1 at.% of Eu ions. Denoted symbols: (#) r-$ZnTiO_3$, (r) r-TiO_2, (•) Zn_2TiO_4, (c) c-$ZnTiO_3$, (L) $Eu_2Ti_2O_7$.

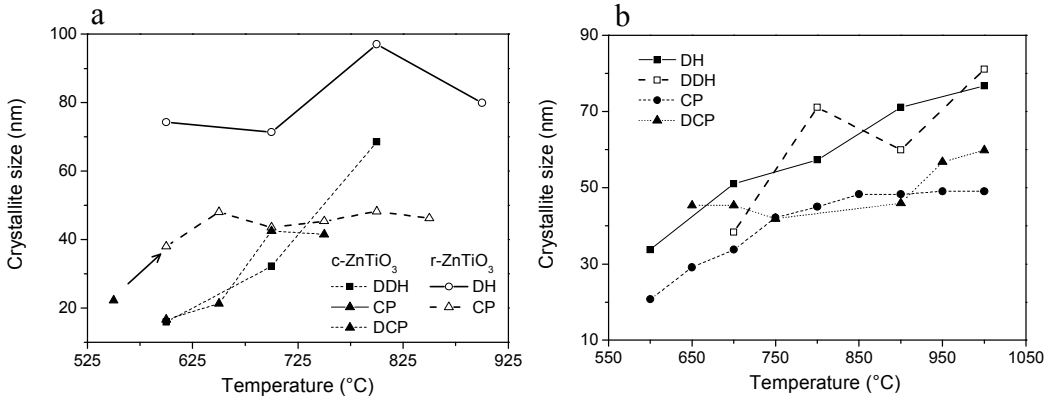

Figure 22 Temperature dependence of nanocrystals size on the sintering temperature for formed structures and particular sol-gel approaches. Sizes calculated by the Debye-Scherrer's equation. a) $ZnTiO_3$, b) r-TiO_2.

600 °C by the formation of r-TiO_2 and rhombohedral structure of $ZnTiO_3$. By raising the temperature, the quantity of r-$ZnTiO_3$ and r-TiO_2 progressively increases as can be deduced from the integrated intensity of the XRD peaks. The size of r-TiO_2 nanocrystals is almost doubled from 40 to 80 nm at 900 °C. However, the size of r-$ZnTiO_3$ nanocrystals remains practically constant in the whole temperature range as can be seen from Figure 22. It is evident that r-$ZnTiO_3$ remains stable to temperatures above 900 °C when it is decomposed to inverse spinel Zn_2TiO_4 and r-TiO_2. The sintered powder, demonstrated in Figure 23, containing r-$ZnTiO_3$ with r-TiO_2 is composed of relatively large grains. Some of them are slightly elongated or form fibrous aggregates composed of primary 60 or 80 nm nanocrystals. Such a tendency is characteristic for rutile and ilmenite expansions in the space [45]. In analogy with the previous results achieved for the ratio Zn:Ti equal to 1:1, the presence of Eu^{3+} ions leads to the formation of c-$ZnTiO_3$ which is transformed to r-$ZnTiO_3$ and r-TiO_2.

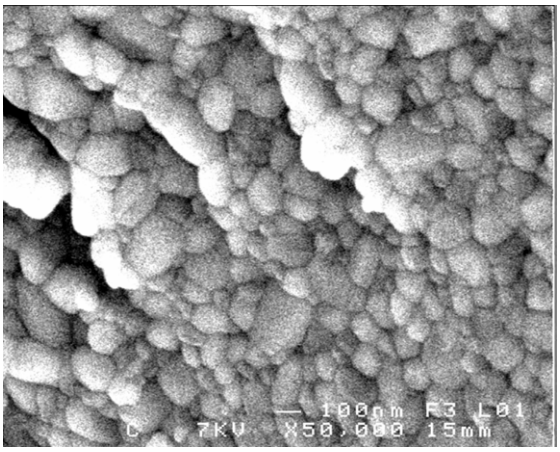

Figure 23 c-$ZnTiO_3$/r-TiO_2 heat-treated at 800°C.

Despite the expectation, none of the selected approaches provides the defect spinel $Zn_2Ti_3O_8$. The results of this thesis give a strong support to the published hypothesis that the referred structure cannot be prepared by wet chemical approaches [49].

Optical properties of sintered bulk xerogels

Optical properties of the prepared ternary nanocrystals could provide us with important information about electronic transitions in these materials and especially with the information about energy of the bandgap. Moreover, one can obtain important information about the REE displacements inside the formed lattices from Stark splitting of the hypersensitive electronic transition $^5D_0 \rightarrow {}^7F_j$ belonging to Eu^{3+} ions. Bulk xerogels doped by 1at. % of Eu^{3+}sintered at 800 °C were analyzed.

As can be seen from Figure 24a, absorption edges of all prepared structures range from 300 to 420 nm. The highest bandgap of 3.8 eV was observed at the prepared c-$ZnTiO_3$ ternary structure. More complicated situation raises in cases of the other compounds. Even in the case of undoped Zn_2TiO_4 the sample contains traces of side formed ZnO and consequently the absorption edge of pure Zn_2TiO_4 observed below 325 nm is superposed by the absorption edge of ZnO which raises a shoulder at 365 nm. The corresponding bandgaps for Zn_2TiO_4 and ZnO are 3.6 and 3.25 eV, respectively. The compound of a general ratio of Zn:Ti equal to 2:3 has the absorption edge at 410 nm with the corresponding value of bandgap of 3.02 eV. Such

a result is in a good coincidence with the value for r-TiO_2. However, the absorption edge of r-$ZnTiO_3$ is completely overlapped.

Excitation photoluminescence spectra recorded for the emission at 612 nm are demonstrated in Figure 24b. The normalized intensities of electronic transitions at 464 and 530 nm are practically invariant. The intensity of electronic transitions around 394 nm is

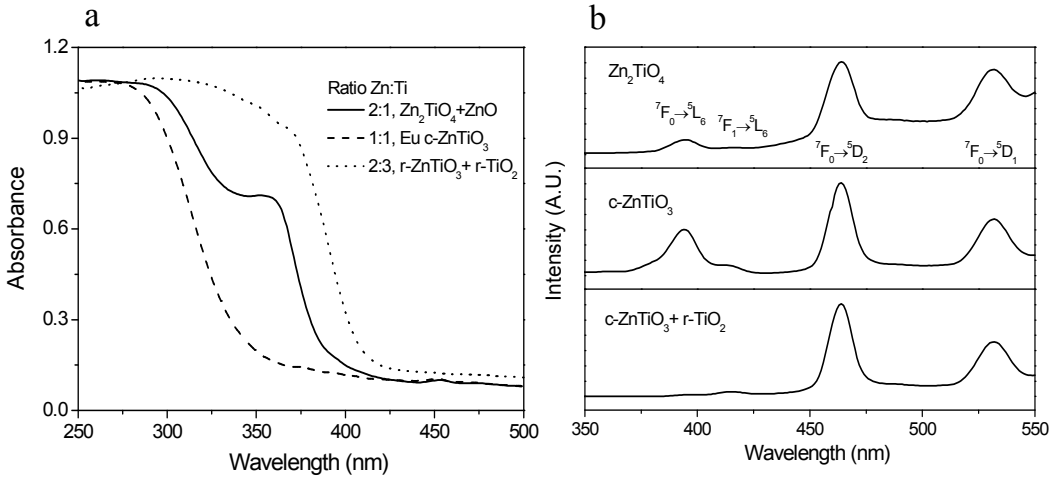

Figure 24 Optical spectra of prepared xerogels sintered at 800°C. a) Kubelka-Munk corrected diffuse reflectance spectra, b) fluorescence excitation spectra of samples doped by 1 at. % of Eu^{3+} recorded at the emission wavelength 612 nm

significantly decreased according to the shift of absorption edges of particular samples. A part of the absorbed energy is consumed in non-radiative transitions inside semiconductor structure of occurring oxides and doesn't contribute to the luminescence of Eu^{3+} ions. All samples show characteristic emission spectra with electronic transitions characteristic for Eu^{3+} ions as can be seen from Figure 25a. The intensity of the emission spectra excited at 394

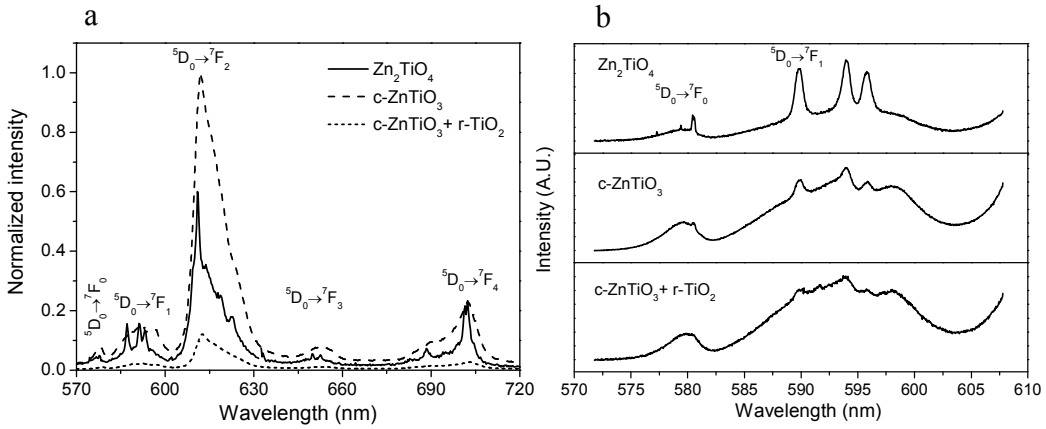

Figure 25 Room temperature luminescence spectra of prepared xerogels doped by 1 at.% of Eu^{3+}sintered at 800°C recorded for the excitation wavelength 394 nm. a) Normalized emission of the global $^5D_0 \rightarrow {}^7F_J$ transition, b) zoom on the position of J=0 and J=1 transitions.

nm dramatically falls down for Zn_2TiO_4 phase and for compound r-$ZnTiO_3$/ r-TiO_2 comparing to cubic $ZnTiO_3$. To suppress the charge transfer from TiO_2 and ZnO lattices to Eu^{3+} ions, the

samples were excited at 464 nm, i.e. beyond the band gap transitions of the mentioned semiconductor oxides. Although the difference in the photoluminescence intensity is not so profound, the red luminescence in cubic $ZnTiO_3$ remains the most intensive comparing to the other phases. The summary of the results of photoluminescence analysis are displayed in Table 10. It should be noted that any photoluminescence transitions indicating the presence of Eu^{2+} ions has not been found in global luminescence spectra.

Table 10 Relative intensities of radiative $^5D_0 \rightarrow {}^7F_J$ (J=1,2) transitions and asymmetry factors R(J2/J1) for $Zn_xTi_yO_z$ structures doped by 1 at. % of Eu^{3+} prepared by the cluster process and sintered at 800 °C.

Ratio Zn:Ti		2:1	1:1	2:3
Detected phases		Zn_2TiO_4 c-$ZnTiO_3$ trace ZnO trace	c-$ZnTiO_3$	c-$ZnTiO_3$/r-TiO_2 h-$ZnTiO_3$ trace
Average crystallite size (nm)		25	30	20
I (612nm)	λ_{ex} = 394 nm	0.89	1	0.02
	λ_{ex} = 464 nm	0.53	1	0.33
R (J2:J1)	λ_{ex} = 394 nm	2.7	3.1	3.44
	λ_{ex} = 464 nm	4.1	4.9	4.3

Recorded luminescence spectra of all samples show broad emission bands including the symmetrically forbidden $^7F_0$ transition. The bulk spectra are superposed by sharp narrow peaks in particular cases. Such an observation implies a hypothesis that Eu^{3+} ions are mainly placed in low symmetry sites, and narrow peaks should be related to the positions with a high coordination symmetry of Eu^{3+} polyhedrons. The phenomena is most obvious for Zn_2TiO_4 lattice where the $^7F_0$ transition is superposed by two weak but sharp single transitions at 577 and 579 nm and one doublet at 581 nm indicating the presence of at least two discrete lattice sites as can be seen in Figure 25b. The modulation of emission peaks of c-$ZnTiO_3$ is less conspicuous reflecting the decrease of the local symmetry of Eu^{3+} ions inside the matrix. The asymmetry factors R(J2/J1) calculated as the ratio of integrated intensities of $^5D_0 \rightarrow {}^7F_2$ over $^5D_0 \rightarrow {}^7F_1$ transitions appear a lowest value, corresponding to the highest crystal field symmetry of Eu^{3+} ions, for inverse spinel lattice of Zn_2TiO_4.

From the general point of view, Eu^{3+} ions can be located in a) a regular crystalline lattice of formed ternary phases, b) on the boundary of formed nanocrystals or c) in other side-formed phases or clusters. Since the solubility of Eu^{3+} ions inside the Zn_2TiO_4 lattice was established below 0.5 at. % the sample is approximately two times over doped. Consequently, Eu^{3+} ions should be partially distributed into side formed $Eu_2Ti_2O_7$ or at the boundary of nanocrystals. The referred solubility of Eu^{3+} ions inside c-$ZnTiO_3$ was estimated to be of 5 at. % [58] and the solubility in tetragonal rutile was estimated to be of 0.3 at. % [74]. As mentioned in Introduction, inverse spinel Zn_2TiO_4 can be expressed by the formula $(Zn_8)^t(Zn_8Ti_8)^oO_{32}$, and introduced Eu^{3+} ions partially substitute zinc ions in the inverse spinel lattice as was demonstrated in previous parts. Cubic $ZnTiO_3$ can be regarded as defect spinel $(Zn_8)^t(Zn_{8/3}\square_{8/3}Ti_{32/3})^oO_{32}$ possessing free octahedral cavities which can be occupied by introduced Eu^{3+} ions. In the concentration around 1 at. % all Eu^{3+} ions should be fully incorporated into the lattice. One can deduce that Eu^{3+} ions are particularly distributed inside the octahedral cavities. Since the occupation of individual atomic positions in the unit cell is less regular in cubic $ZnTiO_3$, the local symmetry of Eu^{3+} ions is reduced. The presence of r-TiO_2 nanocrystals further increases the scale of accessible positions on the rutile boundary, raising up the disorder of the crystal field of the incorporated Eu^{3+} ions. Such conclusions are

in good coincidence with the calculated values of the asymmetry factor R(J2/J1) in Table 10. However, the full explanations of dislocations of europium ions inside the investigated lattices requires further analysis based on advanced low-temperature spectroscopy combined with advance physical methods such a X-ray photoelectron spectroscopy.

Crystallization properties of prepared materials

Measured XRD results provide us with important information about global structural evolution in the studied ternary system. On the basis of these results and those of the DTA analysis one can estimate the thermal stability of particular phases and evaluate new phase diagram for the studied structures. The special attention was paid to the inverse spinel structure Zn_2TiO_4 for its high thermal stability and potential application in fiber-optic technology.

Results of selected DTA analysis of bulk xerogels pre-treated at 400 °C are displayed in Figure 26. For the ratio Zn:Ti equal to 2:1 the crystallization occurs at

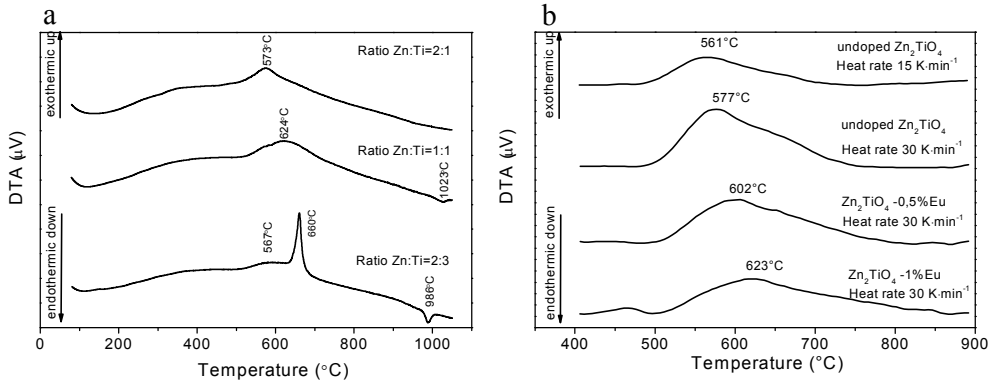

Figure 26 DTA analysis of powders pre-treated at 400°C. a) DTA analysis for different Zn:Ti ratio. Heating rate 10 K·min^{-1}. O_2 flow 50 cm^3·min^{-1}. b) DTA analysis of Zn_2TiO_4 structure demonstrating effects of the REE dopation and heating rate to the crystallization peak of Zn_2TiO_4.

573 °C (see Figure 26a). The introduction of REE into the xerogels shifts the crystallization peaks to higher temperatures, and so does, naturally, the increasing heat rate as is clearly demonstrated in Figure 26b. For the system with the ratio of Zn:Ti equal to 1:1 the crystallization peak appears at 624 °C. Unfortunately, technical parameters of the used apparatus have not allowed us to correctly evaluate the phase transformation from the cubic to the rhombohedral structure. The peak at 1023 °C should be attributed to the decomposition of $ZnTiO_3$ into r-TiO_2 and Zn_2TiO_4. The crystallization peaks for powder with the ratio Zn:Ti equal to 2:3 appears at 567 °C and it is followed by the sharp crystallization peak of r-TiO_2 at 660 °C. The formed $ZnTiO_3$ is decomposed at 986 °C. The correct positions for particular peaks were evaluated from the dependence of peaks temperature versus the heat rate extrapolated to zero value of the heat rate. Calculated data are summarized in Table 11. As was predicted from the results of XRD analysis, the presence of REE shifts the crystallization to higher temperatures. The crystallization of all pure ternary phases occurs bellow 600 °C, except that of pure r-$ZnTiO_3$ which could be prepared by phase transformation of the cubic form at 800 °C.

The crystallization energy of the prepared nanocrystals was evaluated from the Kissinger, Augis-Bennett and Ozawa's equations. Values of the activation energy were calculated from the slope of the linear fits for particular equations as can be seen in Figure 27.

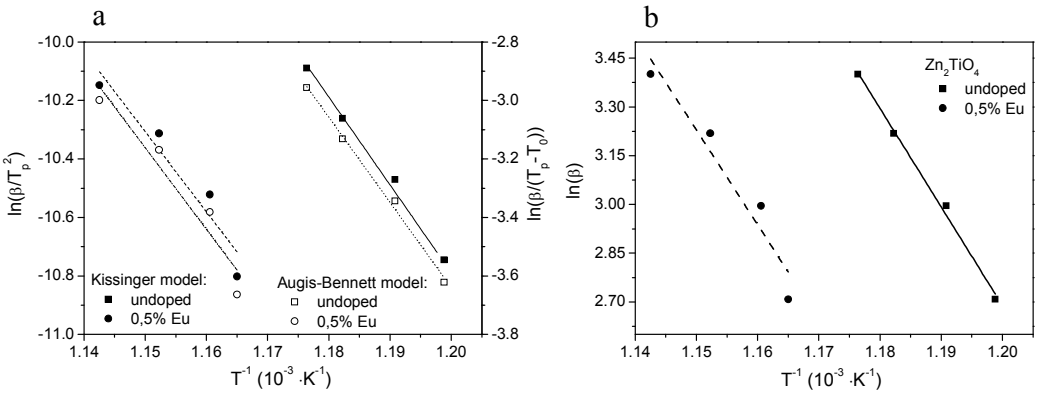

Figure 27 Determination of crystallization energy. Experimental data and corresponding fits for the undoped and 0.5 at. % Eu^{3+} doped Zn_2TiO_4. a) Plots of Kissinger (left scale) and Augis–Bennett (right scale) approximations, b) Ozawa's approximation

The results are summarized in Table 11. All three approximations provide us with similar results for particular samples. Except Zn_2TiO_4 the introducing of Eu^{3+} ions increases the activation energy of crystallization.

Table 11 Crystallization temperatures and activation energy of crystallization calculated for particular samples using different approximations

Ratio Zn:Ti Dopant Detected phase	Crystallization temperature (°C)	Kissinger approximation (kJ·mol^{-1})	Augis-Bennett approximation (kJ·mol^{-1})	Ozawa approximation (kJ·mol^{-1})
2:1 Zn_2TiO_4	546±2	250±19	242±12	252±12
2:1 0,5 at.% Eu Zn_2TiO_4	568±3	228±46	232±46	242±21
2:1 0,5 at.% Tm Zn_2TiO_4	585±2	212±47	216±47	227±47
2:1 0,5 at.% Er Zn_2TiO_4	578±4	191±25	195±25	205±25
1:1 c-$ZnTiO_3$	582±2	207±3	215±24	221±24
1:1 1 at.%Eu c-$ZnTiO_3$	584±3	376±45	339±73	390±45
2:3 h-$ZnTiO_3$	520±2	109±13	120±13	124±14
2:3 1 at.%Eu c-$ZnTiO_3$	553±4	218±17	210±26	232±16

From the course of DTA curves, one can estimate the reaction mechanism of the formation of Zn_2TiO_4 inverse spinel structures. The analysis was carried out for the pure ternary phase and for the sample containing 0.5 at. % Eu^{3+} ions and the results are extended to the other investigated rare earth elements. The calculated Avrami parameter n_A (Equation 11)

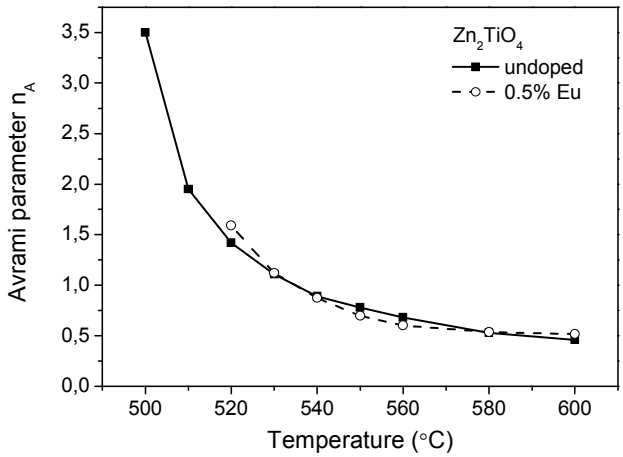

Figure 28 Avrami parameters for pure and undoped Zn_2TiO_4

is displayed in Figure 28. Results show that in the case of Zn_2TiO_4 large values of n_A parameter rapidly decrease with the increased heat-treatment temperature to values calculated for the REE- doped samples. The high values of n_A at the beginning of the crystallization of Zn_2TiO_4 are typical for the homogeneous nucleation with the three-dimensional growth at the constant nucleation rate [79]. Once uniform nanocrystals are formed filling the volume of the initial material, the crystallization mechanism is changed and the cellular recrystallization takes place. As a result nanocrystals regularly grow together as one can see from the Figure 16c and Figure 16d; this growth is limited by diffusion through the crystal boundary and n_A parameters are accordingly decreased.

Despite the lower crystallization energies calculated for REE-doped samples, their crystallization is shifted to higher heat-treatment temperatures. The calculated values of the Avrami parameters are typical for the site saturated nucleation followed by the three dimensional grow controlled by the diffusion which rapidly pass into the cellular recrystallization [79]. Such phenomena can be explained by the incorporation of REE ions into the pre-formed Zn_2TiO_4 clusters. As shown above, REE ions particularly substitute zinc ions inside the zinc titanate structure forming nucleation centers for generated zinc titanate and blocking the crystallite grow till they are fully incorporated into the crystalline lattice. Once REE elements are integrated inside the crystalline lattice the crystallization is facilitated that is characterized by the calculated activation energies of crystallization. Thus, the formation of smaller uniform crystallites is more favorable in the case of doped zinc titanates. On the other hand, the crystallite growth is more favorable in the case of undoped zinc titanate. These effects are explicitly remarkable for the samples heat-treated to 1000 °C in which Zn_2TiO_4 grown up nearly to micrometric grains and Eu doped zinc titanate still remained in the form of nanocrystalline powder as one can clearly see in the SEM pictures Figure 16c and Figure 16d.

Summary

Two sol-gel approaches based on the reaction of $[Zn_4O](Acetate)_6$ clusters with titanium(IV)i-propoxide and on the direct heteronucleation of zinc acetate dihydrate with titanium(IV)butoxide were employed to prepare stable heterosols. The concentration ratios of Zn:Ti in initial sols were 2:1, 1:1 and 2:3. The prepared heterosols were alternatively doped by 1 at. % of Eu^{3+} ions and evaporated at ambient temperature under vacuum atmosphere to bulk xerogels.

The prepared input sols were analyzed by the UV-VIS spectroscopy. The prepared bulk xerogels were analyzed by the differencial thermal analysis coupled with the mass spectrometry, FT-IR spectroscopy, X-ray diffraction analysis, photoluminescence spectroscopy and scanning electron microscopy. The chemical compositions of the prepared xerogels were verified by energy-dispersive X-ray spectroscopy.

It was found that acetate presented in the samples are primary coordinated to titanium ions as bidentate organic ligands and the increasing amount of titanium inside the input sols shifts the burn-out temperature of organic ligands to higher temperatures.

The xerogels were subsequently thermally annealed up to 1000 °C and the structural evolution of formed phases was followed by the XRD analysis. For the ratio of Zn:Ti equal to 2:1 the formation of inverse spinel Zn_2TiO_4 was observed. The sol composition with the ratio Zn:Ti equal to 1:1 gives cubic defect spinel $ZnTiO_3$ which is partially transformed to rhombohedral $ZnTiO_3$. Finally, both $ZnTiO_3$ structures undergo the thermal dissociation to inverse spinel Zn_2TiO_4 and rutile r-TiO_2 at 990 °C. Despite to the referred literature the composition with the ratio of Zn:Ti equal to 2:3 has not provided us with the expected cubic defect spinel of the general formula $Zn_2Ti_3O_8$. The formed compound contained rhombohedral $ZnTiO_3$ and rutile r-TiO_2 in the case of undoped samples and the compounds of cubic $ZnTiO_3$ and rutile r-TiO_2 in the case that Eu^{3+}ions were introduced into the input sol. Both mentioned compounds undergo the thermal dissociation to inverse spinel Zn_2TiO_4 and rutile r-TiO_2 above 900 °C.

Sizes of formed phases were calculated on the base of the Debye-Scherrer's equation and verified by SEM observations. Crystallization temperatures of all formed ternary phases are below 600 °C. The proper initial composition of the input sol and thermal annealing allow us to obtain the selected phase with tailored nanocrystal size ranging from tens of nanometers up to micrometric scale.

The direct heteronucleation approach leads to bigger nanocrystals comparing to the cluster process and allows the formation of pure phases. The cluster process leads to smaller nanocrystals, however the prepared samples contain indispensable amounts of side-formed phases. The explanation can be found in the formation of polymeric clusters from $Ti_xO_y(OH)_z$ species in initial sols. Hence, the cluster process partially displays the character of the solid state reaction.

The introducing of Eu^{3+} ions into input sols significantly changes the crystallization process initiating the formation of cubic spinel structures and blocks the cubic-rhombohedral transformation. Consequently, the crystallization temperatures are increased, nanocrystals growth is suppressed and annealed xerogels appear more homogenous and with uniform shapes comparing to the undoped samples.

The strong red fluorescence and significant Stark splitting of ^7F_J peaks in emission spectra of Eu^{3+} ions confirm the successful incorporation of Eu^{3+}ions into the cubic spinel lattices. The comparison of photoluminescence intensities and asymmetric factors support the hypothesis that cubic $ZnTiO_3$ crystallizes in the defect spinel lattice. The presence of Eu^{3+} ions in concentrations above the solubility limits in the formed compounds leads to the formation of cubic pyrochlore structure $Eu_2Ti_2O_7$.

The solubility of Eu^{3+}, Er^{3+} and Tm^{3+} inside the prepared inverse spinel Zn_2TiO_4 was experimentally determined to be of about 0.5 at. %. The nucleation process of pure Zn_2TiO_4 has the character of homogenous nucleation followed by the three dimensional growth at a constant nucleation rate which finally pass into the cellular recrystallization controlled by the diffusion of matter. The crystallization process of Zn_2TiO_4 doped by Eu^{3+} ions has the character of the site saturated nucleation followed by the three dimensional grow and cellular recrystallization

From the results of XRD analysis combined with the DTA analysis the following phase diagram shown in Figure 29 was proposed for particular samples prepared by the direct heteronucleation.

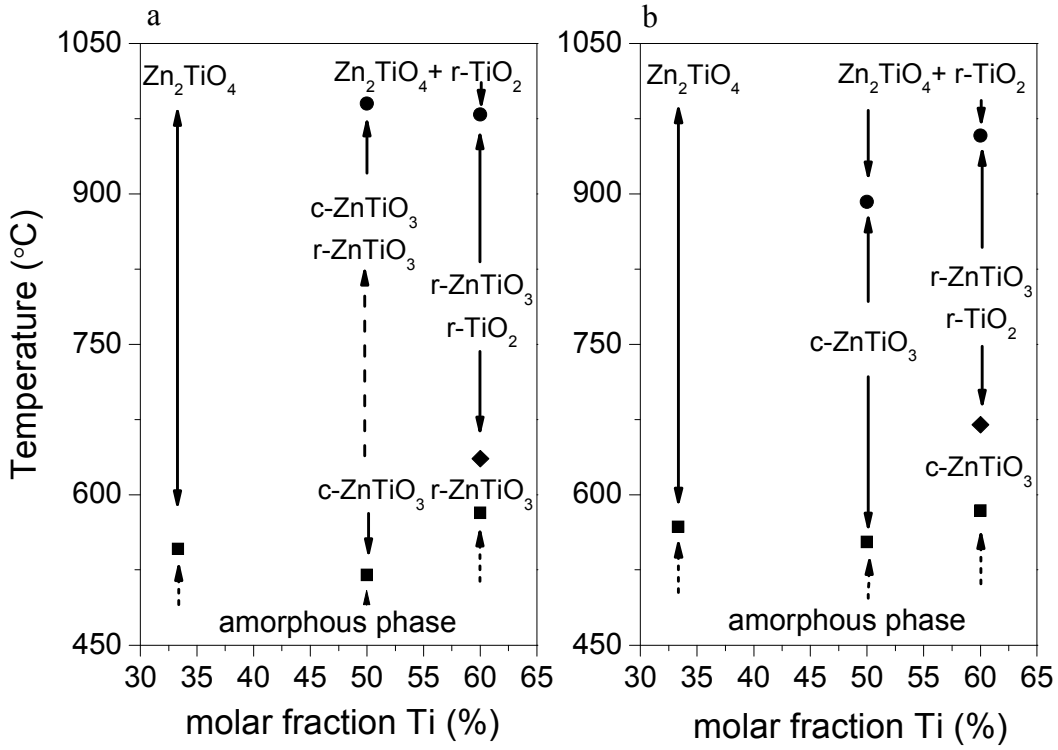

Figure 29 Proposed phase diagram for $Zn_xTi_yO_z$ structures prepared by the "bottom-up" sol-gel route. a) undoped samples for the selected ratios of Zn:Ti = 2:1, 1:1, 2:3. b) Samples doped by 1 at. % of Eu^{3+} ions for selected ratios of Zn:Ti = 2:1, 1:1, 2:3. Side formed $Eu_2Ti_2O_7$ is not shown.

Preparation and characterization of thin films

Prepared ternary nanocrystalline materials provide us by several interesting properties that could be fruitfully exploited in the field of optic, opto-electronic and photocatalysis. Several possible applications have been illustrated in Introduction. However, most of applications prefers or implicitly requires materials in the form of thin films rather than powders. In the following chapter the preparation and characterization of nanocrystalline ternary phases will be presented showing conditions necessary for the preparation of nanocrystalline ternary phases in optical quality and for achieving corresponding optical properties of thin films contained these phases.

As found by the DSC analysis, thermodynamic properties of thin films do not significantly differ from those of the bulk xerogels. Since the materials prepared by the direct heteronucleation process appear better properties and lead to pure stable ternary phases, input sols prepared by the direct heteronucleation process were mainly employed in the deposition of thin films. Although the selected approach allows us to prepare thin films with any ratio of Zn:Ti, only results achieved with input sols characterized by the ratio of Zn:Ti equal to 2:1, 1:1, 2:3 and 1:9 which should provide us with inverse spinel Zn_2TiO_4, cubic defect spinel $ZnTiO_3$ and the compound of rhombohedral $ZnTiO_3$ with rutile (r-TiO_2) are discussed. The sol with the ratio 1:1 was modified by introducing 1 at. % of Eu^{3+} ions to stabilize the cubic structure of $ZnTiO_3$ and to prevent side crystallization.

The crystallization of the first two compounds mentioned above occurs at 546 °C and 584 °C, respectively. The crystallization of r-$ZnTiO_3$ starts at 520 °C, however, it is accompanied by the side formed r-TiO_2 which should crystallize at 636 °C. Since the transmission optical spectra of the prepared films were recorded on samples applied on the Pyrex glass substrate, the annealing temperature should not dramatically exceed 650 °C to prevent the deformation of the substrate. The thickness of the prepared films on the Pyrex substrate could be varied from hundreds of nanometers up to few micrometers and depends on the viscosity and concentration of the input sols and on withdrawing speed.

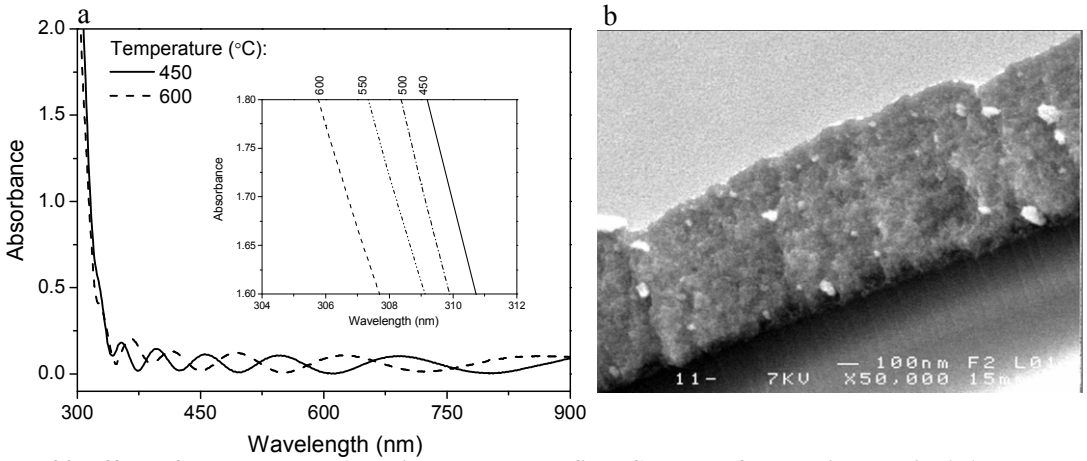

Figure 30 Effect of the thermal annealing to deposed film. Sample of the ratio Zn:Ti =1:1 doped by 1 at. % Eu^{3+}. a) Absorption spectra of prepared film. In the inset is the zoomed area with the absorption edge. b) SEM image of the cross-section of prepared film annealed at 650 °C.

As introduced in Experimental part, thin films were prepared by multideposition of input heterosols with subsequential annealing at 350 °C in air atmosphere in order to burn out

remaining organic material, namely acetate ligands, and to densify the formed films. The deposition process can be easily followed by recording transmission spectra of the formed films. With increasing number of the layers a number of interference fringes in absorption spectra increases and absorption edge is shifted to higher wavelengths. These effects can be seen from Figure 30a showing optical absorption spectra of c-$ZnTiO_3$ as a function of annealing temperature. With increasing the temperature the densification of thin films occurs appearing two important phenomena in the optical transmission spectra. The interference fringes are shifted according to the variation of film thickness and refractive index changes. The absorption edge is shifted with the variation of film thickness going closely to the value corresponding to the fully densified film. In consequent annealing the shift of the absorption edge is practically a linear function of the annealing temperature as can be seen from the inset in Figure 30a. Once the crystallization takes place, a new crystalline phase with different optical properties from the initial amorphous material is formed which causes the corresponding shift of the optical edge.

The prepared films were investigated by SEM microscopy allowing to verify the film thickness and crystalline structure as can be seen from Figure 30b. The presence of the formed ternary phases was confirmed by the XRD analysis demonstrated in Figure 31. Calculated crystallite sizes are displayed in Table 12.

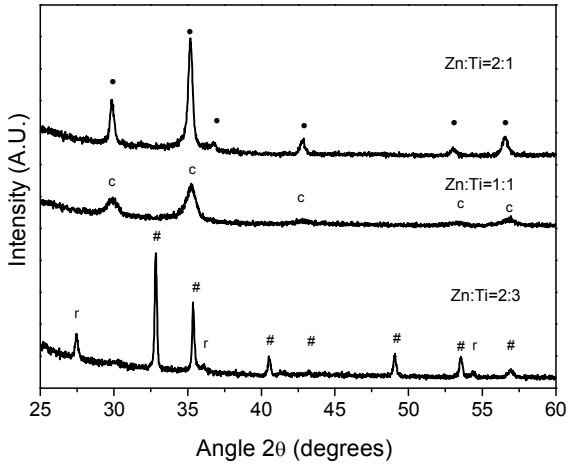

Figure 31 XRD patterns of thin films prepared for different ratio Zn:Ti annealed at 650°C. Denoted symbols: (●) Zn_2TiO_4, (#) r-$ZnTiO_3$, (r) r-TiO_2, (c) c-$ZnTiO_3$.

Table 12 AFM analysis of annealed thin films with corresponding nanocrystalline structure and average crystallite size calculated by the Debye-Scherrer's equation

	Synthesis	Temperature (°C)	Ratio Zn:Ti		
			2:1	1:1,Eu	2:3
RMS factor	Cluster process	550	0.520	0.669	1.10
		650	1.12	0.807	1.32
	Direct heteronucleation	650	0.636	0.418	0.87
Detected phases		650	Zn_2TiO_4	c-$ZnTiO_3$	r-$ZnTiO_3$ r-TiO_2
Average crystallite size (nm)		650	20	9	46 (r-$ZnTiO_3$) 36 (r-TiO_2)

According to the increasing difference between the annealing temperature and the crystallization temperature of particular phases displayed in Table 11 c-$ZnTiO_3$ crystallizing at 584 °C gives the smallest nanocrystals with the average size around 9 nm. However, the compound of r-$ZnTiO_3$/r-TiO_2 forms bigger crystals with the size around 46 nm according to the observed crystallization temperature at 520 °C. Such an observation could be made from the surface morphology of the prepared films. AFM scans of the prepared layers are displayed in Figure 32. All prepared samples appear relatively regular and homogenous morphology

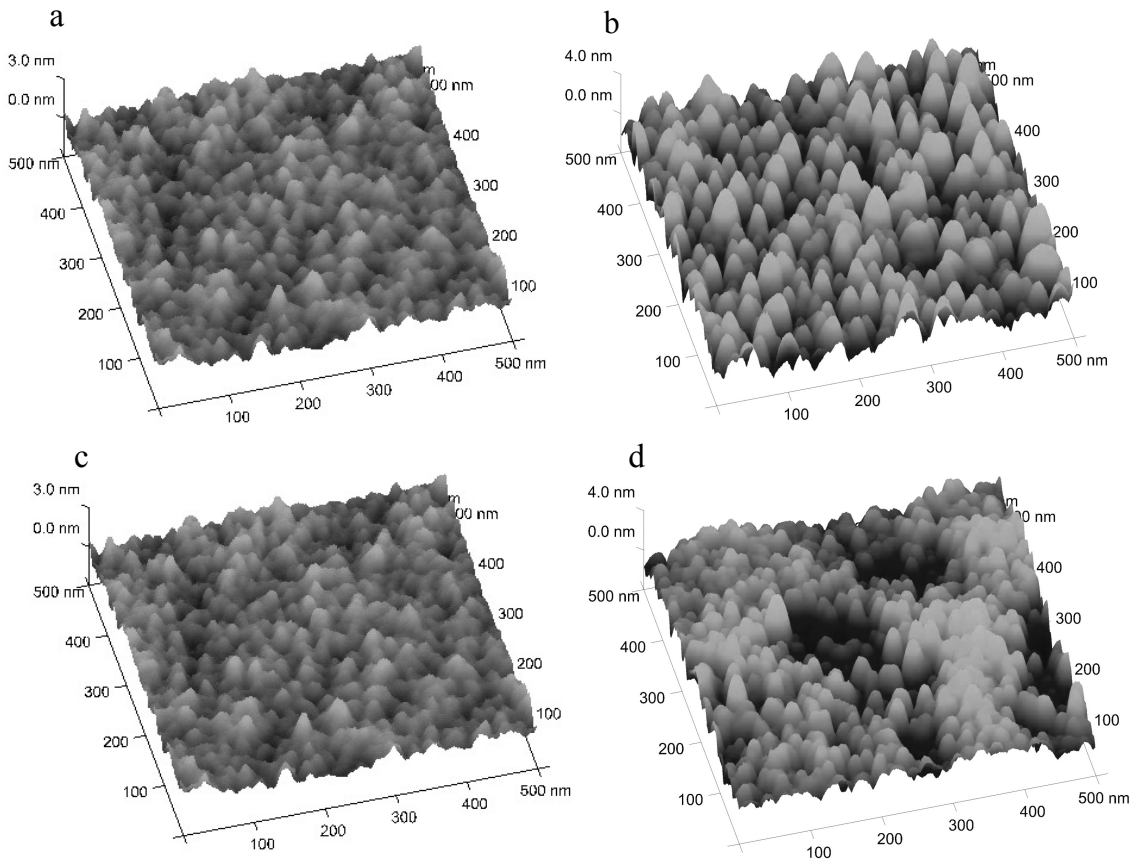

Figure 32 Surface morphology of films annealed at 650°C. a) Ratio Zn:Ti=2:1 prepared by DH, b) Ratio Zn:Ti=2:1 prepared by CP, c) Ratio Zn:Ti=1:1 doped by 1 at. % Eu^{3+}, d) Ratio Zn:Ti=2:3.

with surface variations below 10 nm. Surfaces of the films containing formed Zn_2TiO_4 and c-$ZnTiO_3$ demonstrated in Figure 32a, c consist of regularly associated mostly spherical crystallites with the lateral dimension around 20 and 10 nm, respectively. The surface of the film formed by the compound of r-$ZnTiO_3$/r-TiO_2 (see Figure 32d) appears highly irregular structure of the surface that should be attributed to the coexistence of two different types of nanocrystals. The nanocrystal size can be partially correlated with the variation of the surface represented by the RMS factor indicated in Table 12. Smaller nanocrystals lead to smaller variations of the surface and lower value of the RMS factor. However, the general application of this statement should be carefully considered. According to our previous conclusions and to the results depicted in Figure 15, thin films applied from sols which were prepared by the cluster process are composed of nanocrystals with the size comparable with that one produced by the direct heteronucleation. With increasing the temperature the RMS factor for particular samples is increased according to the beginning crystallization. However, despite of the

comparable size of the formed nanocrystals, the RMS factor of the films deposed from input sols prepared by the cluster process (see Figure 32b) is almost doubled in comparison with that of the films prepared from the directly heteronucleated sols. The surface of these films is formed by almost oriented elongated nanocrystals. This observation confirms the previous hypothesis that xerogels prepared by the cluster process contain several types of pre-condensated polymolecular clusters. Their presence and different physico-chemical properties should influence the deposition process. The oriented structure on the surface can be explained by the preferential adsorption of polymolecular species onto the surface of the formed structures leading to the preferable nanocrystals growth. However, such a hypothesis requires further experimental confirmations.

The absorption coefficient of the prepared nanocrystalline thin films calculated from optical transmission spectra and film thickness evaluated from the SEM analysis are demonstrated in Figure 33. The prepared films containing pure nanocrystalline phases

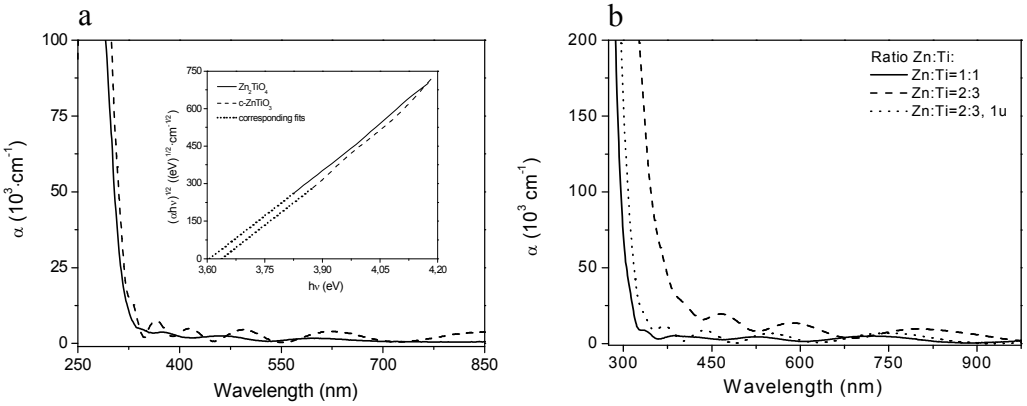

Figure 33 Optical properties of thin films annealed at 650°C. a) Films formed by nanocrystalline Zn_2TiO_4 or c-$ZnTiO_3$. In the inset is the fit allowing the estimation of the nature of electronic transition. b) Films formed by nanocrystalline c-$ZnTiO_3$ and the compound of c-$ZnTiO_3$ with r-TiO_2.

Zn_2TiO_4 and c-$ZnTiO_3$ exhibit the absorption edges around 300 nm. The form of the absorption edges and their fit with the corresponding Tauc function [90] displayed in the inset indicates that the band gap transitions of the formed structures have the character of the indirect transitions. The determined band gaps for Zn_2TiO_4 and c-$ZnTiO_3$ are 3.72 and 3.69 eV, respectively. It should be mentioned, that slow heating rates during the thermal annealing of Zn_2TiO_4 films could be accompanied by side formation of ZnO which is accompanied with a new strong absorption edge around 365 nm. Such an edge is often confused with the absorption edge of inverse spinel Zn_2TiO_4. Two different results can be achieved for the compounds prepared for the ratio of Zn:Ti equal to 2:3. If the input sol was doped by Eu^{3+} ions, the c-$ZnTiO_3$ nanocrystalline phase has been stabilized which is related to appearing the corresponding band gap and fine nanocrystalline structure as can be seen from Figure 33b and Figure 34a. The annealing of the undoped samples is accompanied by the crystallization of side-formed r-TiO_2. The formation of the r-TiO_2 nanocrystalline phase is related to a new absorption edge at 410 nm superposed to the absorption edge of r-$ZnTiO_3$. The nanocrystalline growth of the formed r-TiO_2 can be observed by SEM (see Figure 34b). From the beginning of the crystallization, r-TiO_2 tends to form elongated, fiber like nanocrystals that rapidly growth up introducing the opaque look of the film due to scattering phenomena. The estimated values of the band gap energy are 3.01 and 3.61 eV for r-TiO_2 and r-$ZnTiO_3$, respectively. All demonstrated results achieved on the prepared thin

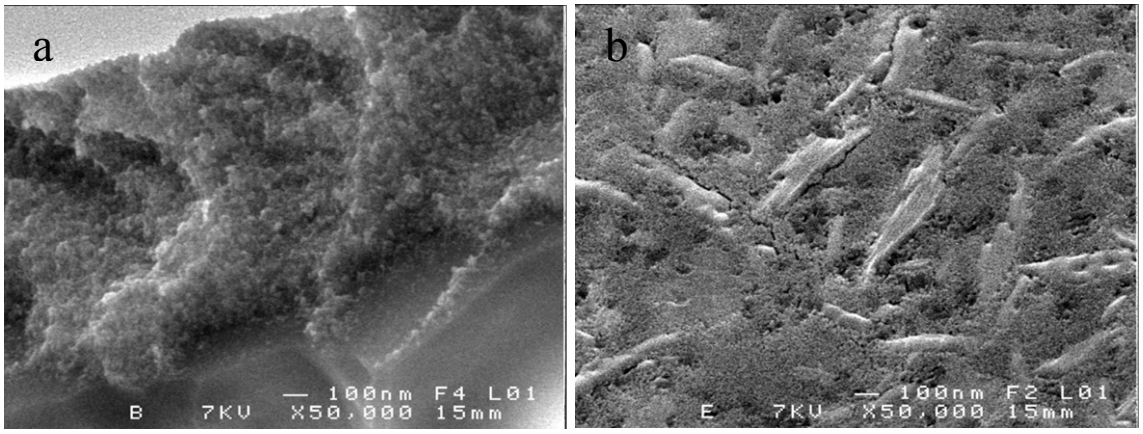

Figure 34 Structure of prepared nanocrystalline thin films annealed at 650°C. a) Cross-section of film formed by nanocrystalline c-$ZnTiO_3$. b) Surface of film formed by the compound of r-$ZnTiO_3$ with r-TiO_2.

films confirm the results concluded from the analysis carried on the corresponding sintered powders. The band gap energies of the particular phases are summarized in Figure 35.

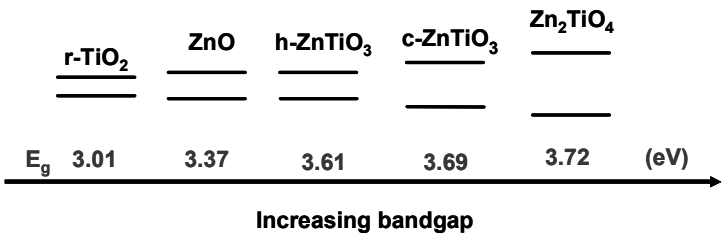

Figure 35 Summarization of experimentally determined values of energy gap for prepared $Zn_xTi_yO_z$ ternary phases and pure oxides.

Refractive indexes and dispersion curves were evaluated from ellipsometric measurements of the films deposed onto intrinsic (100) silicon wafers. Thicknesses of the prepared films analyzed by the surface profilometer and obtained from spectral ellipsometry differ by about 3 %. Spinel-like structures provide us with refractive indexes ranging from 1.69 to 1.95 at 633 nm as can be seen from Figure 36a. These values are significantly lowered for inverse spinel Zn_2TiO_4. Despite the fine surface structure and high morphological homogeneity of the formed film, the absorption coefficient of this compound is almost ten times higher than those of the other samples. The reason of such anomaly still has not been successfully explained and could be attributed to the formation of non-uniform boundaries during the deposition of individual layers. The value of the refractive index of c- $ZnTiO_3$ evaluated at 550 nm is 1.98 and is significantly higher than that of samples prepared by another sol-gel approach [58]. Samples prepared by the magnetron sputtering give the value close to 2.2 [56].

The observed decrease of the refractive index of the sol-gel derived films can be related to two main contributions. The first one is the porosity of the formed films and the second contribution is the presence of remaining amorphous phase. Both mentioned phenomena are supported by high fractions of nanocrystalline boundaries in the formed materials. It is possible to conclude that values of the determined refractive indexes of sol-gel

films are approximately by about 10 % lower than the values obtained from the corresponding bulk samples.

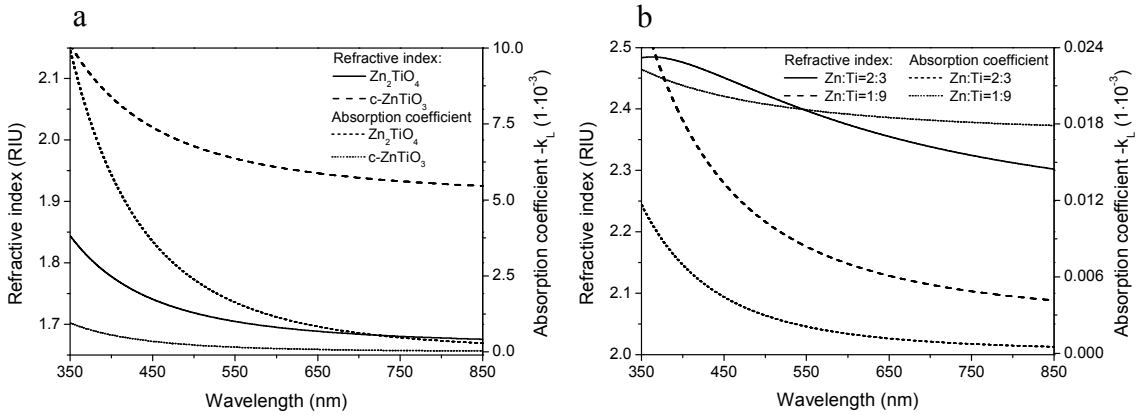

Figure 36 Results of ellipsometric measuments. Calculated refractive indexes and coefficient of optical losses for a) nanocrystalline Zn_2TiO_4 and c-$ZnTiO_3$, b) for different compounds of c-$ZnTiO_3$ with r-TiO_2.

Despite an experimental effort, nanocrystalline films of pure rhombohedral $ZnTiO_3$ haven't been successfully prepared. Although the annealing regime leading to the successful formation of pure r-$ZnTiO_3$ was employed, cubic phase of $ZnTiO_3$ was immediately transformed into inverse spinel Zn_2TiO_4 and r-TiO_2. The reason of the suppression of the cubic to rhombohedral transformation could be found in the interaction of the silicon substrate crystallizing in the cubic lattice with the cubic crystal lattice of the formed spinel like type. Although the compound of cubic and rhombohedral $ZnTiO_3$ with Zn_2TiO_4 and r-TiO_2 was prepared on pure silica glass substrates, the content of the formed rhombohedral $ZnTiO_3$ didn't exceed 40 at. %. Moreover, a long thermal annealing of films around 800 °C scales-up sizes of the formed nanocrystals and the formed films appear a high light scattering and became practically non-transparent. However, the properties of r-$ZnTiO_3$ could be estimated from optical properties of thin films with different ratios of Zn:Ti varying from 1:1 to 0:1.

According to the theory of effective media [81] one can presume that the square of the? refractive index of the alloyed compound can be expressed by a linear combination of squares of refractive indexes of particular constituents By this way refractive indexes of pure r-$ZnTiO_3$ and r-TiO_2 were calculated. The results of the calculated refractive index for r-$ZnTiO_3$ and r-TiO_2 determined for the wavelength of 550 nm are 2.60 and 2.05, respectively and for the wavelength of 633 nm are 2.56 and 2.01, respectively. Concerning r-TiO_2, the calculated value are by about 20 % smaller than the value of the corresponding bulk material described elsewhere [91]. The refractive index of r-$ZnTiO_3$ significantly exceeds the values of the other prepared ternary phases. Such a conclusion clearly results from the properties of rhombohedral crystal lattice and the calculated value does not exceed typical values determined for similar structures [92]

Properties of the prepared thin films including the EDS analysis are summarized in Table 13.

Table 13 Summarization of the composition and physico-chemical properties of prepared nanocrystalline films

Ratio Zn:Ti	2:1	1:1, Eu	2:3	1:9	pure phase
detected phases	Zn_2TiO_4	c-$ZnTiO_3$	r-$ZnTiO_3$ r-TiO_2	r-$ZnTiO_3$ r-TiO_2	r-$ZnTiO_3$
thickness (nm) (SE calculations)	428	883	529	279	-
$n_{633\ nm}$ (RIU)	1.690	1.949	2.361	2.134	2.56
E_g (eV)	3.72	3.69	3.49	3.25	3.61
c Zn (at.%) (EDS)	65.31	52.05	59.76	11.54	-
c Ti (at.%) (EDS)	34.69	45.78 (1.17 Eu)	40.24	88.46	-

Summary

Input sols prepared by the direct heteronucleation process with varying concentrations of Zn:Ti were used to prepare thin films formed by nanocrystalline ternary phases $Zn_xTi_yO_z$. These thin films were prepared by the dip-coating methods and subsequently annealed up to 650 °C. The annealing temperature and time can be used to tailor the size of the formed nanocrystals.

The formation of ternary phases $Zn_xTi_yO_z$ and their physico-chemical properties were investigated by the differential thermal analysis, UV-VIS spectroscopy, X-ray diffraction analysis, atomic force microscopy, scanning electron microscopy, surface profilometry and spectral ellipsometry. The chemical compositions of the prepared films were verified by energy-dispersive X-ray spectroscopy. Absorption coefficients, refractive indexes, dispersion curves and band gaps of the prepared films and pure phases were determined.

Thin films containing selected nanocrystalline ternary phases were successfully prepared. The thickness of the prepared films can be varied from several tens of nanometers up to few micrometers depending on viscosity, concentration of input sols, withdrawing speed and number of deposition cycles. All films formed by pure ternary phases appear an excellent structural and surface homogeneity with surface variations bellow 6 nm. Nanocrystal sizes ranging from 8 to 46 nm have been achieved depending on the film composition and the difference between the annealing temperature and the crystallization temperature of particular phases.

Inverse spinel Zn_2TiO_4 and cubic defect spinel $ZnTiO_3$ appear an absorption edge around 310 nm, a value of the band gap energy around 3.7 eV and the band gap transition corresponds to the indirect semiconductors. The determined values of the refractive indexes at the wavelength of 633 nm were 1.690 and 1.949 nm for inverse spinel Zn_2TiO_4 and cubic defect spinel $ZnTiO_3$, respectively. Rhombohedral $ZnTiO_3$ hasn't been successfully prepared probably due to the interaction of the substrate with the formed films. Optical properties of rhombohedral $ZnTiO_3$ were estimated from its compound with rutile TiO_2. The band gap energy was estimated to be 3.61 eV, the calculated refractive index at 633 nm reach the value of 2.56. All determined refractive indexes are significantly lower than those of the bulk samples. This difference could be attributed to high fractions of nanocrystalline boundaries of the formed nanocrystals which increases the porosity of the formed films and to the presence of remaining non-crystalline phases.

Preparation and characterization of optical fibers

The preparation of optical preform and optical fibers is sophisticated process. From a set of preliminary experiments an approach leading to the preparation of defect free homogenous preforms containing Er in ZnO-doped silica cores was evaluated. Several examples of unsuccessful experiments are presented in Appendix. Adequate results were achieved by two times repeated deposition of the input sol of zinc oxide nanoparticles doped by europium ions inside the silica frit with the consecutive annealing at 200 °C. The soaked frit was annealed at 650 °C for 24 hours under the oxygen flow of 50 $cm^3 \cdot min^{-1}$.

The prepared preform labeled SG 1069 was without observable defects, i.e. bubbles, cracks, and had a good transversal and longitudinal homogeneity. The refractive index profile of the preform demonstrated in Figure 37 correlates with the concentration profile of zinc and

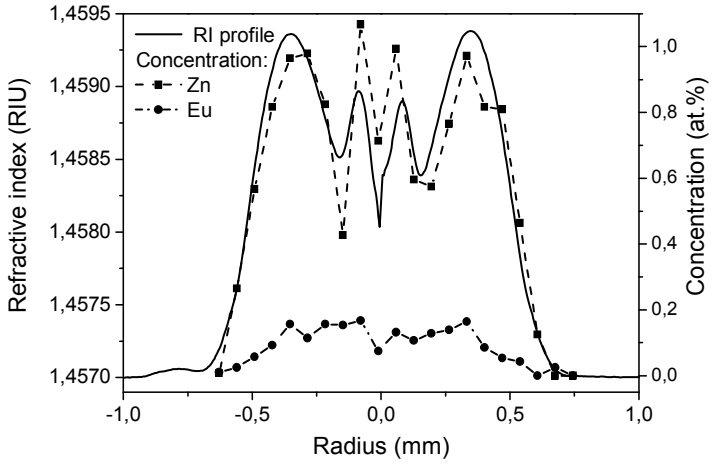

Figure 37 Refractive index profile of prepared perform (left scale) and concentration profile of dopants.

europium determined by the EDX analysis. The highest achieved concentration inside the preform core was around 1 at. % and 0.12 at. % for zinc and europium ions, respectively. From Figure 37 it is evident that the dopants are distributed symmetrically around the preform axis. The concentration of europium ions related to the concentration of zinc is approximately two times higher than that in the input sol. The use of the doped zinc oxide sol in combination with the silica frit supports the absorption and incorporation of Eu^{3+} ions inside the frit.

The prepared preform was withdrawn into an optical fiber with a standard outer diameter of 125 μm that was verified by optical microscopy on the cross-sections of the prepared fiber (see Figure 38a). The experimentally determined value of the fiber diameter of 124 μm is within the technological tolerance. The experimentally determined core diameter was about 15 μm. The longitudinal homogeneity of the core characteristics of the prepared fibers was of 10 m maximum. After some fiber length a small capillary was observed at the cladding-core boundary indicating the formation of small bubbles during the drawing process or the presence of submicron defects in the preform. The length of such capillary defects was several centimeters.

Presuming the conservation of values of the preform refractive indexes in the withdrawn fiber, the difference of the refractive index between the cladding and core of the fiber can be around 0.025 RIU. From Equation (16) the numerical aperture of the optical fiber

was calculated resulting to the value 0.084. Such a value was confirmed by the experimental measurement of the angular distribution of the output power from the fiber shown in Figure 38b. These achieved values are comparable with those of standard commercial or laboratory prepared single mode optical fibers. However, concentrations of europium ions in the fiber several times exceed those achieved by commonly used solution doping method [82], or modified solution doping method based on the deposition of nanocrystalline powders [7].

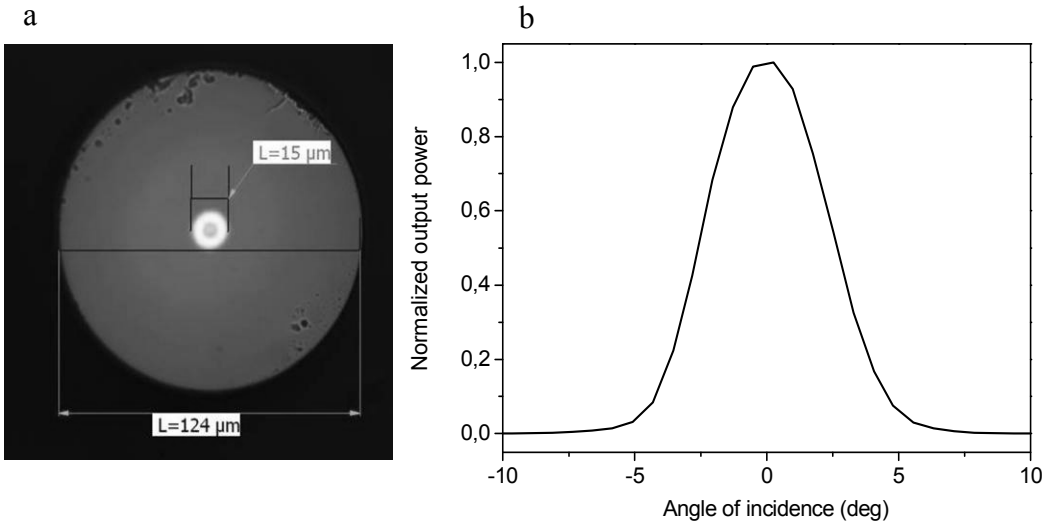

Figure 38 Properties of prepared optical fiber. a) Microscopic image with inserted dimensions. b) Angular distribution

The absorption spectra of the prepared fiber evaluated as spectral attenuation are shown in Figure 39. The background attenuation at 850 nm is around 0.9 dB·m^{-1}. In the

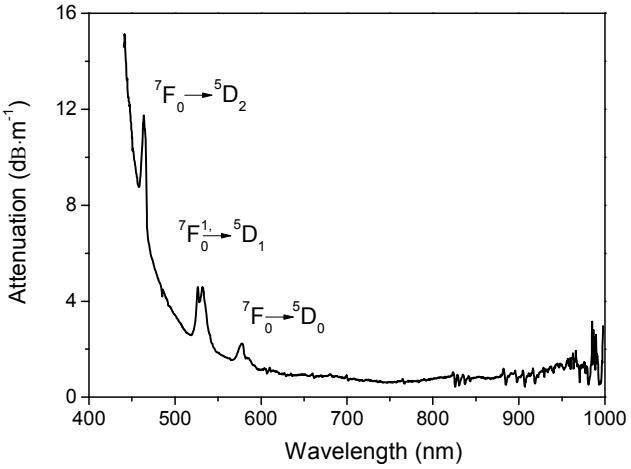

Figure 39 Attenuation of prepared optical fiber with marked optical transitions of Eu^{3+} ions.

spectra typical optical transitions of Eu^{3+} ions superposed over the edge of the absorption band below 450 nm are obvious. Because the position of the absorption edge bellow 450 nm strongly depends on the fiber length while the baseline attenuation remains constant, the absorption edge should be attributed to the electronic transition of formed structures based on

zinc oxide or silicates. Similar properties have been observed on Eu^{3+} doped zinc oxide powders [93].

Properties of the prepared optical fiber are summarized in Table 14 together with the properties of a multimode optical fiber prepared by the modified solution doping method. It can be concluded that the method employed in the thesis allows us to prepare optical fibers with novel matrices with high concentrations of rare earth elements. The approach will be extended to other REE, such an erbium and thulium, in a very close future.

Table 14 Parameters of prepared optical fiber and referred multi-mode fiber prepared by solution doping technique.

	Matrix	**Dopant**	**Dopant concentration (ppm)**	**Core diameter (μm)**	**Numerical aperture**	**Attenuation (850 nm) ($dB \cdot m^{-1}$)**
SG 1069	Zn	Eu	1200	15	0.084	0.9
Referred MM fiber [7]	Al	Er	740	14	0.143	0.005

Summary

The sol containing zinc oxide nanoparticles doped by Eu^{3+} ions was successfully applied into the silica frit deposited inside the silica tube. The tube with the thermally treated doped frit was thermally collapsed forming a preform. The preform was successfully withdrawn into optical fiber.

The prepared preform and optical fiber were analyzed by measuring refractive index profiles of the preform or angular distributions of the output power from the fiber or by energy-dispersive X-ray spectroscopy, optical microscopy, and UV-VIS spectroscopy,

The developed approach allows us to prepare optical fibers with high levels of rare earth elements. The use of ZnO nanoparticles in combination with a silica frit increases the adsorption of Eu^{3+} ions from the sol. The concentration of particular elements inside the preform was approximately 0.9 at. % of Zn^{2+} ions and 0.12 at. % of Eu^{3+} ions. The prepared optical fiber with the outer diameter of 124 μm and core diameter 15 μm has a numerical aperture equal to 0.084. Baseline losses of the prepared fiber were around 0.9 $dB \cdot m^{-1}$. These parameters of the prepared fiber correspond to that of the standard single mode optical fiber.

As was clearly demonstrated in this thesis, zinc oxide nanoparticles prepared by the sol-gel process can be successfully employed as a part of host matrices for rare earth elements allowing thus the preparation of active optical fibers with parameters close to optical fibers prepared by the standard or modified solution doping method. The presented experimental work will be extended to other rare earth elements, such an erbium and thulium, in a very close future, allowing the preparation of novel active optical fibers.

Conclusions

The presented thesis deals with the sol-gel synthesis of nanocrystalline ternary phases of the general formula $Zn_xTi_yO_z$, their characterization and potential for applications in photonics. Achieved results bring new fundamental knowledge about the processes leading to the formation of $Zn_xTi_yO_z$ nanocrystals from amorphous xerogels and give novel information about structural and opto-electrical properties of the prepared materials. The presented results allow us to prepare most of up-to-date reported $Zn_xTi_yO_z$ compounds with tailored nanocrystalline sizes and structures in forms of powders or thin films.

Two sol-gel approaches based on the cluster process and direct heteronucleation were employed to prepare input sols. These sols were optionally doped by Eu^{3+} ions to evaluate effects of rare earth elements to crystallization properties of the formed compounds. In the first part of the thesis crystallization properties and structural evolution of thermally treated xerogels were analyzed.

The direct heteronucleation approach leads to formation of uniform nanocrystals which readily grow up with increasing the temperature. The method can be used to prepare pure phases. The cluster process leads to nanocrystalline materials with the size ranging from 10 to 70 nm. However, the prepared samples contain significant amounts of side-formed phases. The explanation of this effect can be found in formation of polymeric clusters from $Ti_xO_y(OH)_z$ species in the input sols simultaneously to ZnO aggregates. Hence, the cluster process partially appears the character of the solid state reaction.

The crystallization of the prepared ternary phases occurs between 500 and 600 °C. The selected ratio Zn:Ti equal to 2:1 in the input sol is related to the thermally stable Zn_2TiO_4. The sol composition with the ratio Zn:Ti equal to 1:1 gives cubic defect spinel $ZnTiO_3$ which is partially transformed to rhombohedral $ZnTiO_3$. Finally, both $ZnTiO_3$ structures undergo the thermal dissociation to inverse spinel Zn_2TiO_4 and rutile r-TiO_2 at 990 °C.

The sol composition with the ratio of Zn:Ti equal to 2:3 provides us with the compound of rhombohedral $ZnTiO_3$ and rutile r-TiO_2 in case of undoped samples and the compound of cubic $ZnTiO_3$ and rutile r-TiO_2 in the case that Eu^{3+}ions were introduced into initial sol. Both mentioned compounds undergo the thermal dissociation to inverse spinel Zn_2TiO_4 and rutile r-TiO_2 above 900 °C. Sizes of the formed phases were calculated on the basis of the Debye-Scherrer's equation and verified by SEM observations.

The introducing of Eu^{3+} ions into the input sols mentioned above significantly changes the crystallization process initiating the formation of cubic spinel structures and blocking the cubic-to-rhombohedral transformation. Consequently, the crystallization temperatures are increased, nanocrystal growth is suppressed and formed nanocrystals appear more homogenous and with uniform shapes comparing to those of the undoped samples.

The strong red fluorescence and significant Stark splitting of ^7F_J peaks in emission spectra of Eu^{3+} ions confirm the successful incorporation of Eu^{3+}ions into the cubic spinel lattices. The comparison of photoluminescence intensities and asymmetric factors support the explanation that cubic $ZnTiO_3$ crystallizes in the defect spinel lattice. The presence of Eu^{3+} ions above the solubility limits in the formed compounds leads to the formation of cubic pyrochlore structure $Eu_2Ti_2O_7$.

Crystallization properties of inverse spinel Zn_2TiO_4 and its possible dopation by other rare earth elements were further investigated in this thesis. It was found, that results received for Eu^{3+} ions can be extended to other rare earth elements, namely Er^{3+} and Tm^{3+}. Solubility limits of rare earth elements inside prepared inverse spinel Zn_2TiO_4 were experimentally determined to be 0.5 at. %.

From the analysis of the crystallization peaks it was deduced, that the crystallization process of pure Zn_2TiO_4 can be characterized as homogenous nucleation followed by the three dimensional growth at a constant nucleation rate which finally pass into the cellular recrystallization controlled by the diffusion of matter. The crystallization process of Zn_2TiO_4 doped by Eu^{3+} ions has the character of the site saturated nucleation followed by the three dimensional growth and cellular recrystallization resulting into formation of smaller and more uniform nanocrystals.

Thus, the versatile approach allowing the preparation of inverse spinel Zn_2TiO_4, cubic defect spinel $ZnTiO_3$ and rhombohedral $ZnTiO_3$ with tailored nanocrystal sizes was developed in the thesis. By controlling the initial sol composition and thermal annealing of xerogels this approach allows us to prepare the selected ternary phase with tailored nanocrystals sizes ranging from tens of nanometers up to micrometric scale. The formed cubic structures can be doped by rare earth elements up to their limits of solubility.

In the second part of this thesis, the approaches elaborated in the first part were successfully exploited for the preparations of thin films with defined nanocrystalline structure and selected composition. Initial sols prepared by the direct heteronucleation process with varying concentration of Zn:Ti were used to apply thin gel films by the dip-coating methods which were subsequently heat-treated up to 650 °C. The films containing the selected nanocrystalline ternary phases were successfully prepared. The thickness of films prepared on the basis of the presented approaches can be varied from several tens of nanometers up to few micrometers depending on viscosity, concentration of input sols, withdrawing speed and number of deposition cycles.

All films appear an excellent structural and surface homogeneity allowing to determine selected optical and opto-electronic parameters of particular nanocrystalline phases. Inverse spinel Zn_2TiO_4 and cubic defect spinel $ZnTiO_3$ appear an absorption edge around 310 nm, band gap energy around 3.7 eV. Their band gap transitions have character typical for indirect semiconductors. The determined values of the refractive indexes at the wavelength 633 nm were of 1.690 and 1.949 for inverse spinel Zn_2TiO_4 and cubic defect spinel $ZnTiO_3$, respectively. Rhombohedral $ZnTiO_3$ has not been successfully prepared probably due to the interaction of the silicon substrate with formed films. Optical properties of rhombohedral $ZnTiO_3$ were estimated from its compound with rutile TiO_2. Its band gap energy was estimated to be 3.61 eV, the calculated refractive index at 633 nm reach the value of 2.56. All refractive indexes determined on the prepared films are significantly lower than those of the corresponding bulk materials. This difference could be attributed to high fractions of nanocrystalline boundaries of formed nanocrystals which increases the porosity of the formed films and to the presence of remaining non-crystallized phases.

In the third part of this thesis the potential for applying of selected compounds for the preparation of special optical fibers was investigated. Despite the decomposition of inverse spinel Zn_2TiO_4 caused by high temperatures during the fiber preparation, zinc oxide nanoparticles doped with Eu^{3+} were successfully exploited. The sol containing zinc oxide nanoparticles doped by Eu^{3+} ions was successfully applied into the silica frit deposited inside the silica tube. The tube with the thermally-treated doped frit was collapsed into a rod, the preform . The preform was successfully withdrawn into the optical fiber. The developed approach allows us to prepare optical fibers with a high level of rare earth elements.

The employment of Eu^{3+} doped ZnO nanoparticles and their immobilization in the silica frit increases the incorporation of Eu^{3+} ions into the frit from the sol. The concentration of particular elements inside the prepared preform was approximately 0.9 at. % of Zn^{2+} ions and 0.12 at. % of Eu^{3+} ions. The prepared optical fiber with the outer diameter of 124 μm and

the core diameter of 15 μm has the numerical aperture equal to 0.084. These parameters correspond to those of standard single mode optical fibers. Baseline losses of the prepared fiber was around 0.9 $dB \cdot m^{-1}$. The parameters of the prepared optical fiber are comparable with those of an optical fiber prepared by the solution doping approach

As the prepared spinel-derived structures appear a relatively wide band gap, they cannot be directly employed in the field of photocatalysis. However, the prepared films formed by r-$ZnTiO_3$/r-TiO_2 compounds were successfully tested as photocatalytic materials for degradation of fatty acids as was demonstrated elsewhere [94].

The thesis has clearly shown that spinel-derived structures allow introducing rare earth elements inside the crystal lattice. Owing to high optical transparency and excellent surface quality of prepared films, spinel-derived structures can be employed as materials for passive and active planar optical waveguides. One example is represented by c-$ZnTiO_3$ where the concentration of rare earth elements can reach several percent [58]. Recently, new materials based on nanocrystalline Zn_2TiO_4 films with high quality factors were prepared, making these compounds promising materials for applications as microwave dielectrics [95].

As was clearly demonstrated in the thesis zinc oxide nanoparticles prepared by the sol-gel process can be successfully employed as a part of host matrices for rare earth element incorporation allowing thus the preparation of active optical fibers with parameters close to optical fibers prepared by the standard or modified solution doping method. The presented experimental work will be extended to other rare earth elements, such an erbium and thulium, allowing the preparation of novel active optical fibers.

By comparing the results with the aims of this study, I can conclude that all objectives were successfully completed.

Résumé

Cette étude se rapporte à la préparation de phases ternaires de formule générale $Zn_xTi_yO_z$ par la voie sol-gel, à leur caractérisation et leur application éventuelle en photonique. Les résultats obtenus apportent des éléments nouveaux de connaissance fondamentale sur les processus de formation de nanocristaux $Zn_xTi_yO_z$ dans les xérogels amorphes. La thèse fournit aussi des nouvelles informations sur les propriétés structurales et opto-électriques des matériaux préparés. Sur la base des résultats présentés, la plupart de ces phases de type $Zn_xTi_yO_z$ peuvent être préparées sous forme de poudres ou de couches minces en contrôlant la taille et la structure nanocristalline.

Deux voies de synthèses sol-gel ont été utilisées pour préparer le sol initial : soit sur la base d'un processus de cluster et soit par hétéronucléation directe. Le sols ont été éventuellement dopés par des ions Eu^{3+} pour évaluer l'effet de la terre rare sur la cristallisation de composés formés. La première partie de notre étude analyse le phénomène de cristallisation et l'évolution structurale des xérogels avec le traitement thermique.

L'approche directe par hétéronucléation conduit à la formation de nanocristaux uniforme qui agrandi régulièrement avec la température augmente. La méthode peut être utilisée pour préparer les phases pures. Le procédé « cluster » conduit à un matériau nanocristallin avec des tailles allant de 10 à 70 nm. Cependant les échantillons ainsi préparés contiennent une quantité importante de phases secondaires. L'explication peut être trouvée dans la formation de clusters polymériques $Ti_xO_y(OH)_z$ dans les sols initiaux à côté des agrégats de ZnO. Ainsi, le processus cluster présente partiellement un caractère de réaction à l'état solide.

La cristallisation des phases ternaires préparés se produit entre 500 et 600 ° C. Lorsque le rapport Zn: Ti est égal à 2:1, on peut obtenir Zn_2TiO_4 qui est thermiquement stable. La composition avec le rapport Zn: Ti égal à 1 conduit à la spinelle déficitaire $ZnTiO_3$ qui est partiellement transformée en $ZnTiO_3$ rhomboédrique. Enfin, les deux structures $ZnTiO_3$ subissent une dissociation thermique à 990 °C en Zn_2TiO_4 spinelle inverse et rutile r-TiO_2. La composition avec le rapport de Zn: Ti égal à 2:3 conduit à un mélange de $ZnTiO_3$ rhomboédrique et de rutile r-TiO_2 dans le cas d'échantillons non dopés et un mélange de $ZnTiO_3$ cubique et de rutile r-TiO_2 dans le cas où des ions Eu^{3+} ont été introduits dans le sol initial. Les deux composés susmentionnés subissent une dissociation thermique en spinelle inverse Zn_2TiO_4 et rutile r-TiO_2 au dessus de 900 °C. La taille des nanocristaux des phases formées a été calculée sur la base de l'équation de Debye-Scherrer et vérifiée par les observations en Microscopie Electronique à Balayage (MEB).

L'introduction d'ions Eu^{3+} dans les sols influence de manière significative le processus de cristallisation, favorisant la formation de structures spinelle cubique et bloquant la transformation cubique - rhomboédrique. De c e fait, les températures de cristallisation sont augmentées, tandis que la croissance des nanocristaux est inhibée et que la distribution des nanocristaux formés semble plus homogène et uniforme, par comparaison avec des échantillons non dopés. La fluorescence rouge est intense et le dédoublement Stark ^7F_J des pics dans les spectres d'émission des ions Eu^{3+} confirme l'incorporation effective des ions Eu^{3+} dans une maille spinelle cubique. La comparaison des intensités de photoluminescence et les facteurs asymétriques viennent conforter la théorie selon laquelle le $ZnTiO_3$ cubique cristallise dans le réseau spinelle déficitaire. La présence d'ions Eu^{3+} au-dessus des limites de solubilité du composé formé conduit à la formation de pyrochlore cubique $Eu_2Ti_2O_7$.

La cristallisation du spinelle inverse Zn_2TiO_4 et son dopage possible par d'autres terres rares ont été étudiés de façon plus approfondie. Il a été démontré que les résultats observés avec les ions Eu^{3+} pouvaient être étendus à d'autres éléments de la famille des terres rares, à

savoir Er^{3+} et Tm^{3+}. Les limites de solubilité des terres rares à l'intérieur du spinelle inverse Zn_2TiO_4 ont été déterminées expérimentalement entre 0,5 à. 1 %. De l'analyse des pics exothermiques de cristallisation il a été déduit que le processus de cristallisation de Zn_2TiO_4 pur est régi par une nucléation homogène avec un taux de nucléation constant et une croissance tridimensionnelle. Celle-ci est tout d'abord contrôlée par l'interface (CCI/ Croissance Contrôlée par l'Interface) puis progressivement par la diffusion (CCD : Croissance Contrôlée par la Diffusion). Le processus de cristallisation de Zn_2TiO_4 dopé par des ions Eu^{3+} se caractérise par un nombre de nuclei constant (nucléation à saturation de sites) et une croissance tridimensionnelle, ce qui aboutit à la formation de nanocristaux plus petits et plus uniformes.

En conséquence, on arrive ainsi à une méthode souple qui permet la préparation de spinelle inverse Zn_2TiO_4, cubique, de spinelle déficitaire $ZnTiO_3$ et de $ZnTiO_3$ rhomboédrique avec des tailles de nanocristaux ajustables sur mesure. La composition initiale et le recuit thermique nous permettent de préparer et de sélectionner des phases ternaires avec des nanocristaux dont la taille peut être ajustée entre quelques dizaines de nanomètres et une échelle micrométrique. Les structures cubiques peuvent être dopées par des ions de terres rares jusqu'à leur limite de solubilité.

Dans la deuxième partie de l'étude, les approches explorées et affinées dans la première partie ont été exploitées avec succès pour la préparation des couches minces nanocristallines de structure et de composition sélectionnées. Les sols de départ ont été préparés par le procédé d'hétéronucléation directe, avec ajustement des concentrations respectives de Zn et de Ti. Des couches minces ont été obtenues par trempage puis recuit à 650 °C. Des couches contenant des phases ternaires nanocristallines sélectionnées ont été préparé avec succès. L'épaisseur de ces couches peut varier de quelques dizaines de nanomètres à quelques micromètres selon la viscosité, la concentration des sols initiaux, la vitesse de retrait et le nombre de cycles de dépôt.

Tous les films présentent une excellente homogénéité de structure et de surface, ce qui a permis de déterminer divers paramètres optiques et opto-électriques de certaines phases nanocristallines. Le spinelle inverse Zn_2TiO_4 et le spinelle déficitaire $ZnTiO_3$ ont un seuil d'absorption voisin de 310 nm, une énergie de bande interdite d'environ 3,7 eV. Cela leur confère un caractère indirect de semi-conducteurs. Les valeurs déterminées des indices de réfraction à la longueur d'onde de 633 nm sont de 1.690 et 1.949 pour le spinelle inverse Zn_2TiO_4 et le spinelle déficitaire $ZnTiO_3$. La phase rhomboédrique $ZnTiO_3$ n'a pas été préparée avec succès, probablement en raison de l'interaction du substrat avec des films formés. Les propriétés optiques de $ZnTiO_3$ rhomboédrique ont été estimées à partir de couches minces contenant aussi du rutile TiO_2. L'énergie de bande interdite a été estimée à 3,61 eV, et l'indice de réfraction calculé à 633 nm atteint la valeur 2,56. Tous les indices de réfraction déterminés laissent apparaître une diminution significative par comparaison avec des échantillons massifs. Ce phénomène doit être attribué à la haute teneur du film en nanocristaux formés, ce qui augmente la porosité des films ainsi qu'à la présence d'autres phases non cristallisées.

La troisième partie de notre étude se rapporte aux applications potentielles des matériaux synthétisés dans le domaine des fibres optiques. En dépit de la décomposition du spinelle inverse Zn_2TiO_4 pendant le recuit thermique de la préforme, les nanoparticules d'oxyde de zinc ont pu être exploitées avec succès. Le sol d'oxyde de zinc contenant des nanoparticules dopées par des ions Eu^{3+} a été introduit dans le « frit » de silice déposé à l'intérieur du tube de silice. Celui-ci a ensuite été thermiquement compacté, formant une préforme vitreuse. La préforme a finalement été étirée avec succès en fibre optique. Cette

méthode nous permet de préparer des fibres optiques à haut niveau de dopage par des terres rares. Les nanoparticules de ZnO en combinaison avec la silice vitreuse augmentent l'adsorption des ions Eu^{3+} à partir du sol. Les concentrations élémentaires dans le cœur de la préforme étaient d'environ 0,9 % d'ions Zn^{2+} et de 0,12 % d'ions Eu^{3+}. La fibre optique avait un diamètre extérieur de 124 μm et le diamètre de cœur de 15 μm pour une ouverture numérique égale à 0,084. Ces paramètres correspondent à une fibre optique monomode standard. L'atténuation de base de fibres se situe autour de 0,9 $dB \cdot m^{-1}$. On a comparés les paramètres de la fibre optique ainsi obtenue avec ceux d'une fibre optique dopée préparée par voie conventionnelle.

Parce que les spinelles et les structures dérivées présentent une largeur de bande relativement large, ils ne peuvent pas être directement utilisés dans le domaine de la photocatalyse. Cependant, les couches préparées avec des composés de type r-$ZnTiO_3$/r-TiO_2 ont été testées avec succès en tant que matériaux photocatalytiques pour la dégradation des acides gras, comme cela l'a été montré ailleurs[94]: Puisque l'on a confirmé que des éléments de terres rares peuvent être introduits à l'intérieur du réseau cristallin dans la structure spinelle. Avec la haute transparence optique et l'excellente qualité de surface des films préparés, ces spinelles peuvent être utilisés comme matériau actif et passif pour guides d'ondes optiques planaires. C'est notamment le cas du c-$ZnTiO_3$ où la concentration en terres rares peut atteindre plusieurs pour cent [58]. Récemment, de nouveaux matériaux basés sur des films nanocristallins de Zn_2TiO_4 avec un très bon facteur de qualité ont été préparés, ce qui les rend prometteurs comme matériaux diélectriques pour application en micro-ondes [95].

Enfin, il a été clairement démontré que des nanoparticules d'oxyde de zinc préparées par voie sol-gel peuvent être utilisées avec succès comme matrices d'accueil pour les terres rares, permettant la préparation des fibres optiques actives, avec des paramètres proches de ceux des fibres optiques préparées de façon standard ou par la méthode de dopage modifiée. Le travail expérimental présenté sera étendu à d'autres terres rares, notamment erbium et thulium, ouvrant la voie à la préparation de nouvelles fibres optiques actives.

En conclusion, les résultats obtenus à l'issue de cette étude recouvrent largement l'ensemble des objectifs initialement fixés.

Appendixes

Appendix 1. Mass spectrometry spectra of selected fragments [96]

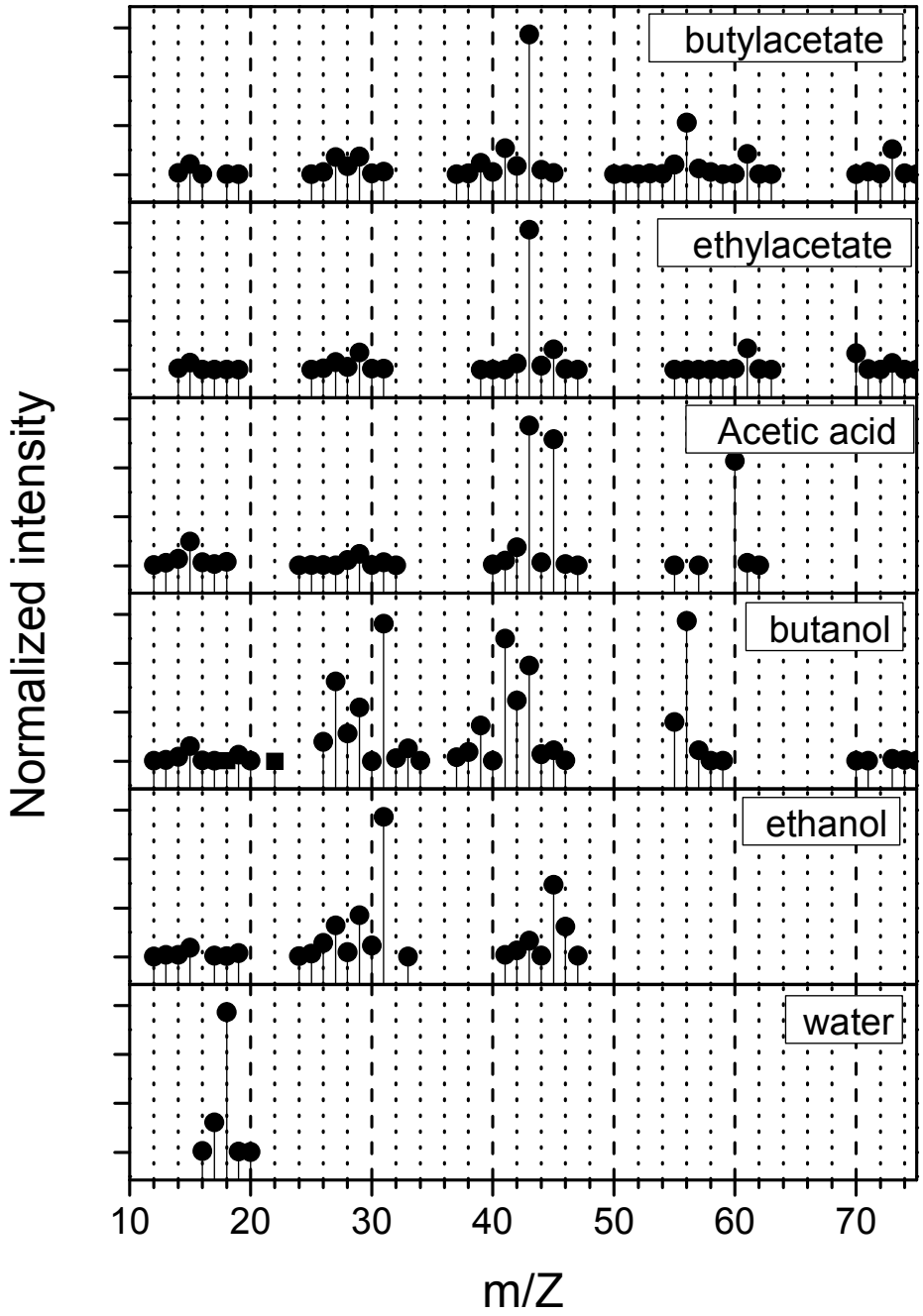

Supplementary figure 1 MS spectra for selected compounds

Appendix 2. XRD patterns for samples prepared by cluster process

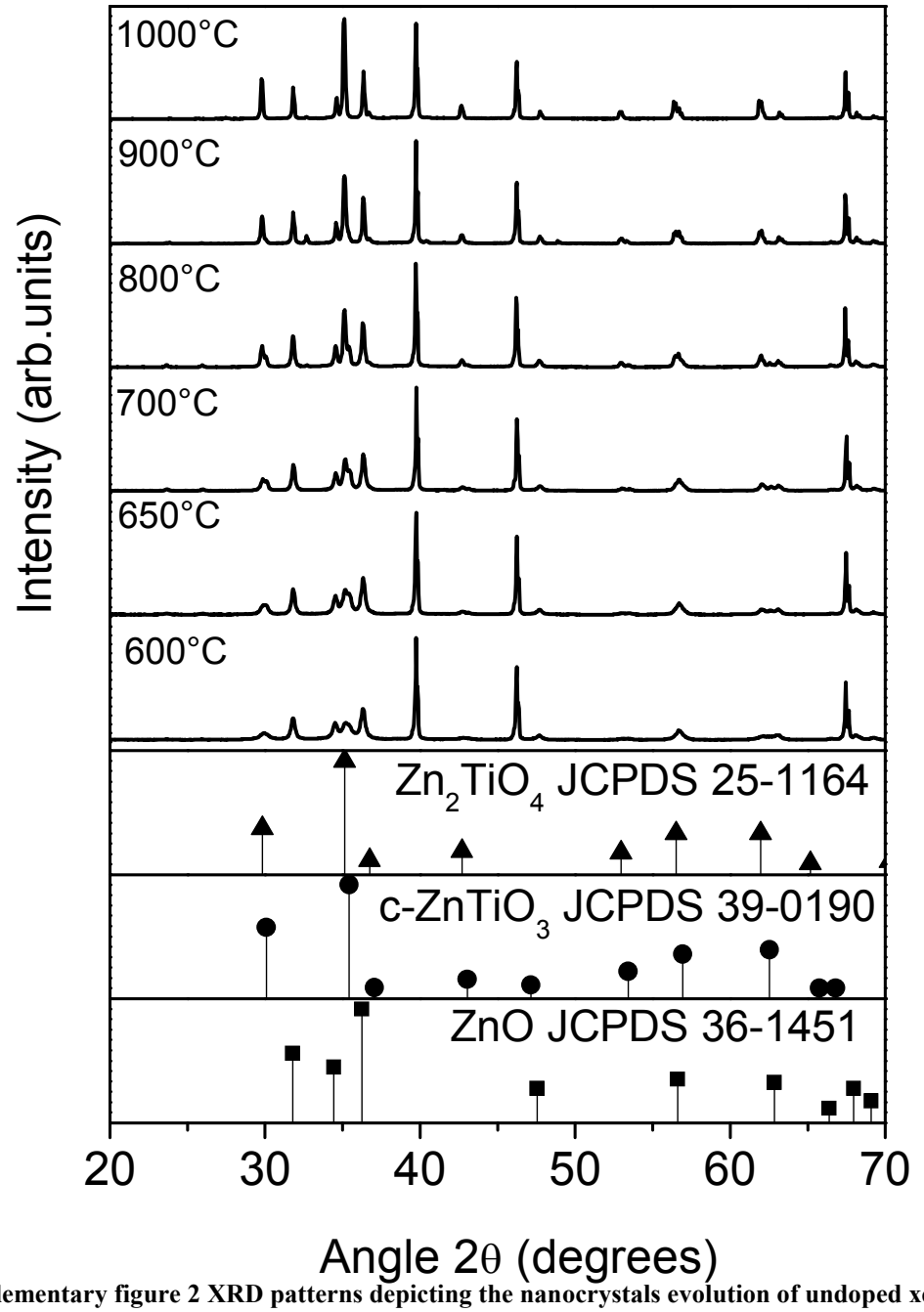

Supplementary figure 2 XRD patterns depicting the nanocrystals evolution of undoped xerogels prepared by the cluster process for the ratio Zn:Ti=2:1. Peaks positions 39.76, 46,24 and 67.45 ° depict the platinum reference standard according to the JCPDS file N° 04-0802.

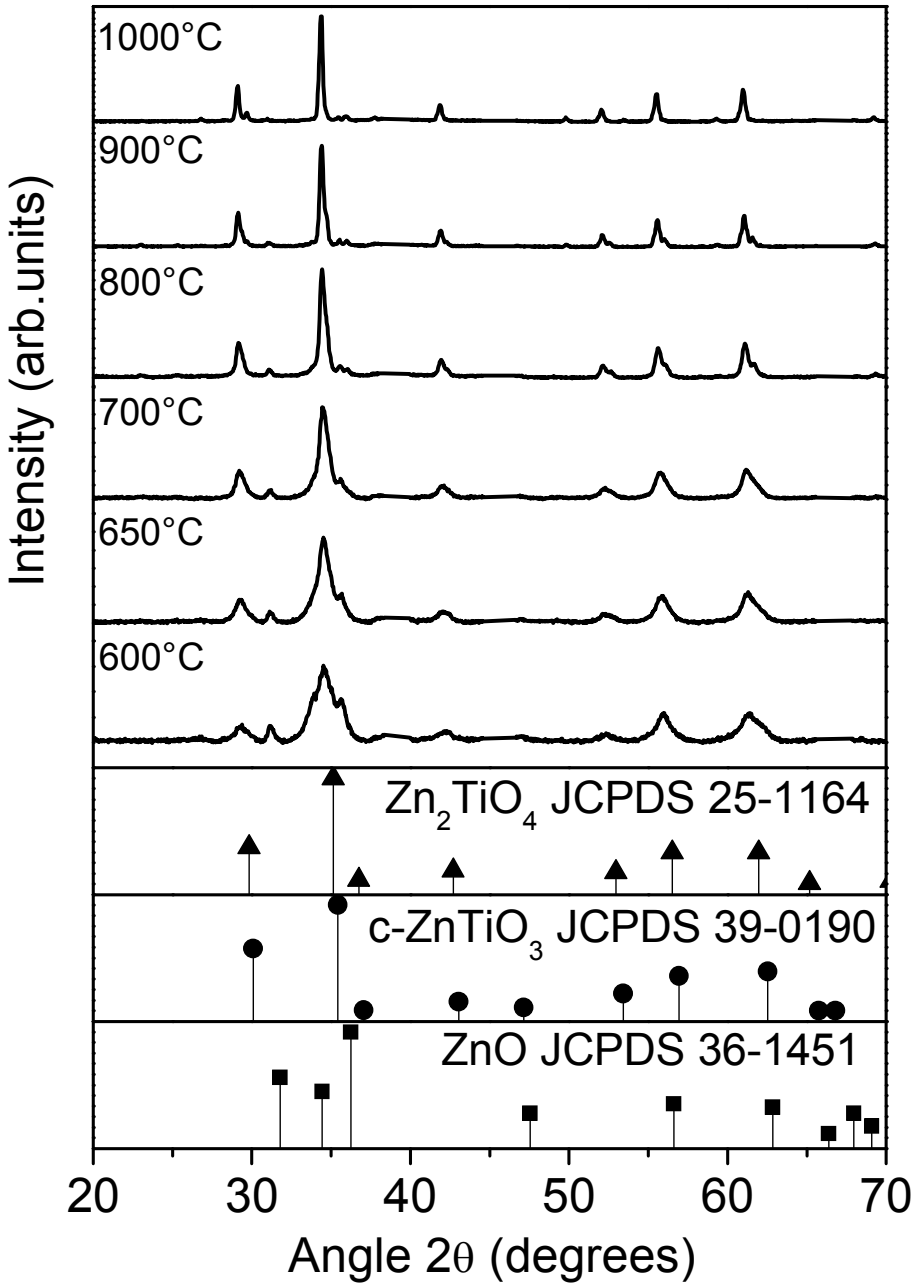

Supplementary figure 3 XRD patterns depicting the nanocrystals evolution of xerogels doped by 1 at. % Eu prepared by the cluster process for the ratio Zn:Ti=2:1.

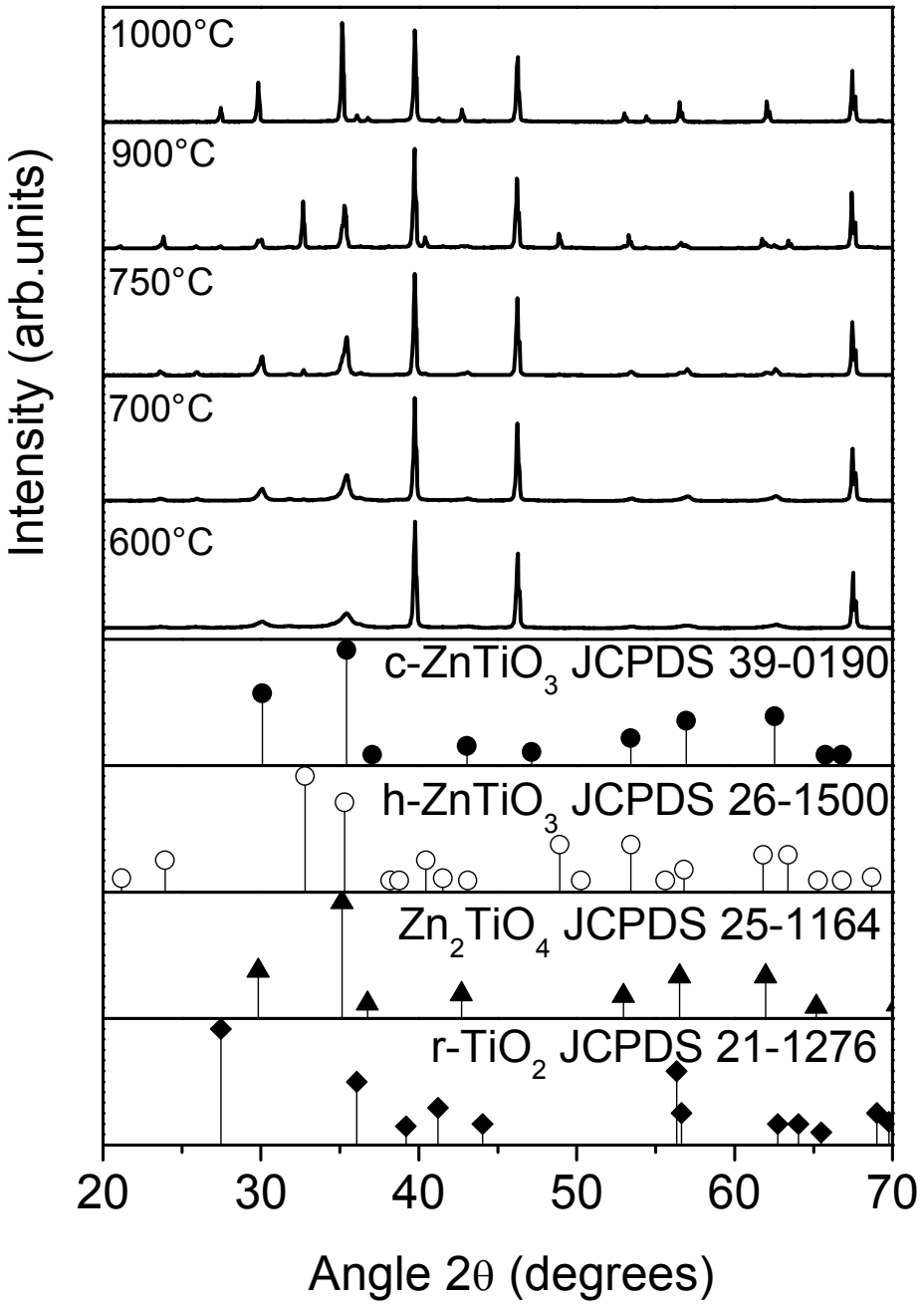

Supplementary figure 4 XRD patterns depicting the nanocrystals evolution of xerogels doped by 1 at. % prepared by the cluster process for the ratio Zn:Ti=1:1. Peaks positions 39.76, 46,24 and 67.45 ° depict the platinum reference standard according to the JCPDS file N° 04-0802.

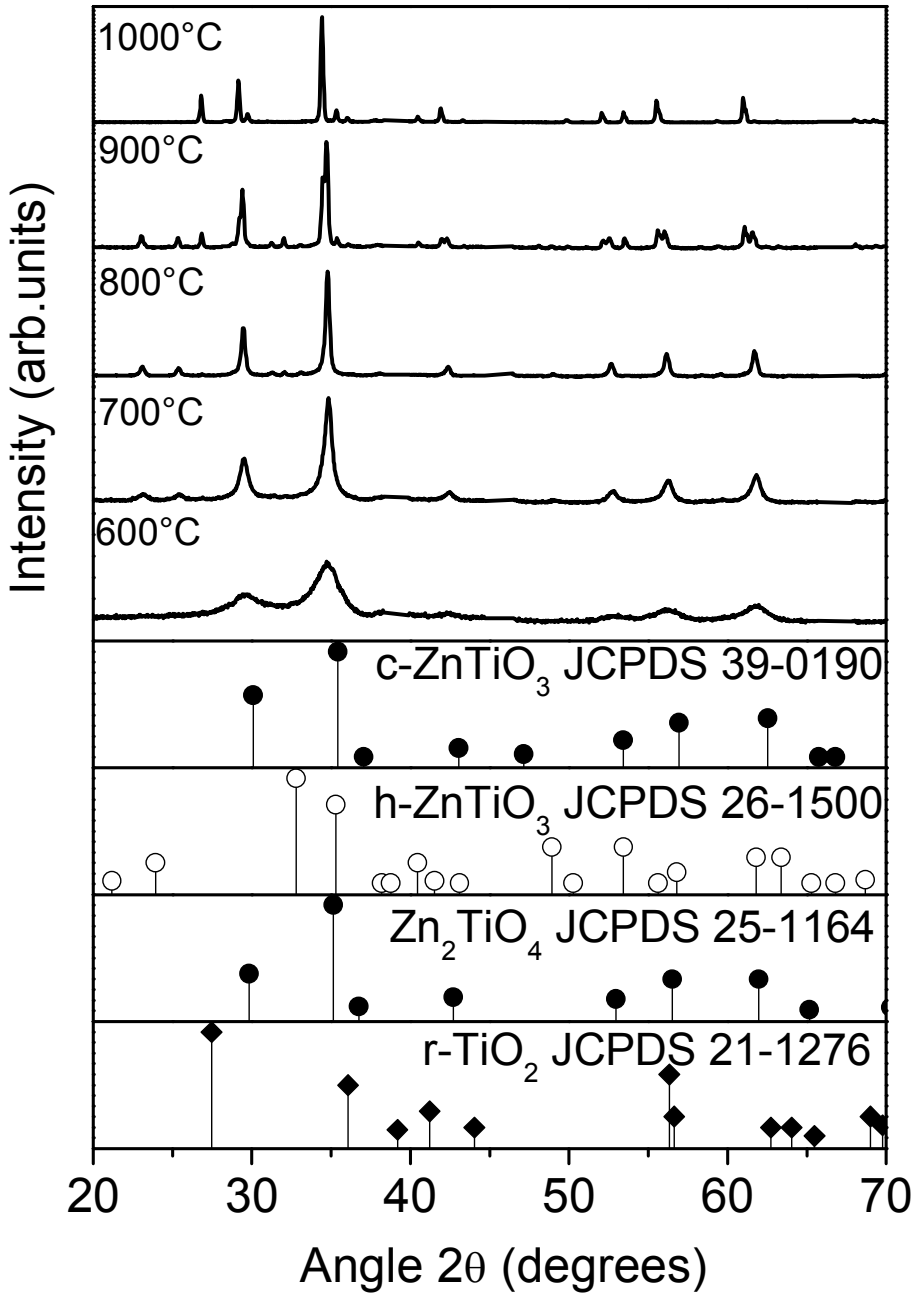

Supplementary figure 5 XRD patterns depicting the nanocrystals evolution of undoped xerogels prepared by the cluster process for the ratio Zn:Ti=1:1.

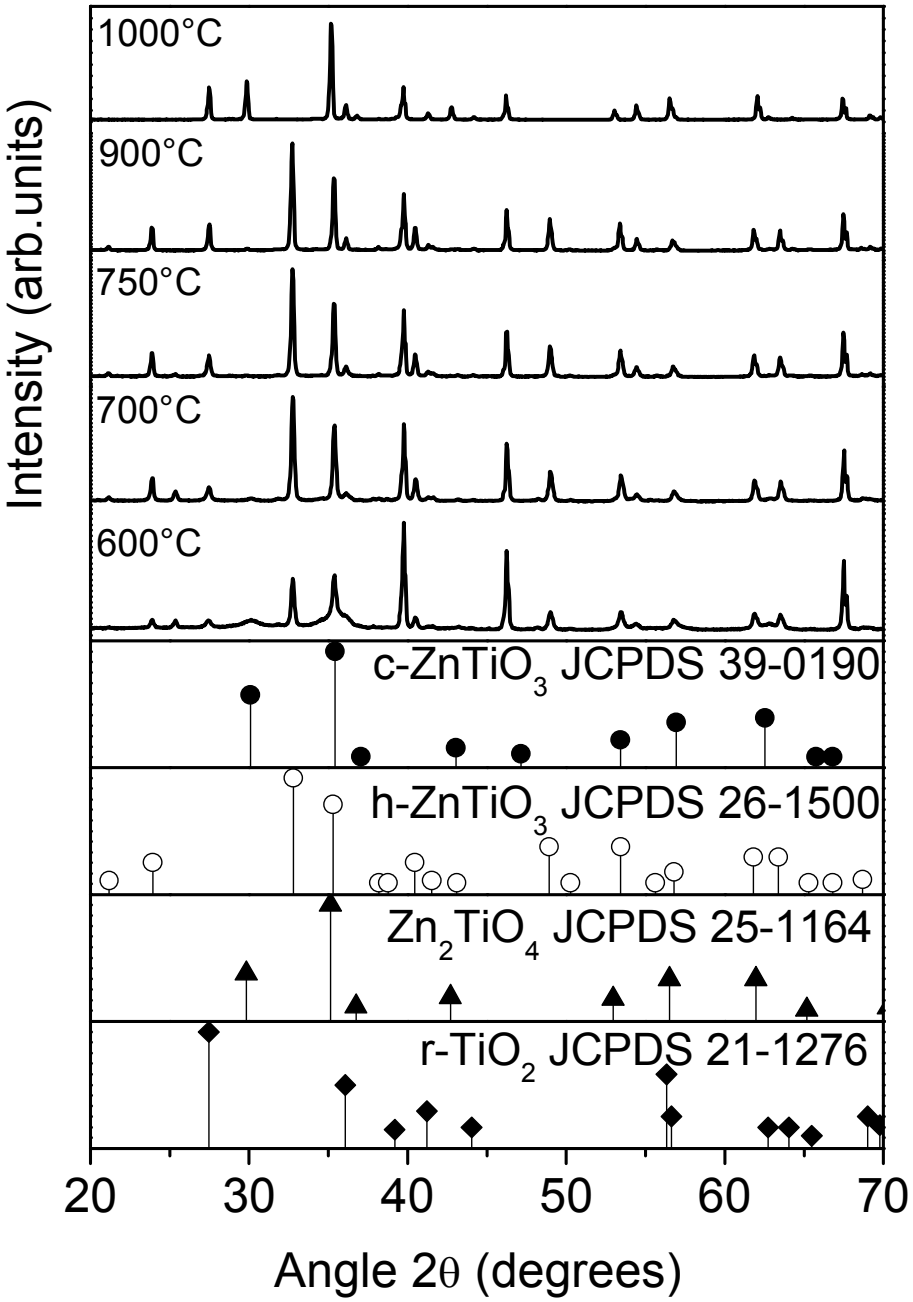

Supplementary figure 6 XRD patterns depicting the nanocrystals evolution of undoped xerogels prepared by the cluster process for the ratio Zn:Ti=2:3. Peaks positions 39.76, 46,24 and 67.45 ° depict the platinum reference standard according to the JCPDS file N° 04-0802.

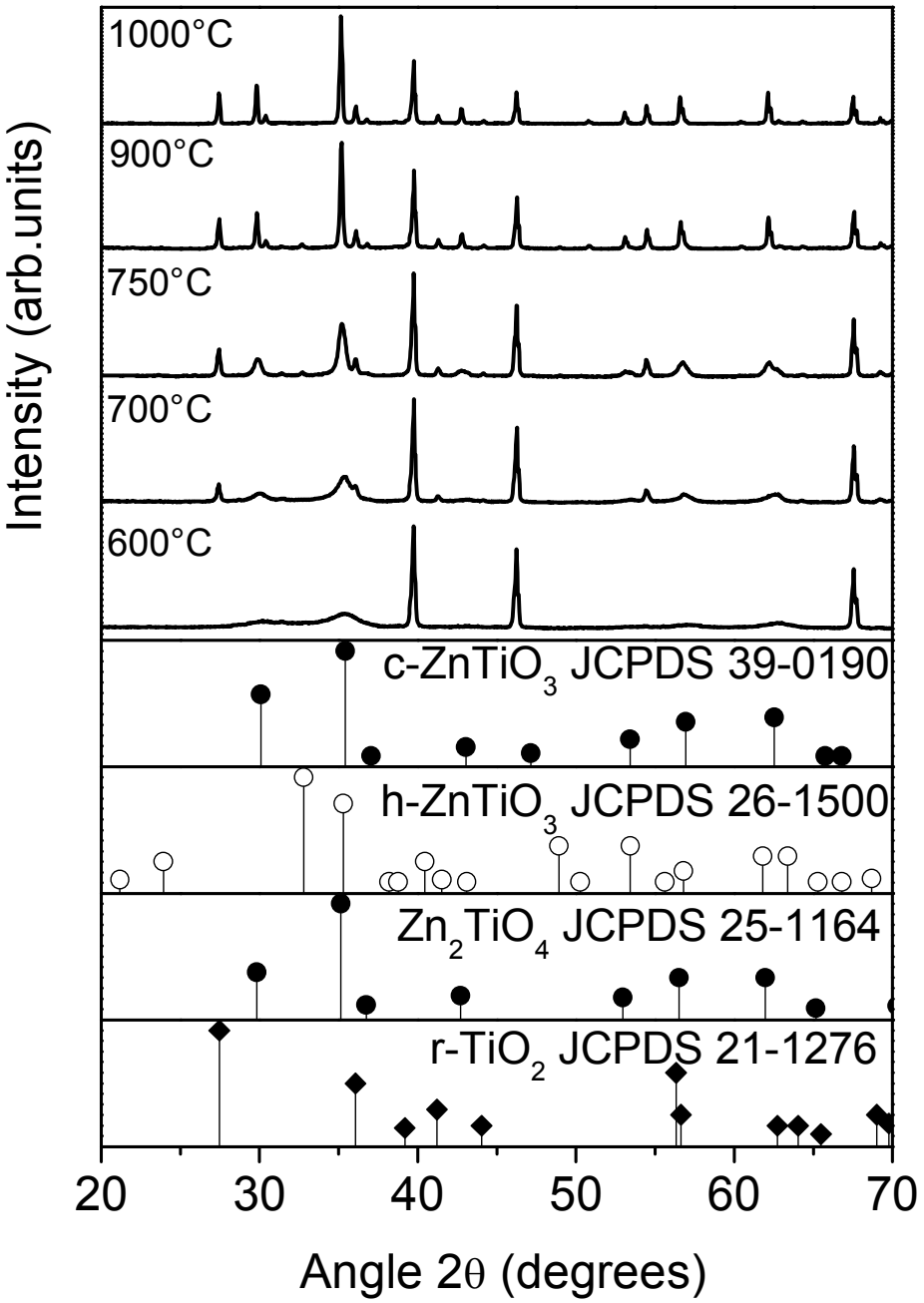

Supplementary figure 7 XRD patterns depicting the nanocrystals evolution xerogels doped by 1 at. % prepared by the cluster process for the ratio Zn:Ti=2:3. Peaks positions 39.76, 46,24 and 67.45 ° depict the platinum reference standard according to the JCPDS file N° 04-0802.

Appendix 3 Examples of unsuccessfully prepared optical preforms

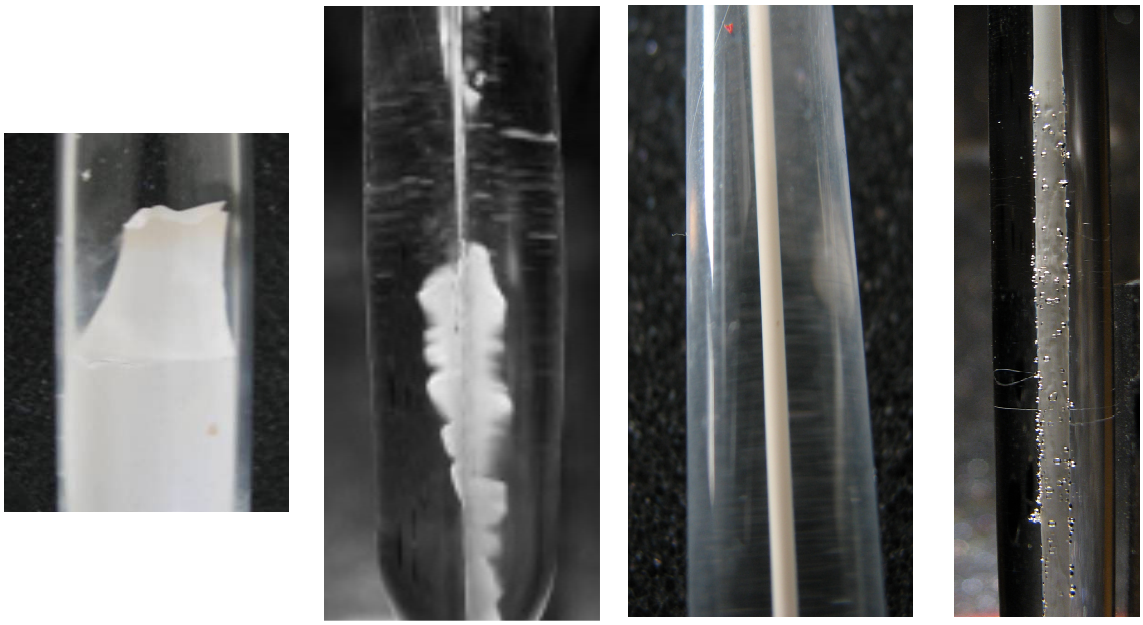

Supplementary figure 8 Examples of unsuccessfully prepared optical preforms. From the left: 1) delamination of prepared frit during the sintering, 2) delamination of prepared frit during the thermal collapse, 3) side crystallization of the core, 4) side crystallization of the core accompanied by local evaporation of dopants.

References

1. Miller, S.E. and A.G. Chynoweth, *Optical fiber telecommunications*. 1979: New York : Academic Press.
2. Springer, T., M. Piliarik, and J. Homola, *Real-time monitoring of biomolecular interactions in blood plasma using a surface plasmon resonance biosensor.* Analytical and Bioanalytical Chemistry, 2010. **398**(5): p. 1955-1961.
3. Schrofel, J. and K. Novotný, *Optické vlnovody*. 1986, Praha: SNTL.
4. Marques, A.C. and R.M. Almeida, *Raman spectra and structure of multicomponent oxide planar waveguides prepared by sol-gel.* Journal of Sol-Gel Science and Technology, 2006. **40**(2-3): p. 371-378.
5. Peterka, P., et al., *Experimental demonstration of novel end-pumping method for double-clad fiber devices.* Optics Letters, 2006. **31**(22): p. 3240-3242.
6. d'Acapito, F., et al., *Role of CaO addition in the local order around Erbium in SiO2-GeO2-P2O5 fiber preforms.* Materials Science and Engineering B-Solid State Materials for Advanced Technology, 2008. **146**(1-3): p. 167-170.
7. Dhar, A., et al., *Fabrication of high aluminium containing rare-earth doped fiber without core-clad interface defects.* Optics Communications, 2010. **283**(11): p. 2344-2349.
8. Coto-Garcia, A.M., et al., *Nanoparticles as fluorescent labels for optical imaging and sensing in genomics and proteomics.* Analytical and Bioanalytical Chemistry, 2011. **399**(1): p. 29-42.
9. Barick, K.C., et al., *Porosity and photocatalytic studies of transition metal doped ZnO nanoclusters.* Microporous and Mesoporous Materials, 2010. **134**(1-3): p. 195-202.
10. Smirnova, N., et al., *Synthesis and characterization of photocatalytic porous Fe3+/TiO2 layers on glass.* Journal of Sol-Gel Science and Technology, 2001. **22**(1-2): p. 109-113.
11. Urlacher, C., et al., *Planar ZrO2 waveguides prepared by the sol-gel process: Structural and optical properties.* Journal of Sol-Gel Science and Technology, 1997. **8**(1-3): p. 999-1005.
12. Mais, N., et al., *Er doped nanocrystalline ZnO planar waveguide structures for 1.55 mu m amplifier applications.* Applied Physics Letters, 1999. **75**(14): p. 2005-2007.
13. Grieve, K., P. Mulvaney, and F. Grieser, *Synthesis and electronic properties of semiconductor nanoparticles/quantum dots.* Current Opinion in Colloid & Interface Science, 2000. **5**(1-2): p. 168-172.
14. Djurisic, A.B., A.M.C. Ng, and X.Y. Chen, *ZnO nanostructures for optoelectronics: Material properties and device applications.* Progress in Quantum Electronics, 2010. **34**(4): p. 191-259.
15. Spanhel, L. and M.A. Anderson, *Synthesis of porous quantum-size CdS membranes - photoluminescence phase-shift and demodulation measurements.* Journal of the American Chemical Society, 1990. **112**(6): p. 2278-2284.
16. Sutter, J.U., D.J.S. Birch, and O.J. Rolinski, *The effect of intensity of excitation on CdSe/ZnS quantum dots: Opportunities in luminescence sensing.* Applied Physics Letters, 2011. **98**(2).
17. Hoffmann, M.R., et al., *Environmental applications of semiconductor photocatalysis.* Chemical Reviews, 1995. **95**(1): p. 69-96.
18. Zahradnik, R. and R. Polak, *Zaklady kvantove chemie*. 1976, Praha: SNTL. 440.

19. Bartram, S.F. and R.A. Slepetys, *Compound Formation and Crystal Structure in the System ZnO-TiO2.* Journal of the American Ceramic Society, 1961. **44**(10): p. 493-499.
20. Mills, A. and S. LeHunte, *An overview of semiconductor photocatalysis.* Journal of Photochemistry and Photobiology a-Chemistry, 1997. **108**(1): p. 1-35.
21. Spanhel, L., *Colloidal ZnO nanostructures and functional coatings: A survey.* Journal of Sol-Gel Science and Technology, 2006. **39**(1): p. 7-24.
22. Hoel, C.A., et al., *Transparent Conducting Oxides in the ZnO-In(2)O(3)-SnO(2) System.* Chemistry of Materials, 2010. **22**(12): p. 3569-3579.
23. Odobel, F., et al., *New Photovoltaic Devices Based on the Sensitization of p-type Semiconductors: Challenges and Opportunities.* Accounts of Chemical Research, 2010. **43**(8): p. 1063-1071.
24. Nah, Y.C., I. Paramasivam, and P. Schmuki, *Doped TiO(2) and TiO(2) Nanotubes: Synthesis and Applications.* Chemphyschem, 2010. **11**(13): p. 2698-2713.
25. Wang, K.P. and H.S. Teng, *Zinc-doping in TiO2 films to enhance electron transport in dye-sensitized solar cells under low-intensity illumination.* Physical Chemistry Chemical Physics, 2009. **11**(41): p. 9489-9496.
26. Ozgur, U., D. Hofstetter, and H. Morkoc, *ZnO Devices and Applications: A Review of Current Status and Future Prospects.* Proceedings of the Ieee, 2010. **98**(7): p. 1255-1268.
27. Spanhel, L. and M.A. Anderson, *Semiconductor clusters in the sol-gel process - quantized aggregation, gelation, and crystal-growth in concentrated ZnO colloids.* Journal of the American Chemical Society, 1991. **113**(8): p. 2826-2833.
28. Kratochvil, B., *Chemie a fyzika pevnych latek. 1.* 1994, Praha: VSCHT Praha. 233.
29. Kraus, I., *Struktura a vlastnosti krystalu*. 1993, Praha: Academia.
30. Pineda, M., et al., *Characterization of zinc oxide and zinc ferrite doped with Ti or Cu as sorbents for hot gas desulphurization* Applied Surface Science, 1997. **119**(1-2): p. 1-10.
31. Chen, Z.X., et al., *Dehydrogenation of Isobutane over Zinc Titanate Thin Film Catalysts.* Journal of Catalysis, 1996. **161**(2): p. 730-741.
32. Xiuhua, L., et al., *Preparation of Zn/TiO2 powder and its photocatalytic performance for oxidation of P-nitrophenol.* Nuclear Science and Techniques, 2007. **18**(1): p. 59-64.
33. Berthebaud, D., et al., *Tunable Optical Absorption on "ZnxTixO4-3yN2y" Nanosized Spinel Powders.* Journal of Physical Chemistry C, 2007. **111**(22): p. 7883–7888.
34. Kapoor, P.N., et al., *Aerogel processing of MTi2O5 (M = Mg, Mn, Fe, Co, Zn, Sn) compositions using single source precursors: synthesis, characterization and photocatalytic behavior.* Journal of Molecular Catalysis A: Chemical, 2005. **229**(1-2): p. 145-150.
35. Grasset, F., L. Spanhel, and S. Ababou-Girard, *New nanocrystalline colored oxynitride thin films from Ti4+-functionalized ZnO nanocolloids.* Superlattices and Microstructures, 2005. **38**(4-6): p. 300-307.
36. Grasset, F., et al., *From ZnO colloids to nanocrystalline colored ZnxTiyOw-zNz spinel films.* Advanced Materials, 2005. **17**(3): p. 294-297.
37. Starukh, G., et al., *Photoactivity of sol-gel derived nitridated ZnxTiyOz-films.* Zeitschrift Fur Physikalische Chemie-International Journal of Research in Physical Chemistry & Chemical Physics, 2007. **221**(3): p. 349-360.
38. Mayén-Hernández, S.A., et al., *Optical and structural properties of ZnO + Zn2TiO4 thin films prepared by the sol-gel method* Journal of Materials Science: Materials in Electronics, 2007. **18**(11): p. 1127-1130.

39. Shi, L., et al., *Co-emission of UV, violet and green photoluminescence of ZnO/TiO2 thin film.* Materials Letters, 2007. **61**(25): p. 4735-4737.
40. Wang, S.F., et al., *Photoluminescence of sol–gel derived ZnTiO3:Ni2+ nanocrystals.* Chemical Physics Letters, 2003. **373**(1-2): p. 223-227.
41. Manik, S.K. and S.K. Pradhan, *Preparation of nanocrystalline microwave dielectric Zn2TiO4 and ZnTiO3 mixture and X-ray microstructure characterization by Rietveld method.* Physica E-Low-Dimensional Systems & Nanostructures, 2006. **33**(1): p. 69-76.
42. Kim, H.T., et al., *Titanium Incorporation in Zn2TiO4 Spinel Ceramics.* Journal of the American Ceramic Society, 2001. **84**(5): p. 1081-1086.
43. Chaouchi, A., et al., *Low temperature sintering of ZnTiO3/TiO2 based dielectric with controlled temperature coefficient.* Journal of the European Ceramic Society, 2007. **27**(7): p. 2561-2566.
44. Yang, J. and J.H. Swisher, *The phase stability of Zn2Ti3O8.* Materials Characterization, 1996. **37**(2-3): p. 153-159
45. Steinike, U. and B. Wallis, *Formation and Structure of TibondZn-Oxides.* Crystal Research and Technology, 1997. **32**(1): p. 187-193.
46. Li, C., et al., *Precipitate within the spinel-type Zn2TiO4 matrix studied by high-resolution analytical transmission electron microscopy.* Materials Research Bulletin, 1961. **35**(3): p. 351-358.
47. Liu, X.C., et al., *Effects of WO3 additions on the phase structure and transition of zinc titanate ceramics.* Journal of Alloys and Compounds, 2008. **450**(1-2): p. 440-445.
48. Chaouchi, A., et al., *ZnTiO3 ceramic sintered at low temperature with glass phase addition for LTCC applications.* Materials Chemistry and Physics, 2007. **103**(1): p. 106-111.
49. Yamaguchi, O., et al., *Formation and Transformation of $ZnTiO_3$.* Journal of American Ceramic Society, 1987. **70**(5): p. C97-C98.
50. Chang, Y.S., et al., *The structure and properties of zinc titanate doped with strontium.* Journal of Alloys and Compounds, 2003. **354**(1-2): p. 303-309.
51. Zhao, L.L., et al., *Preparation and characterizations of ZnTiO3 powders by sol-gel process.* Journal of Sol-Gel Science and Technology, 2005. **33**(1): p. 103-106.
52. Hosono, E., et al., *Low-Temperature Synthesis of Nanocrystalline Zinc Titanate Materials with High Specific Surface Area.* Journal of the American Ceramic Society, 2004. **87**(9): p. 1785-1788.
53. Luo, J., et al., *Synthesis and characterization of (Zn,Co)TiO3 by modified low temperature preparing route.* Journal of Alloys and Compounds, 2005. **402**(1-2): p. 263-268.
54. Phani, A.R., M. Passacantando, and S. Santucci, *Synthesis of nanocrystalline ZnTiO3 perovskite thin films by sol–gel process assisted by microwave irradiation.* Journal of Physics and Chemistry of Solids, 2007. **68**(3): p. 317-323.
55. Wang, L., et al., *Low-temperature synthesis of ZnTiO3 nanopowders.* Journal of Crystal Growth, 2009. **311**(5): p. 611-614.
56. Ye, C., et al., *Preparation and optical properties of nanocrystalline thin films in the ZnO-TiO2 system.* Applied Physics A: Materials Science & Processing, 2008. **90**(2): p. 375-378.
57. Jung, J.S., et al., *Dielectric properties of zinc titanate thin films prepared by Rf magnetron sputtering.* Journal of Electroceramics, 2008. **23**(2-4): p. 272-276.
58. Aubert, T., et al., *Synthesis and characterization of Eu(3+), Ti(4+)@ZnO organosols and nanocrystalline c-ZnTiO(3) thin films aiming at high transparency and luminescence.* Science and Technology of Advanced Materials, 2010. **11**(4).

59. Chang, Y.S., et al., *Synthesis and characterization of zinc titanate nano-crystal powders by sol-gel technique.* Journal of Crystal Growth, 2002. **243**(2): p. 319-326.
60. Li, B., et al., *Low-fired microwave dielectrics in ZnO-TiO2 ceramics doped with CuO and B2O3.* Journal of Materials Science-Materials in Electronics, 2002. **13**(7): p. 415-418.
61. Kim, J.W., et al., *Synthesis and characterization of the ZnO-TiO2 nanoparticles by a hydrothermal processing*, in *Fracture and Damage Mechanics V, Pts 1 and 2*, M.H. Aliabadi, et al., Editors. 2006. p. 1297-1300.
62. Liu, X.C., et al., *Low-temperature cofiring behavior of ZnTiO3 dielectrics/NiZnCu ferrite composites.* Journal of Alloys and Compounds, 2009. **470**(1-2): p. 269-272.
63. Liu, Z.C., et al., *Studies on a basic question of zinc titanates.* Journal of Alloys and Compounds, 2009. **475**(1-2): p. 840-845.
64. Chaves, A.C., et al., *Photoluminescence in disordered Zn2TiO4.* Journal of Solid State Chemistry, 2006. **179**(4): p. 985-992.
65. Aubert, T., et al., *Synthesis and characterization of Eu(3+), Ti(4+)@ZnO organosols and nanocrystalline c-ZnTiO(3) thin films aiming at high transparency and luminescence.* Science and Technology of Advanced Materials, 2010. **11**(4): p. 9.
66. Brdicka, R. and J. Dvorak, *Zaklady fysikalni chemie*. 1977, Praha: Academia.
67. Ditchburn, R.W., *Light*. The student's physics. 1963, London: Blacke & son limited. 833.
68. Eckertova, L., *Metody analyzy povrchu : Elektronova mikroskopie a difrakce*. 1996, Praha: Academia.
69. Singh, J., *Optical Properties of Condensed Matter and Applications*. 2006: John Wiley and Sons. 448.
70. Leitner, J. and P. Vonka, *Termodynamika materialu*. 1992, Praha: Vysoka skola chemicko-technologicka,. 346.
71. Dakhel, A.A., *Thermal annealing effect on the structure, bandgap, and optical constants of Er-Mn oxide thin films.* Vacuum, 2007. **81**(9): p. 1101-1108.
72. Lakowicz, J.R., *Principles of fluorescence spectroscopy*. 2006: Springer.
73. Liu, Y., et al., *Optical Spectroscopy of Eu3+ Doped ZnO Nanocrystals.* Journal of Physical Chemistry C, 2008. **112**(3): p. 686–694.
74. Ikeda, M., et al., *Phase formation and luminescence properties in Eu3+-doped TiO2 nanoparticles prepared by thermal plasma pyrolysis of aqueous solutions* Thin Solid Films, 2008. **516**(19): p. 6640-6644.
75. Boyer, D., G. Bertrand-Chadeyron, and R. Mahiou, *Structural and optical characterizations of YAG:Eu3+ elaborated by the sol–gel process.* Optical Materials, 2004. **26**(2): p. 101-105.
76. Ozawa, T., *A new method of analyzing thermogravimetric data.* Bulletin of the Chemical Society of Japan, 1965. **38**(11): p. 1881-1886.
77. Llopiz, J., et al., *Generalization of the kissinger equation for several kinetic-models.* Thermochimica Acta, 1995. **256**(2): p. 205-211.
78. Augis, J.A. and J.E. Bennett, *Calculation of avrami parameters for heterogeneous solid-state reactions using a modification of kissinger method.* Journal of Thermal Analysis, 1978. **13**(2): p. 283-292.
79. Malek, J. and T. Mitsuhashi, *Testing method for the Johnson-Mehl-Avrami equation in kinetic analysis of crystallization processes.* Journal of the American Ceramic Society, 2000. **83**(8): p. 2103-2105.
80. Langford, J.I. and A.J.C. Wilson, *Scherrer after 60 years - survey and some new results in determination of crystallite size.* Journal of Applied Crystallography, 1978. **11**(APR): p. 102-113.

81. Azzam, R.M.A. and N.M. Bashara, *Ellipsometry and polarized light*. 1977, Amsterdam: North-Holland publishing company.
82. Sysala, O., I. Kasik, and I. Spejtkova, *Preparation of preforms and optical fibers containing aluminum by the solution-doping method.* Ceramics-Silikaty, 1991. **35**(4): p. 363-367.
83. Ningthoujam, R.S., et al., *Photoluminescence studies on Eu doped TiO(2) nanoparticles.* Journal of Alloys and Compounds, 2009. **486**(1-2): p. 864-870.
84. Tokumoto, M.S., et al., *Preparation of ZnO Nanoparticles: Structural Study of the Molecular Precursor.* Journal of Sol-Gel Science and Technology, 2003. **26**(1-3): p. 547-551.
85. Chai, Y.L., et al., *The effects of heat-treatment on the structure evolution and crystallinity of ZnTiO3 nano-crystals prepared by Pechini process.* Materials Research Bulletin, 2008. **43**(5): p. 1066-1073.
86. Ishioka, T., et al., *Vibrational spectra and structures of zinc carboxylates II. Anhydrous zinc acetate and zinc stearate.* Spectrochimica Acta Part A-Molecular and Biomolecular Spectroscopy, 1998. **54**(12): p. 1811-1818.
87. Perrin, F.X., V. Nguyen, and J.L. Vernet, *FT-IR spectroscopy of acid-modified titanium alkoxides: Investigations on the nature of carboxylate coordination and degree of complexation.* Journal of Sol-Gel Science and Technology, 2003. **28**(2): p. 205-215.
88. Preudhom.J and P. Tarte, *Infrared studies of spinels .2. experimental bases for solving assignment problem.* Spectrochimica Acta Part A-Molecular Spectroscopy, 1971. **27**(6): p. 845-851.
89. Preudhom.J and P. Tarte, *Infrared studies of spinels .1. critical discussion of actual interpretations.* Spectrochimica Acta Part A-Molecular Spectroscopy, 1971. **27**(7): p. 961-968.
90. Piotrowski, T. and S. Sikorski, *Photovoltaic effects in an inhomogeneous semiconductor with position-dependent temperature.* Semiconductor Science and Technology, 2001. **16**(9): p. 750-758.
91. Tompkins, H.G., *The initial-stages of the oxidation of titanium nitride.* Journal of Applied Physics, 1992. **71**(2): p. 980-983.
92. Lee, J. and C.W. Choi, *Sol-Gel derived epitaxial MgTiO3 thin films.* Japanese Journal of Applied Physics Part 1-Regular Papers Short Notes & Review Papers, 1999. **38**(6A): p. 3651-3654.
93. Bachir, S., et al., *Photoluminescence of polycrystalline zinc oxide co-activated with trivalent rare earth ions and lithium. Insertion of rare-earth ions into zinc oxide.* Journal of Luminescence, 1997. **75**(1): p. 35-49.
94. Krylova, G., et al., *Natural superhydrophilicity and photocatalytic properties of sol-gel derived ZnTiO(3)-ilmenite/r-TiO(2) films.* Physical Chemistry Chemical Physics, 2010. **12**(45): p. 15101-15110.
95. Shih, C.F., et al., *Low-temperature sintered Zn2TiO4:TiO2 with near-zero temperature coefficient of resonant frequency at microwave frequency.* Journal of Alloys and Compounds, 2009. **485**(1-2): p. 408-412.
96. NIST. *NIST Standard Reference Database Number 69*. National Institute of Standards and Technology]. Available from: http://webbook.nist.gov/chemistry/.